MULTISCALE METHODS FOR TRANSPORT PHENOMENA

BY

RAVI BHADAURIA

DISSERTATION

Submitted in partial fulfillment of the requirements
for the degree of Doctor of Philosophy in Mechanical Engineering
with a concentration in Computation Science & Engineering
in the Graduate College of the
University of Illinois at Urbana-Champaign, 2017

Urbana, Illinois

Doctoral Committee:

Professor Narayana R. Aluru, Chair and Director of Research
Professor Kenneth S. Schweizer
Professor Surya P. Vanka
Assistant Professor Diwakar Shukla

Abstract

In this thesis, we discuss the development of high fidelity multiscale methods to understand fluid flow past solid interfaces. Because of the dominant surface effects at the nanoscale, the classical field based continuum models break down. Particle-based methods offer accurate insights into the flow physics but are computationally expensive. Also, the ratio of pertinent to total information (particle trajectories) from these simulations is minimal. This research entails bridging these two descriptions of the flow physics at different scales to a unified, field-based quasi-continuum framework that can provide atomic level accuracy with continuum level efficiency. First, we discuss the construction of the transport model where fluid density and transport parameters such as viscosity are assumed to be varying across the confinement. These are, in turn, incorporated using Empirical Quasicontinuum Theory (EQT) and Local Average Density Model (LADM). We elucidate the failure of the "no-slip" boundary condition at the nanoscale and its estimation using the collective diffusion coefficient from Equilibrium Molecular Dynamics (EMD) calculations. Further, we reinterpret the slip phenomenon originating from liquid-solid interfacial friction. In this context, we discuss the Generalized Langevin Equation (GLE) based single particle dynamical framework that is consistent with the EMD simulations. Our adsorption based understanding of the flow physics elucidated that the slip length does not change with the slit width. Next, the methodology of multiscale dynamical "coarse-grained" (CG) framework is further refined to incorporate multi-physics to make it viable for a variety of fluid flow situations, such as Poiseuille flow of binary mixtures and nanochannel electroosmosis. The resultant suite of multiscale models significantly reduced the computational burden from tens of thousands of hours to seconds, without trading off the accuracy of the conventional transport parameters. Finally, we demonstrate the failure of local constitutive laws in fluids when strain-rate changes appreciably compared to the fluid molecular diameter, under extreme confinement. Here, a genuinely non-local constitutive relationship between the stress and strain-rate is more appropriate, and the viscosity is interpreted as a non-local kernel instead of a material property defined pointwise. The results indicate that a non-local model performs appreciably well in capturing the strain-rate sign reversals observed from Non-Equilibrium Molecular Dynamics calculations.

To the memory of my grandmother.

Acknowledgments

I would like to thank Prof. Aluru for his countless hours of encouragement, guidance, dedication, and support during this work. Thanks to my doctoral committee members, Prof. Schweizer, Prof. Vanka, and Prof. Shukla for helpful discussions. Many thanks to National Science Foundation and Air Force Office of Scientific Research for their continued financial support during my doctoral research. I would also like to acknowledge parallel computing resources provided by the Campus Cluster and Blue Waters at the University of Illinois, and National Center for Supercomputing Applications. I am immensely thankful to all my group members for helpful discussions. In particular, I would like to mention Sikandar Mashayak, Tarun Sanghi, Kumar Kunal, Aravind Alwan, and Subhadeep De. I also acknowledge the scholars in nanofluidics community, whose literary work has helped to shape my philosophy towards this research area.

I am thankful to my friends for their time, and keeping me cheerful and motivated during my stay at Urbana-Champaign. A special thank you to Souvik Roy, Amit Desai, Sikandar Mashayak, Siddhartha Verma, Tarun Sanghi, Mohammad Heiranian, and Matthew Sylvain for the same.

I would like to thank my uncle and aunt for making me feel at home away from home. Finally, I am deeply indebted and grateful to my wife, Koyal, and my parents for their unflinching support, sacrifice, and patience.

Table of Contents

List of Tables

List of Figures

Chapter 1

Introduction

1.1 Motivation

Understanding the behavior of fluids with different reagents, chemicals, and surfaces is imperative due to its role in biological and industrial processes. With the growing impetus of nanotechnology research, physics of confined fluid has generated tremendous curiosity, ranging from studying water flow in naturally occurring transmembrane protein channels like aquaporins [159, 8] to artificially manufactured graphene/graphite slits and Carbon Nano Tubes (CNT) [94, 178, 93, 69, 160, 72, 81, 80, 79]. The potential applications include water purification [148, 157, 158, 79], biological flows in membranes [159, 8, 146], energy harvesting [118], and many others. These applications have instigated the need to understand the fundamental mechanism of fluid transport under confinement, both from experimental and theoretical standpoint [20].

The nature of interaction between the surface and the fluid is central to understand the flow physics [108, 31, 37], and it affects the flow in two different ways. First, competing surface and fluid interactions result in structural inhomogeneity of the fluid [137, 141, 142, 100, 98]. This structural inhomogeneity leads to spatially inhomogeneous viscosity [162, 163, 166, 27, 28]. Viscous contribution is dominant for flows in naturally occurring hydrophilic channels such as silicates [23, 52]. Second, the lattice structure and the chemical properties of the surface could result in the motion of the fluid molecules relative to the surface, a phenomenon more commonly known as slip [174, 97, 168, 25]. Several experimental [94, 93, 178, 69] and Molecular Dynamics (MD) [72, 160, 79, 81] studies have reported high enhancement, slip dominant flow in engineered hydrophobic surfaces. Therefore, an accurate account of both of these phenomena is critical for the development of a transport model for confined fluids.

1.2 Particle and hybrid particle-continuum based methods

Molecular dynamics (MD) simulations can provide detailed fundamental insights into the flow physics at the nanoscale. Since the pioneering work of Rahman to study liquid Argon [138], they have evolved tremendously

over the past five decades in terms of their performance, partly due to advances in computing power. In these simulations, fluid (and solids alike) are modeled as discrete particles interacting typically via an accurate albeit approximate pairwise potential field, and their trajectories are evolved using Hamilton's equations of motion. The interparticle potentials are representative of different interaction mechanisms such as Born repulsion, van der Waals dispersion, electrostatics, bonds etc. Combined with appropriate spatial and temporal sampling techniques, MD can be used to study fluid structure, dynamics, and transport. Despite its rigor and accuracy, usage of MD as a predictive tool for transport phenomena is comparatively limited due to high computational requirements (massive parallelization), resulting from high degrees of freedom (number of particles) in the system. In addition, the requirement of small time steps for integrating the equations of motion due to stiff potentials restricts one to probe hydrodynamic time scales in a reasonable computational time.

The limitations of MD in probing hydrodynamic time scales can be alleviated to some extent by using softer interparticle interactions and performing a so-called "coarse-grained" dynamical simulations such as Dissipative Particle Dynamics (DPD), first proposed by Hoogerbrugge and Koelman [70]. It is an approach similar to MD regarding preserving Galilean, translational, and rotational invariance, and is widely used to perform simulations of fluid and complex systems at the mesoscale, when hydrodynamics and thermal fluctuations play a role, along with retaining the discrete nature of the interacting particles. Despite its advantages, DPD has few drawbacks. First, the softening of the pairwise interaction potential term by a linear function in typical DPD simulation leads to an unphysical equation of state [59] for liquids. Furthermore, softening of the pairwise force also leads to faster dynamics, and the challenge is to address this deficiency by introducing artificial friction between the particles using a pairwise dissipative and random forces that obey the fluctuation-dissipation relationship.

Since molecular nature manifests predominantly at the liquid-solid interface, hybrid MD-continuum methods can also be utilized in context to study fluid flow problems [112, 61]. In these methods, MD is used to simulate the interfacial phenomenon, while the continuum based modeling approach is undertaken at the bulk-like region. The consistency of mass and momentum exchange between the two domains is maintained by introducing a buffer region, typically of the order of one molecular diameter. The attractiveness of these methods is lost due to the added complexity by adding constraints and convergence issues.

Due to the limitations mentioned above of particle-based and particle-continuum hybrid methods, there is an imperative need to address them from a continuum standpoint. Continuum field-based methods with strong foundations from atomistic or mesoscopic dynamics offer significant advantages over MD. It provides the user flexibility over the spatial resolutions, which can significantly reduce the degrees of freedom. Also,

a plethora of numerical methods (finite element, finite difference, spectral methods, etc.) can be leveraged to provide numerical solutions. For this exercise, the classical continuum-based models should be revised by embedding the microscopic physics in two ways. First, by introducing the liquid structure by incorporating particle spatial correlations such as radial distribution function, and dynamical time correlations information to ensure that the interparticle friction manifesting in the form of transport coefficients such as viscosity, diffusion, and liquid-solid interfacial friction are accurate.

1.3 Review of Transport Models

1.3.1 Constitutive relationships and viscosity models

The formulation of accurate constitutive laws governing the relationship between the stress and strain-rate is quite involved and active area of research. The earliest and simplest framework of intermolecular collision mediated momentum exchange was provided by Chapman and Cowling [39]. It relies on the Chapman-Enskog solution to the Boltzmann equation, that can describe the kinetic theory of gases in bulk. Although the kinetic theory is extremely useful for computation of transport coefficients such as viscosity, diffusion, and thermal conductivity, its usage is rather limited to monoatomic gases at low density. This is because it neglects the ternary collisions, that become important at high density cases. Also, the calculation of temperature dependent collision integrals becomes difficult for complex molecules. Application of different variants of kinetic theory to compute inhomogeneous transport coefficients has met with limited success [126, 127, 1].

Besides the above outlined attempts based on the kinetic theory to rigorously determine the inhomogeneous transport coefficients, heuristic models such as the Local Average Density Model (LADM) can be utilized for the same purpose [28, 20]. The underlying motivation of formulating LADM originates from early efforts to construct excess free energy functionals for inhomogeneous fluids in classical Density Functional Theory (c-DFT). With a specified equation of state for homogeneous (bulk) fluid, the LADM is used to obtain transport properties corresponding to the local point of interest in the homogeneous fluid. Several models for computing local average density exist in literature, such as generalized van der Waals model, hard-rod model, Tarazona model etc. The LADM has provided reasonably satisfactory estimation of the velocity profiles of confined fluids under shear driven situations [28, 125]. However, the accuracy of LADM is still debated due to the lack of an explicit comparison of the local transport property provided by the LADM with the one directly obtained from the MD simulations.

At molecular length scales, however, the notion of local transport properties may not always be an accurate one. Close examination of the confined fluid flow velocity profiles obtained performing gravity driven

MD simulations have confirmed the nature of non-quadratic velocity profiles near the interface [1, 166, 164]. Furthermore, under certain circumstances, the velocity profile showed local extrema while local shear stress being a non-zero quantity, thereby challenging the validity of pointwise stress and strain-rate relationship. The viscous momentum transfer mechanism, in strictest sense, has to be reinterpreted as non-local mechanism instead of a local one [47]. Further studies in this context were able to characterize the non-local kernel for homogeneous fluids [63]. However, computation of a truly non-local viscous kernel for confined fluid is still an open problem [36].

1.3.2 Interfacial slip models

A general first order slip boundary condition for hydrodynamics prevalent in the literature is given as

$$l_{\mathrm{s}} \frac{\mathrm{d}u_x(z)}{\mathrm{d}z}\bigg|_{z=\delta} = u_{\mathrm{s}}, \tag{1.1}$$

where z is the direction perpendicular to the confining walls, u_x is the velocity field, l_{s} is the slip length, $\mathrm{d}u_x/\mathrm{d}z$ is the strain rate, u_{s} is the slip velocity, which is the velocity of the fluid layer relative to the adjoining wall, and δ is the distance from the surface to the location where the boundary condition is applied, also known as the slip plane. Slip length is defined as the distance from the slip plane where the linearly extrapolated value of the velocity is zero. Navier [107] proposed a similar form of the aforementioned slip boundary condition where the slip length depends upon the interfacial friction coefficient ζ_0 and the fluid viscosity μ_0 as $l_{\mathrm{s}} = A\mu_0/\zeta_0$, where A is the interfacial area. This relationship stems naturally from an interfacial force balance, where the viscous force balances the wall-fluid friction force. Although significant progress has been made to understand the interfacial friction coefficient [64, 30, 121], the common approach is to ignore the inhomogeneity in the density and the viscosity across the confinement. Huge variations in the velocity gradient in the interfacial region can also lead to uncertainties in the computed value of slip length [88], thereby limiting the applicability of Non-Equilibrium Molecular Dynamics (NEMD) as a reliable tool to compute slip length. An exhaustive mention of these issues is given recently by Kannam et al. [90, 82], where significant differences in the reported values of slip length have been highlighted.

Bhatia et al. have performed an array of studies targeting slip in meso and nano scale pores [76, 77, 22, 18]. They have developed an oscillator model for computing transport diffusion under special case of Maxwell's boundary condition, which is exact for low density fluids [76]. Viscous and diffusive components of flow are superimposed over each other to obtain the effective transport flux. This approach, although promising, relies on an approximation of diffuse wall boundary condition with the pore which is not always the correct

representation of the wall. To apply their work to a defect free, rigid surfaces, Smoluchowski correction factor is introduced [4], which is a complicated function of the thermodynamic state of the fluid and wall structure, and till date, only limited studies exist for its calculation [151, 155].

Bocquet and Barrat have presented a statistical mechanical based model using Green-Kubo relations for calculating slip length [30, 9]. This model computes the slip length as a ratio of a phenomenological parameter, friction factor to the shear viscosity. This model can then be used in conjunction with Navier slip boundary condition [31] to obtain the velocity profile. The friction factor is inherently related to the fluctuations of wall-fluid interaction force, which can be computed from EMD simulations. Hydrodynamic location of the wall is also computed using EMD correlations, where the Navier slip condition has been applied. However, their expression for friction factor has been a subject of debate whether it does or does not include fluid-fluid viscous effects as the expression involves cross-correlations between two solvent particles [121].

Hansen et al. [64] have sought to mitigate the aforementioned deficiencies by considering the motion of interfacial region from a collective dynamics point of view. The slip boundary condition in their work is replaced by an integral boundary condition, which represents the average velocity on a slab of finite width, unlike on the liquid-solid interfacial plane. The wall-fluid friction force, therefore, balances the viscous shear forces and the additional body force. The friction coefficient is obtained using time autocorrelation of COM force, and COM force–COM velocity cross-correlations on the slab. Their transport model, however, neglects the density and viscosity variation across the confinement, and therefore results in a channel width dependent slip length, even for planar surfaces.

Recently, Huang and Szlufarska [71] have developed a Green-Kubo like expression to obtain friction coefficient from EMD simulations. They have argued that interfacial friction is not a collective quantity, but a single-particle one. The resulting expression for the friction coefficient does not involve cross-particle time correlations. The total wall-fluid friction experienced by the fluid is assumed additive from the contributions of all the interfacial particles. This hypothesis can, in principle, allow one to use single particle dynamical framework to evolve the trajectory of a representative interfacial particle that is consistent with the EMD simulations, and indeed we have leveraged this point of view to explore dynamical coarse-grained methods like GLE to compute interfacial friction.

1.4 Thesis layout

The remainder of the thesis is organized as follows. In Chapter 2, we describe the construction of a multiscale, quasi-continuum framework to predict the velocity profile of a fully developed, confined fluid, driven by a constant gravity (or acceleration) field in the streamwise direction under isothermal conditions. Unlike the classical approach (Stokes equation) where the material properties are assumed to remain constant, we allow for a continuous variation of density and viscosity fields. In this context, we briefly discuss the EQT framework to accurately predict density profile of a confined fluid by simulating Lennard-Jones (LJ) fluids confined inside slit-like channels. The viscosity variations are incorporated using the LADM approach that takes density variation as an input. The interfacial slip is modeled using the time autocorrelation of the collective wall-fluid force acting on the center of mass of the fluid, that is calculated using EMD simulations. We demonstrate the applicability of the transport model to predict the velocity profile of LJ fluids confined in low and high interfacial friction conditions. In Chapter 3, we further improve the computational efficiency of the transport model by discussing a stochastic, non-Markovian, GLE based framework to compute interfacial friction. We demonstrate the accuracy of this approach by predicting the velocity profiles of gravity-driven flow of confined water. In Chapter 4, we extend our multiscale framework to study the gravity-driven flow of binary mixtures, where species-specific momentum equations account for the interspecies diffusive momentum transfer. In Chapter 5, we use the transport model to investigate EOF, which incorporates the solvent polarization, the reduction in interfacial mobility of ions to model the viscosity enhancement near the interface. In Chapter 6, we reinterpret the viscous momentum transfer mechanism by including non-local effects in the constitutive relationship between the stress and the strain-rate. Finally, concluding remarks of this thesis are drawn in Chapter 7.

Chapter 2

A Quasi-Continuum Hydrodynamic Model for Slit shaped Nanochannel Flow

In this chapter, we present a hydrodynamic model which includes both the lateral and longitudinal surface effects. Spatially varying shear viscosity in the confining direction is determined using the existing correlations for viscosity. Slip effects are modeled using a static Langevin equation describing the center of mass (COM) motion of fluid particles [152, 153], with its stochastic force being the total wall-fluid interaction force in the streamwise direction computed from an EMD simulation. We observe that, under the same thermodynamic state, only one EMD simulation is required to obtain parameters of Langevin model for different channel widths. The model is used to study hydrodynamics for three systems, with differing surface-fluid friction due to relative motion between surface and fluid for slit shaped nanochannels.

The rest of the chapter is organized as follows: in Sec. 2.1 we present the hydrodynamic transport model. We briefly discuss the EQT method used to calculate density profiles of fluid under confinement in slit channels. Local average density method (LADM) proposed by Bitsanis *et al.* [27, 28] is used with viscosity correlations presented by Woodcock [170] to obtain spatial variations of fluid viscosity as a functional of density. We also present the development of a generic boundary condition using Langevin type model. In Sec. 2.2, necessary details of MD simulations are provided. In Sec. 2.3 results obtained from the hydrodynamic model are discussed and compared with NEMD simulations.

2.1 Transport model

The starting point of the transport model is the Cauchy momentum equation, which relates inertial flux to the diffusive flux and is given by

$$\frac{\mathrm{D}\rho_m \mathbf{u}}{\mathrm{D}t} = -\nabla P + \nabla \cdot \boldsymbol{\tau} + \mathbf{f} \tag{2.1}$$

where $\mathrm{D}/\mathrm{D}t = \partial/\partial t + \mathbf{u} \cdot \nabla$ is the material derivative, $\mathbf{u}$ is the velocity field, ρ_m is the mass density of the fluid, P is the hydrostatic pressure, $\mathbf{f}$ is the body force per unit volume. $\boldsymbol{\tau}$ is the deviatoric stress tensor, which relates to strain rate constitutive relation to obtain the Navier–Stokes equation for incompressible

fluids

$$\frac{\mathrm{D}\rho_m \mathbf{u}}{\mathrm{D}t} = -\nabla P + \nabla \cdot (\mu \nabla \mathbf{u}) + \mathbf{f} \tag{2.2}$$

where μ is the dynamic viscosity. This can be further approximated for one-dimensional gravity driven low Reynolds number flow (see Fig. 2.1) as

$$\frac{\mathrm{d}}{\mathrm{d}z}\left[\mu(z)\frac{\mathrm{d}u_x(z)}{\mathrm{d}z}\right] + m\rho(z)g_x = 0 \tag{2.3}$$

with boundary conditions

$$u_x\left(-\frac{L}{2}+\delta\right) = u_x\left(+\frac{L}{2}-\delta\right) = u_\mathrm{s} \tag{2.4}$$

where $u_x(z)$ is the unknown streaming direction velocity, z is the direction of confinement, x is the streaming direction, m is the molecular mass of the fluid, $\rho(z)$ is the number density (which relates to mass density $\rho_m(z) = m\rho(z)$, and is referred as density from now on), L is the channel width and g_x is the gravity field applied in the streaming direction. Continuity equation is already satisfied under the assumption that u_z is identically zero. Closure to the governing equations is provided by Dirichlet boundary condition at a fixed distance δ from the surface. Inputs required for this framework are density, viscosity, magnitude of slip velocity u_s and the distance δ from the actual position of the wall, where slip condition is applied. The methods to obtain these inputs are discussed below.

2.1.1 Density profiles

We first calculate density variations along the confinement to facilitate computation of viscosity profile in the slit. Here, we use Empirical-potential based Quasicontinuum Theory (EQT) to compute the density profiles [137, 141, 142, 100, 99]. EQT is a multiscale framework for fast and accurate prediction of density profile of confined fluid. It uses a continuum formulation to model the wall-fluid and fluid-fluid interaction between the atoms, and solves for the density and total potential of mean force (PMF) inside a channel in a self-consistent manner. The inputs to the EQT framework are wall-fluid, and fluid-fluid interaction parameters, average density of fluid in the slit, and channel wall density. In EQT, for a slit like channel, as shown in Fig. 2.1, density variation in the channel is modeled as a one-dimensional continuum variable expressed by 1D steady-state Nernst–Planck equation,

$$\frac{\mathrm{d}}{\mathrm{d}z}\left(\frac{\mathrm{d}\rho(z)}{\mathrm{d}z} + \frac{\rho(z)}{k_\mathrm{B}T}\frac{\mathrm{d}U(z)}{\mathrm{d}z}\right) = 0, \tag{2.5}$$

with boundary conditions and integral constraint on average channel density as

$$\rho\left(-\frac{L}{2}\right) = \rho\left(+\frac{L}{2}\right) = 0, \tag{2.6a}$$

$$\frac{1}{L}\int_{-L/2}^{+L/2} \rho(z)\mathrm{d}z = \rho_{\mathrm{avg}}, \tag{2.6b}$$

where $U(z)$ is the total PMF, T is the fluid temperature, k_{B} is the Boltzmann constant, and ρ_{avg} is the average number density of the fluid in the slit, which depends upon the thermodynamic state of the fluid, i.e., operating temperature and pressure.

The total PMF has two components, namely wall-fluid (U^{wf}) and fluid-fluid (U^{ff}) PMF, resulting from interactions of wall-fluid and fluid-fluid particles, respectively, and is given by $U = U^{\mathrm{wf}} + U^{\mathrm{ff}}$. Wall-fluid PMF is computed from the continuum approximation of the wall, obtained by suitable integration taking into account the wall structure and density (ρ_{wall}), and wall-fluid interaction parameters [156], as shown in Eq. (2.7a). Similarly, fluid-fluid PMF in EQT can be computed by integrating the potential between the fluid particles, weighted by the fluid density, as in Eq. (2.7b),

$$U^{\mathrm{wf}}(z) = \int_V u^{\mathrm{wf}}(|z-r|)\rho_{\mathrm{wall}}(r)\mathrm{d}V, \tag{2.7a}$$

$$U^{\mathrm{ff}}(z) = \int_V u^{\mathrm{ff}}(|z-r|)\rho(r)\mathrm{d}V, \tag{2.7b}$$

where u^{wf} and u^{ff} are wall-fluid and fluid-fluid pair potentials, $\mathrm{d}V$ is the infinitesimal volume element centered at r, and $\rho(r)$ is the fluid number density in the volume V, outside of which, interactions between particles is neglected. A Lennard–Jones (LJ) pair potential that describes interaction between two particles, i and j of same or different species (wall and fluid), separated at distance r is written as

$$u_{\mathrm{LJ}}^{ij}(r) = \frac{C_{12}^{ij}}{r^{12}} - \frac{C_6^{ij}}{r^6}, \tag{2.8}$$

where $C_{12} = 4\epsilon_{ij}\sigma_{ij}^{12}$ and $C_6 = 4\epsilon_{ij}\sigma_{ij}^{6}$ are LJ potential parameters. Since LJ potential is highly repulsive at small distances, computation of fluid–fluid potential may suffer from numerical singularities, leading to spurious results, or may be rendering a very stiff, and in many cases unsolvable system of equations. To avoid this, the repulsive core is "softened" by the introduction of structurally consistent smooth potential functions and bridging them with the usual 12–6 form of the LJ potential. The fluid–fluid interactions used

in this work can be summarized as [141]

$$u^{\mathrm{ff}}(r) = \begin{cases} 0 & r < R_{\mathrm{crit}} \\ \sum_{n=0}^{2} a_n r^n & R_{\mathrm{crit}} \leq r < R_{\mathrm{min}} \\ u_{\mathrm{LJ}}^{\mathrm{ff}}(r) & R_{\mathrm{min}} \leq r < R_{cut} \\ 0 & r \geq R_{cut} \end{cases} \tag{2.9}$$

R_{crit} and R_{min} are parameters that define the softer repulsion and truncated core and can be obtained using an optimization algorithm. C^2 type continuity, which implies the two bridge potentials, and their first and second derivatives have the same value at R_{min} is ensured to uniquely identify the parameters a_n, as discussed in Ref. [141]. Further discussion on these parameters and their values are provided in the results section.

2.1.2 Viscosity profiles

In this section, we discuss the incorporation of viscosity variation into the hydrodynamic model. Since density in the slit channel varies with position, we capture the viscosity as a density dependent property. Density variations are used to estimate the local thermodynamic state of the fluid in confinement, and correlations for shear viscosity for bulk fluid are mapped to obtain the local viscosity. Bitsanis *et al.* were among the first to investigate from MD simulations the effect of density variation in velocity profiles obtained from Couette flow [27]. Few salient features of their work are

1. Viscosity must be a local function of position in the confining direction to account for the observed non-linearity in velocity profiles.
2. Density variation along the confining direction is correlated to the observed velocity profile.
3. Density profiles do not change significantly for a transport (NEMD) simulation as compared to an equilibrium (EMD) simulation for the amount of shear rates of practical interest.

Based on the above observations, the authors proposed LADM which states that the local shear viscosity, instead of being a direct function of density $\rho(z)$, is a function of the local average number density $\bar{\rho}(z)$, which is defined as

$$\bar{\rho}(\mathbf{r}) = \frac{6}{\pi \sigma_{\mathrm{ff}}^3} \int\limits_{|\mathbf{r}-\mathbf{r}'|<\sigma_{\mathrm{ff}}/2} \rho(\mathbf{r}') \mathrm{d}^3\mathbf{r}'. \tag{2.10}$$

This "coarse-grained" local average density identifies a unique homogeneous (bulk) state of confined inhomogeneous fluid at a particular location in the confinement. Further accurate modeling for local average

density involves averaging density profile at each point with appropriate weight functions [68], where the definition of local average density becomes

$$\bar{\rho}(\mathbf{r}) = \int\limits_{|\mathbf{r}-\mathbf{r}'|<\sigma_{\mathrm{ff}}/2} \omega(|\mathbf{r}-\mathbf{r}'|)\rho(\mathbf{r}')\mathrm{d}^3\mathbf{r}', \tag{2.11}$$

where the weight function ω can take various forms to deal with different thermodynamic properties of interest [44, 62], and satisfies the normalization condition

$$\int\limits_{|\mathbf{r}-\mathbf{r}'|<\sigma_{\mathrm{ff}}/2} \omega(|\mathbf{r}-\mathbf{r}'|)\mathrm{d}^3\mathbf{r}' = 1. \tag{2.12}$$

In this work, we choose hard-rod model using which the local average density equation is written in one dimensional form as [167]

$$\bar{\rho}(z) = \frac{6}{\sigma_{\mathrm{ff}}^3} \int\limits_{|z-z'|<\sigma_{\mathrm{ff}}/2} \left[\left(\frac{\sigma_{\mathrm{ff}}}{2}\right)^2 - (z-z')^2\right] \rho(z')\mathrm{d}z', \tag{2.13}$$

which can then be used to obtain viscosity using suitable models for equation of state of shear viscosity. Enskog has provided a closed form expression for viscosity of fluids interacting with a hard sphere potential.[39] Similarly for LJ fluids, once an effective hard sphere diameter is calculated [60], Enskog theory can be used to predict shear viscosity. While suitable correlations such as those given in Ref. [41] exist, there are limitations on their applicability to different thermodynamic states. Corrections based on an accurate equation of state for LJ fluid have been proposed in Ref. [103], but they require empirical constants, which are different for different fluids [75].

In this work, we adopt the method proposed by Woodcock to calculate viscosity from local average density [170]. A one parameter model which is valid for nearly all equilibrium states of liquid and gaseous phase for LJ fluid is used. The correlation calculates viscosity as

$$\mu(\bar{\rho}^*, T^*) = \mu_0(T)\left[1 + B_\mu^*\bar{\rho}^* + C_{\mathrm{AH}}(1/T^*)^{1/3}(\bar{\rho}^*)^4\right], \tag{2.14}$$

where $\bar{\rho}^* = \bar{\rho}\sigma_{\mathrm{ff}}^3$ and $T^* = k_{\mathrm{B}}T/\epsilon_{\mathrm{ff}}$ are reduced local average density and temperature respectively, and k_{B} is the Boltzmann constant. μ_0 is the zero density limit viscosity and is computed as

$$\mu_0 = \frac{5}{16\sigma_{\mathrm{ff}}^2}\sqrt{\frac{mk_{\mathrm{B}}T}{\pi}}\frac{f_\mu}{\Omega^{*(2,2)}}, \tag{2.15}$$

where $\Omega^{*(2,2)}$ is collision integral, and f_μ is dependent upon collision integrals, which follow recursion relation as discussed in Ref. [117]. For finite densities, additional corrections for first order dependence of viscosity on density over μ_0 is done through the addition of Rainwater-Friend coefficient [50] (B^*_μ) as

$$B^*_\mu = \sqrt{2}(1 - (T^*)^{-4} - T^*/8). \tag{2.16}$$

C_{AH} is the Ashurst-Hoover coefficient [6] and its value is taken as 3.025. For further details on the correlation, readers are referred to the original text in Refs. [170, 117].

2.1.3 Boundary condition: Langevin model

To close the model, boundary conditions are needed. In macro-scale hydrodynamics, the use of "no-slip" condition is widely accepted, in which the relative motion between the surface and the fluid is not assumed. But at smaller scales, this phenomenological relation fails to hold. Fluid flow past a surface can exhibit relative motion between the surface and the fluid, a phenomenon known as slip [179, 161]. The degree of slippage depends on the nature of physical interaction between the surface and the fluid molecules. When fluid particles try to move past a surface, a friction force tries to retard their relative motion due to the trapping and hopping mechanism in surface-fluid potential energy map [174, 97, 168], such that the shear stress in the fluid is balanced at the interface. Topology of the surface and strength of the surface-fluid interaction relative to the applied shear gradient (Couette flow) or driving force (Poiseuille flow) dictates the slip velocity [5, 31, 130, 109, 131]. We propose a model for computation of slip velocity for isothermal gravity driven flow using Langevin dynamics [180, 152, 153], which incorporates these effects into a time autocorrelation function of surface-fluid force in the streaming direction. We assume that the fluid slip is a collective motion of particles, which can be modeled as a lumped Brownian particle in the dissipative force field of the surface. This can be written in the form of Langevin equation [152, 153] as

$$M\frac{\mathrm{d}u_{\mathrm{c}}}{\mathrm{d}t} = -\eta u + F(t), \tag{2.17}$$

where $M = Nm$ is the mass of the lumped Brownian particle, N is the number of particles in the simulation box, u_{c} is the collective velocity and $F(t)$ is the random force acting on the particle due to the surface in the absence of any non-equilibrium force and relates to the dissipative coefficient η from the fluctuation-dissipation theorem as

$$\eta = \frac{1}{k_{\mathrm{B}}T}\int_0^\infty \langle F(0)F(t)\rangle \mathrm{d}t. \tag{2.18}$$

Using Einstein relation [89], collective diffusion coefficient D_c of the Brownian particle can be written as

$$D_c = \frac{k_B T}{\eta}, \tag{2.19}$$

which can be related to slip velocity, u_s, in NEMD via mobility, μ_{mob} and diffusion relationship

$$\mu_{mob} = \frac{u_s}{M g_x} = \frac{D_c}{k_B T}, \tag{2.20}$$

where g_x is the applied gravity. The final expression for slip velocity can be written as

$$u_s = \frac{D_c M g_x}{k_B T} = k_B T N m g_x \left[\int_0^\infty \langle F(0) F(t) \rangle \mathrm{d}t \right]^{-1}. \tag{2.21}$$

Time autocorrelation of the total surface-fluid interaction force in the streaming direction can be computed using an equilibrium MD simulation, which is computationally less expensive to perform as compared to non-equilibrium MD simulation [30, 9]. Computation of force autocorrelation is independent of width of the nanochannel, provided they are at the same thermodynamic state. This model serves as a fast and accurate tool for calculation of the slip velocity. Slip boundary condition is applied at the location of first density peak, which is the location of PMF minimum [22].

2.2 MD Simulation

We consider three types of systems to represent differing levels of friction between the surface and the fluid. The working fluid in all cases is single site methane, represented as a LJ particle. For the first (low friction) system, methane confined between rigid graphene sheets is considered. For the second system, we consider rigid graphene like structure, with the wall interaction parameter changed to that of methane ($\epsilon_{ww}/k_B = 148.1$ K). This case is similar to the one presented by Sokhan et al. [155], and results in a moderate friction type of a flow situation. For the third system, four layers of a rigid silicon wall oriented in [111] direction as presented in Ref. [132] is considered with $\epsilon_{ww}/k_B = 294.93$ K, and is representative of high friction (no-slip) type boundary. All MD simulations considered here are performed at constant temperature of 300 K with a timestep of 1 fs. Lorentz-Berthelot combination rule is used to calculate the interaction parameters of surface and fluid. The number of particles in a channel is estimated using the linear superposition approximation [150, 43], which provides a simpler way of computing the average density in a nanochannel. Center to center distance between the first layer of wall atoms, closest to the fluid atoms

from top and bottom walls, is defined as the channel width, and this definition is used for computing the average density in the nanochannel. Simulations are performed for channel widths $20\sigma_{\mathrm{ff}}$ to $3\sigma_{\mathrm{ff}}$, for all the systems studied here.

MD simulations are performed with LAMMPS [123], with working fluid as single site methane molecule. Both wall–fluid and fluid–fluid interactions are modeled with 12–6 LJ potential (see Eq. (2.8)), with parameters reported in Table 2.1. For EMD simulations, systems are equilibrated for 5 ns by simulating an NVT ensemble with Nosé–Hoover thermostat [110] with time constant of 0.4 ps. After that, production run for 10 ns is performed, with data collected every 0.02 ps for calculating force autocorrelation. This data is divided into 1000 similar samples of 10 ps each, and the resultant force autocorrelation is averaged by the number of samples.

NEMD simulations are performed with the same force field parameters as for EMD simulations. In addition, a uniform gravity field is applied in the x-direction, with their magnitude 4×10^{-4} nm/ps^2 (for graphene wall), 2×10^{-3} nm/ps^2 (for modified graphene wall), and 2×10^{-3} nm/ps^2 (for silicon wall, except for $3\sigma_{\mathrm{ff}}$ channel in this case, where 5×10^{-3} nm/ps^2 is used for better signal to noise ratio). To control the temperature, we again make use of the NVT ensemble with Nosé–Hoover thermostat, only this time the thermostat is coupled to y and z directions, so that it does not interfere with the flow dynamics. We also checked that the thermostat follows the equipartition theorem, by comparing the thermal kinetic energy (computed using peculiar velocity) per particle in each direction to be equal to $k_{\mathrm{B}}T/2$. This ensures that the thermostat effect is observed in each direction due to inter-particle interactions, despite not explicitly coupling it with x-direction. Simulations are performed for 20 ns, the first 10 ns data is discarded to allow for a fully developed flow profile, and the next 10 ns data is collected at every 0.2 ps. Ten identical simulations are performed with initial velocities of particles drawn from a Maxwell distribution with different seeds, to get an error estimate on the mean velocity profile. Bins of width $0.1\sigma_{\mathrm{ff}}$ are used to compute the density and $0.2\sigma_{\mathrm{ff}}$ are used to sample velocity profiles. For reliable statistics, a minimum of 500 fluid particles were simulated in MD system, with box lengths suitably adjusted to account for the correct average density in the channel.

2.3 Results

To test the proposed hydrodynamic model, we present here the results for three different types of systems with differing surface–fluid interaction and corrugation. We calculate the density profiles from EQT, which are used in calculating viscous component of the flow. Slip component of the flow is incorporated using

Eq. (2.21). For the low friction system (C–CH_4), fluid inside the slit is in equilibrium with a bath of bulk density (ρ_b) 2.138 atoms/nm^3, whereas moderate friction system (C*– CH_4) is in equilibrium with bulk fluid with density $\rho_b = 2.936$ atoms/nm^3. Lastly, the high friction case (Si–CH_4) is at thermodynamic state corresponding to a bulk density $\rho_b = 2.97$ atoms/nm^3. To obtain the values of parameters R_{min} and R_{crit} in Eq. (2.9), we adopt the linear scaling relations proposed in Ref. [141] as a first approximation. These parameters are then fine tuned to obtain the present results. EQT parameters are reported in Table 2.2. Comparison of the density profiles in Fig. 2.2 between EQT and MD shows that there is a very good quantitative match between the two methods.

Variation of the local average density ($\bar{\rho}$) computed from EQT profile using Eq. (2.13) is also plotted in Fig. 2.2. We see that the average density is weighted average form of the density, and hence shows less undulations in its profile. There is not much shift in the peak position between the average density and density peaks because of the nature of the chosen weight function, which provides a higher bias for $|z - z'| \to 0$ as evident from Eq. (2.13). A representative plot of viscosity profile is presented for Si–CH_4 system in Fig. 2.3. It should be noted that viscosity in the limit of zero average density ($\bar{\rho} \to 0$) is $\mu \to \mu_0$, which is the dilute gas viscosity.

The autocorrelation integral $\int_0^\infty \langle F(0)F(t)\rangle dt$ is computed from the autocorrelation data $\langle F(0)F(t)\rangle$ obtained from EMD simulation. We assume that the autocorrelation follows exponential relaxation. A two parameter exponential function is fitted to MD autocorrelation data, and further calculations for computing the integral is done on the fitted function. This process is needed for only one slit, since they are independent of slit size, and the results presented in Fig. 2.4 are for $20\sigma_{ff}$ channel. As evident from the plots, the maximum value of force autocorrelation $\langle F(0)F(0)\rangle$ increases from lowest friction (C–CH_4) case to highest friction case (Si–CH_4), indicating that magnitude of slip velocity should be highest in C–CH_4 system and lowest in Si–CH_4 system, as understood from Eq. (2.21). The parameters for exponential fit are reported in Table 2.3.

2.3.1 Low wall-fluid friction: Methane confined between graphene surfaces

Since the surface energy parameter of graphene is very low ($\epsilon_{ww}/k_B = 28$ K) and it possesses a hexagonal closed pack structure of sp^2 hybridized carbon with bond length of 0.142 nm compared to its diameter of 0.34 nm, its surface landscape is very smooth. Therefore, this weakly corrugated surface results in a high degree of specular reflections of fluid particles after interaction with the wall, leading to a very little resistance to the collective motion of fluid under gravity driven flow. This physics is well captured in the results presented in Fig. 2.5 for various slit sizes, which demonstrate that there is a considerable amount of slip flow, reflected

by the plug-like nature of velocity profiles. It can be deduced that the viscous effects are not so important in this type of low wall-fluid friction systems. However, the contribution of slip flow decreases with increase in the slit size, where the effect of the wall subsides in the region far away from the interface, and the viscous contribution starts to increase. Slip velocity boundary condition is applied at the first peak of the density profile, which is at a distance of 0.3619 nm from the wall.

2.3.2 Moderate wall-fluid friction: Methane confined between modified graphene surfaces

For this system, the LJ potential energy parameter ϵ_{ww} of the wall was set equal to that of the fluid, thereby making the wall–fluid (slip) and fluid–fluid (viscous) effects comparable to each other. The amount of slip observed in response to applied gravity is less than that of graphene-methane system (as applied gravity value for the slip case is about one order of magnitude less than that of the other two cases), but still there is a considerable amount of slip present in the velocity profiles as shown in Fig. 2.6. This can be explained by increased corrugation of the surface potential, responsible for the degree of slippage. Enhanced value of the wall-fluid interaction energy parameter results in more friction and therefore provides more resistance to the moving fluid, as compared to the low friction case. In this case, a prominent parabolic shaped velocities superimposed on a considerable amount of slip flow for larger slit size is observed (see Fig. 2.6(a)). We again observe that the effect of slip contribution increases with decreasing slit size, similar to slip case (see Figs. 2.6(a)-2.6(d)). This is due to the wall effects becoming dominant in the smaller slit size channels, because the confining surfaces are closer. Again, slip velocity boundary condition is applied at the first peak of the density profile, which is at a distance of 0.3619 nm from the wall.

2.3.3 High wall-fluid friction: Methane confined between silicon surfaces

In this case, surface structure (FCC 111, rougher than that of graphene lattice) and wall-fluid interaction energy parameter result in increased corrugation of the potential, which is non-conducive for facilitating slip. A very little amount of slip is observed as shown in Fig. 2.7. This case is representative of the viscous effects dominating over slip. The velocity profiles show a parabolic type nature in larger size slits as shown in Fig. 2.7(a), while a non-parabolic velocity profile in clearly evident in Fig. 2.7(b) for a slit size of $9\sigma_{ff}$, which shows undulations near the interface. Reducing the slit size further to $4\sigma_{ff}$, where no bulk type region is observed in the density profile (see Figs. 2.2(c) and 2.3), shows significant deviation from parabolic profile as seen from Fig. 2.7(c) which one would obtain using a constant density and viscosity. Thus, a spatially varying density and viscosity formulation of hydrodynamic problem is important especially in smaller slit

sizes. Again, the slip velocity boundary condition is applied at 0.3239 nm, which is the first density peak location. It is observed that the match between continuum and MD results is not so good for $3\sigma_{\text{ff}}$ wide channel. This can be attributed to assumption of exponential relaxation for autocorrelation of wall–fluid interaction force (see Fig. 2.4(c)). A better approximation would capture the backscattering effects in the autocorrelation, thereby reducing the value of the integral and enhanced value of slip, which currently lacks in the present approximation.

2.3.4 Mass flow rate

To test the relative contribution of slip and viscous effects in different systems, we calculate the mass flow rate, $\dot{m}$, as

$$\dot{m} = \int_{-L/2+\delta}^{+L/2-\delta} m\rho(z)u_x(z)\mathrm{d}z \tag{2.22}$$

The above equation assumes unit length in y-direction. To compute the slip contribution to the mass flow rate $\dot{m}_s$, the profile $u_x(z)$ is replaced by a constant value of u_s obtained from Eq. (2.21). The ratio $\dot{m}_s/\dot{m}$ is calculated for all systems and it is observed from Fig. 2.8, that the contribution of slip in mass flow rate is highest in narrower slits. Similar trends are also observed by Bhatia *et al.* in Ref. [21], where the effect of contribution of viscous flow decreases in narrower SWNT (10,10) as compared to larger SWNT (60,60). While viscous effects are important in larger slits and slip starts to become a dominant flow mechanism in narrower slits, the contribution of viscous effects still cannot be neglected since they account for about 30 percent of flow rate in high friction system at slit size of $4\sigma_{\text{ff}}$ (see Fig. 2.8(b)). A constant density and viscosity based transport model would result in a very different value of mass flow rate, therefore the importance of density and viscosity variations cannot be overlooked in these cases.

In this chapter, we have developed a quasi-continuum hydrodynamic transport model for gravity driven flow in slit shaped nanopores. We have demonstrated the importance of both viscous and slip components in the velocity profile by considering three different types of systems which elucidate competition between the two phenomenon. Density profiles are used to calculate space dependent viscosity profile, using LADM method. This variation is necessary to capture the non-parabolic nature of velocity profiles as it would have been for constant density and viscosity case. A general boundary condition which takes into account the total wall-fluid interactions modeled into the static Langevin equation describing center of mass motion of fluid inside the slit is used. It is demonstrated that this boundary condition works for a spectrum of wall-fluid interaction type, and its parameters are constant for fluids confined in slit under same thermodynamic state. Furthermore, it is revealed from the velocity profiles that the slip contribution in mass flow rate increases in

all cases when the confining length is decreased, which indicates that wall-fluid effects become more dominant compared to fluid-fluid effects for smaller slit sizes. Overall, the model results in good agreement with the velocity profiles obtained from NEMD simulations, and is valid for reasonable thermodynamic states that are studied in experiments for a variety of wall-surface interactions.

Table 2.1: LJ interaction parameters for surface and fluid atoms. C is carbon atom, C* is carbon atom with methane LJ energy parameter and Si is silicon atom. Fluid is LJ methane denoted by CH_4.

Atoms	σ (nm)	ϵ (kJ/mol)
CH_4–CH_4	0.3810	1.2314
C–C	0.3400	0.2328
C*–C*	0.3400	1.2314
Si–Si	0.3385	2.4522
CH_4–C	0.3605	0.5354
CH_4–C*	0.3605	1.2314
CH_4–Si	0.3597	1.7377

Table 2.2: EQT parameters for computing density profiles.

System	R_{crit} (nm)	R_{min} (nm)	a_0 (kJ/mol)	a_1 (kJ/mol/nm)	a_2 (kJ/mol/nm^2)
C–CH_4	0.24	0.4125	87.1561	-417.4426	492.9563
C*– CH_4	0.19	0.4095	99.1396	-475.7608	563.9083
Si–CH_4	0.19	0.4170	71.4594	-341.7384	401.6761

Table 2.3: Parameters for exponential fit $\langle F(0)F(t)\rangle \approx A\,\exp(-Bt)$.

System	A (kJ/mol/nm)^2	B (1/ps)
C–CH_4	2.256×10^3	15.710
C*– CH_4	1.186×10^4	12.484
Si–CH_4	5.722×10^5	16.350

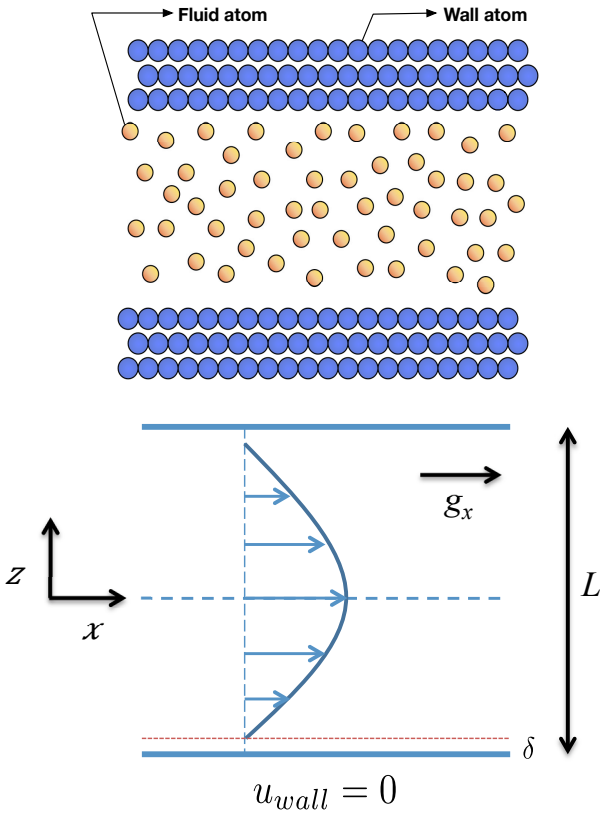

Figure 2.1: Schematic plot of the gravity driven flow considered in present work.

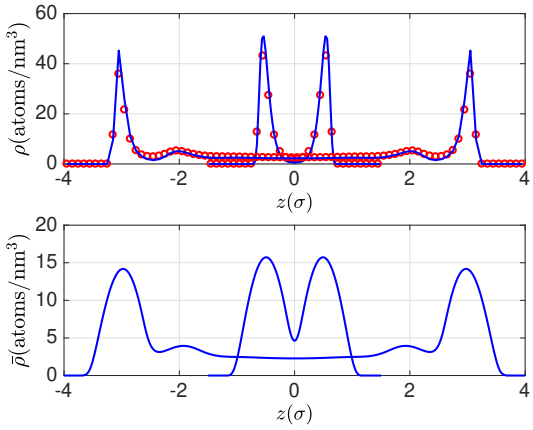

(a) C–CH_4 system

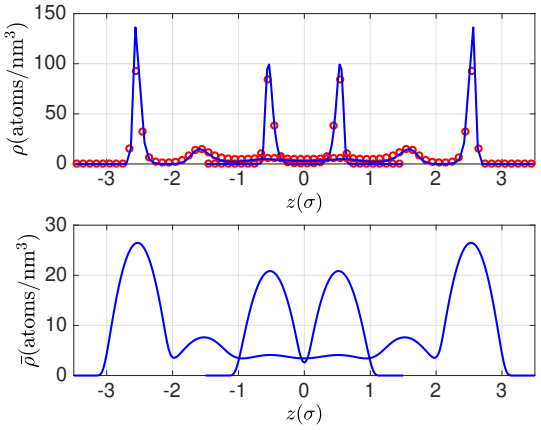

(b) C*–CH_4 system

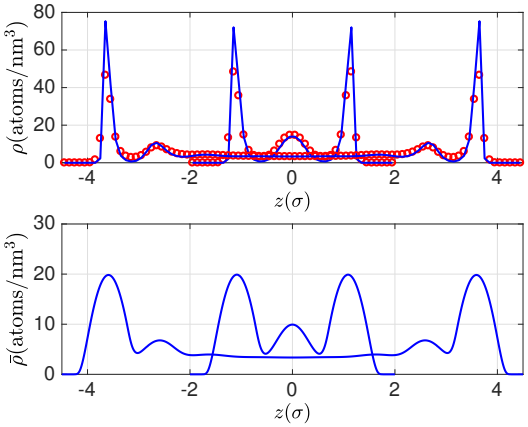

(c) Si–CH_4 system

Figure 2.2: Density ($\rho(z)$, top plot) and average density profiles ($\bar{\rho}(z)$, bottom plot) computed using LADM for select cases of (a) C–CH_4 ($8\sigma_{\text{ff}}$ and $3\sigma_{\text{ff}}$), (b) C*–CH_4 ($7\sigma_{\text{ff}}$ and $3\sigma_{\text{ff}}$), and (c) Si–CH_4 ($9\sigma_{\text{ff}}$ and $4\sigma_{\text{ff}}$) type systems. For density subplot, line (blue) represents EQT results, while circles (red) represent profiles from MD simulation.

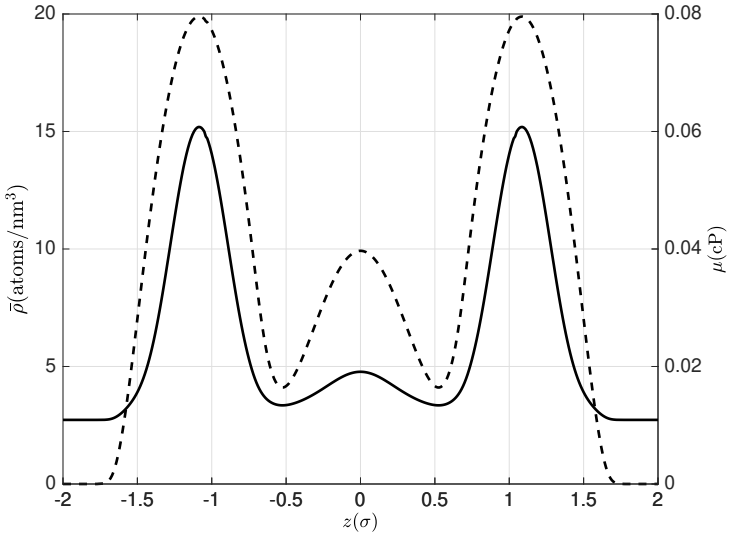

Figure 2.3: Average density (dashed, left-axis) and viscosity (bold, right-axis) for $4\sigma_{\text{ff}}$ wide Si–CH_4 system.

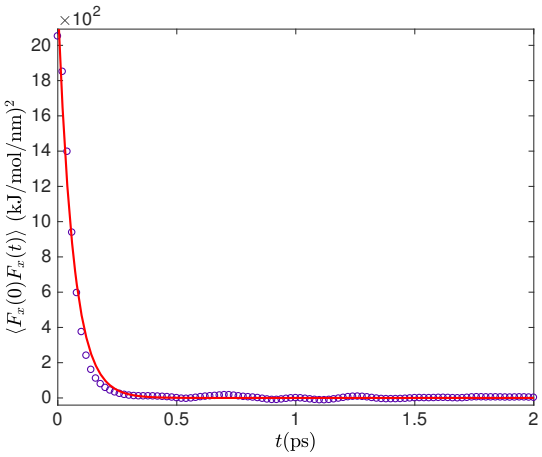

(a) C–CH_4 system

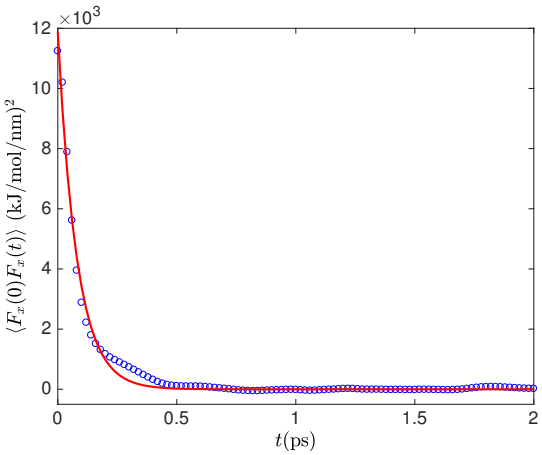

(b) C^*–CH_4 system

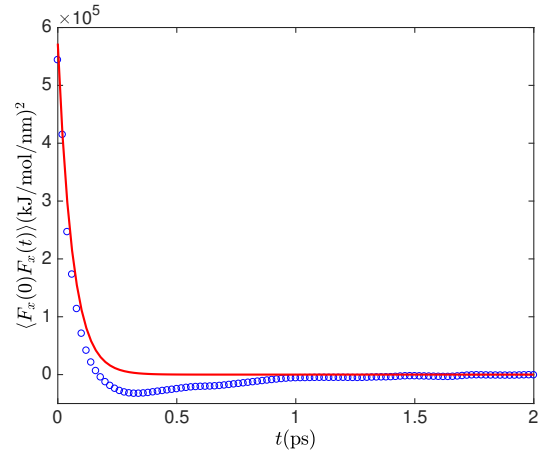

(c) Si–CH_4 system

Figure 2.4: Surface-fluid total force autocorrelation from MD simulation (circles, blue) and exponential fits (bold line, red) for (a) C–CH_4, (b) C^*–CH_4 and (c) Si–CH_4 system.

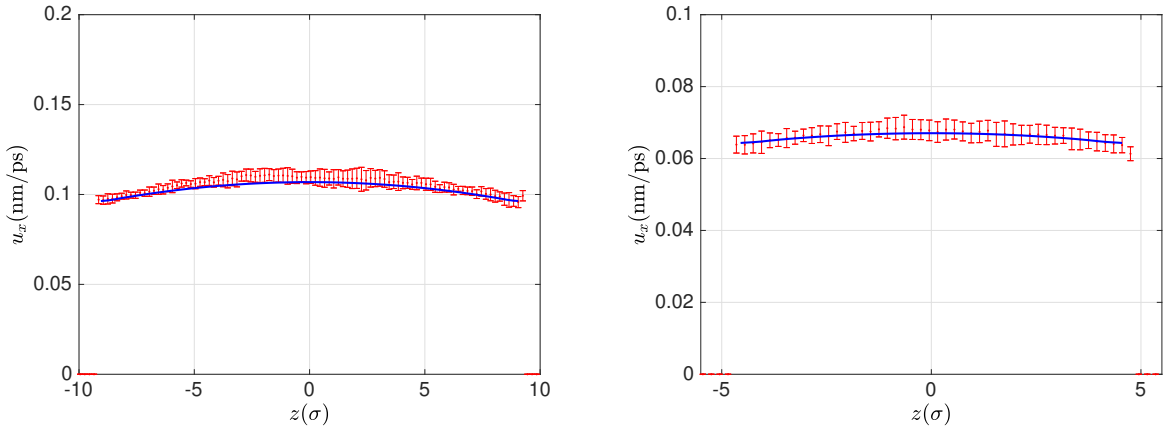

(a) $20\sigma_{\text{ff}}$

(b) $11\sigma_{\text{ff}}$

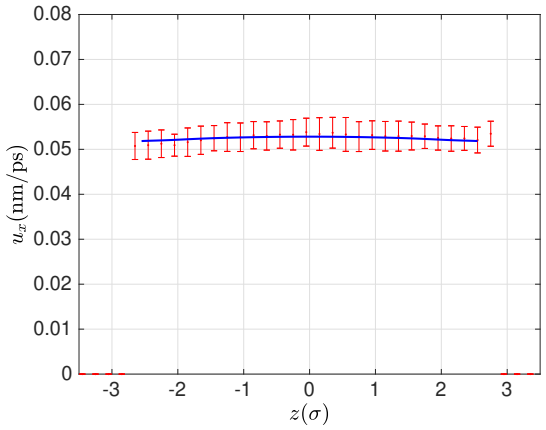

(c) $7\sigma_{\text{ff}}$

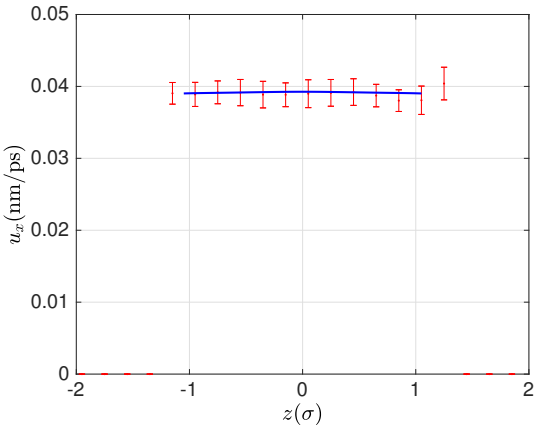

(d) $4\sigma_{\text{ff}}$

Figure 2.5: Velocity profiles for methane confined in graphene slits of size (a) $20\sigma_{\text{ff}}$, (b) $11\sigma_{\text{ff}}$, (c) $7\sigma_{\text{ff}}$ and (d) $4\sigma_{\text{ff}}$. Continuum results are in solid line (blue), while MD results are represented by error bars (red).

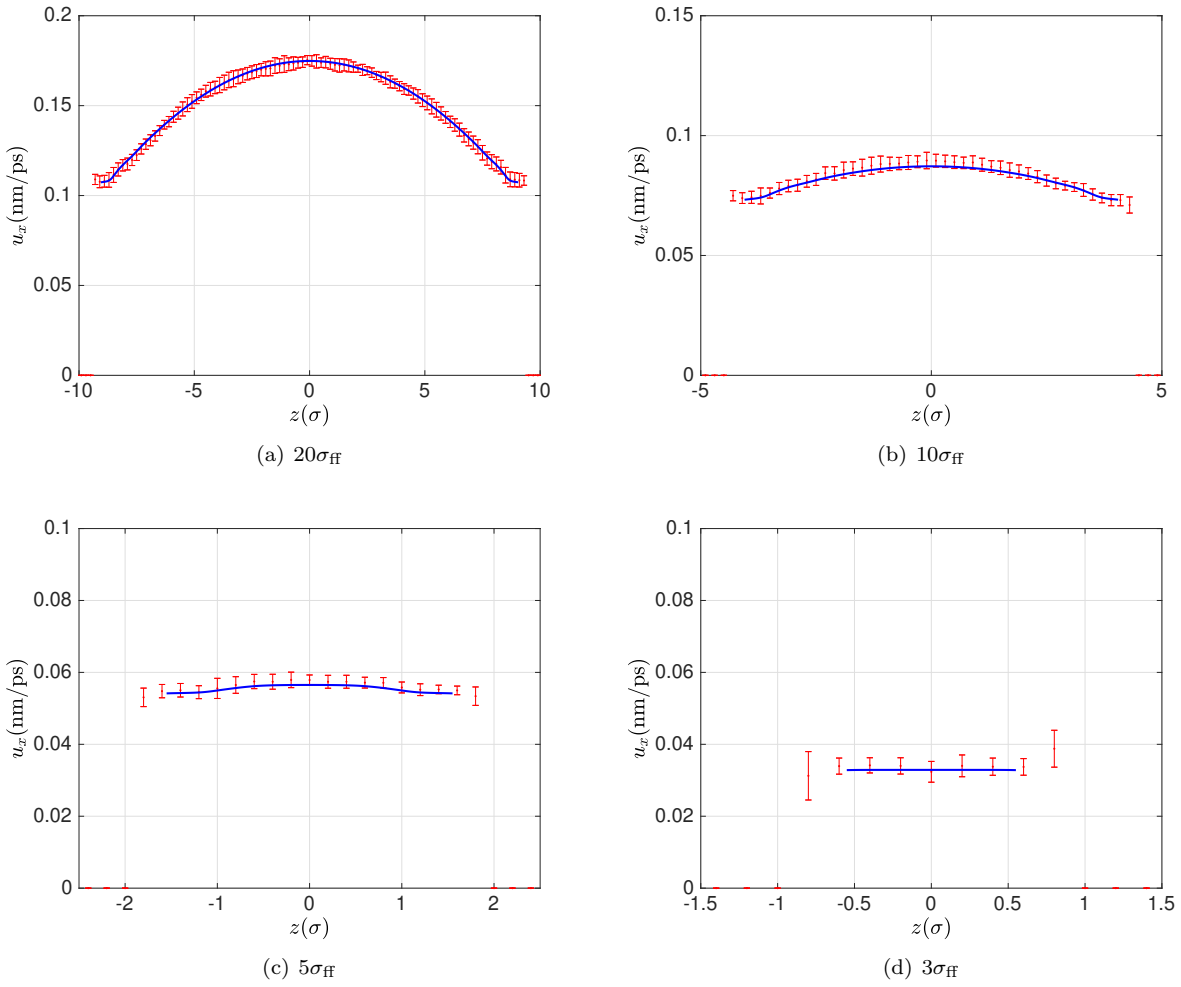

(a) $20\sigma_{\text{ff}}$ (b) $10\sigma_{\text{ff}}$

(c) $5\sigma_{\text{ff}}$ (d) $3\sigma_{\text{ff}}$

Figure 2.6: Velocity profiles for methane confined in modified graphene [C*] slits of size (a) $20\sigma_{\text{ff}}$, (b) $10\sigma_{\text{ff}}$, (c) $5\sigma_{\text{ff}}$ and (d) $3\sigma_{\text{ff}}$. Continuum results are in solid line (blue), while MD results are represented by error bars (red).

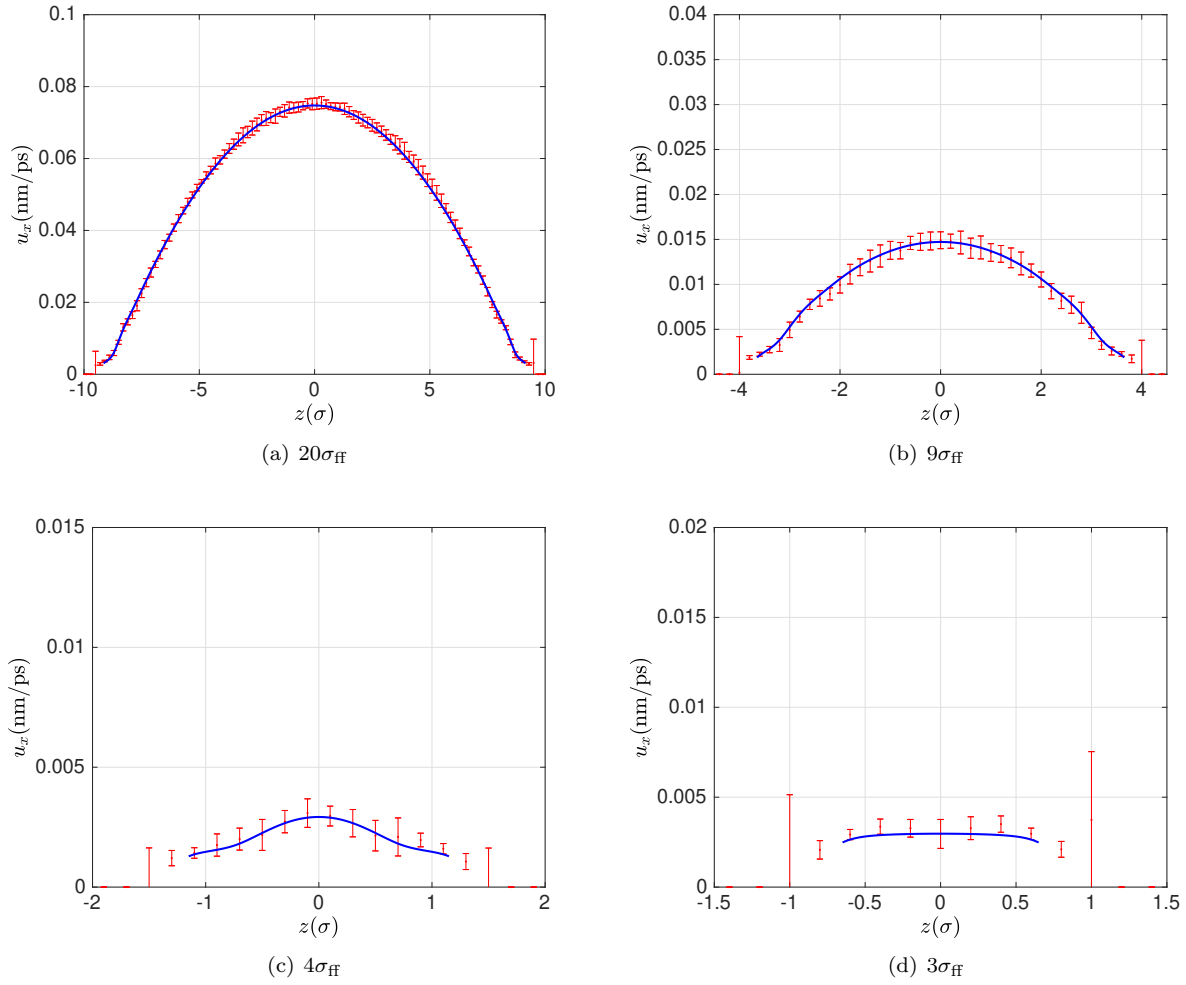

(a) $20\sigma_{\text{ff}}$

(b) $9\sigma_{\text{ff}}$

(c) $4\sigma_{\text{ff}}$

(d) $3\sigma_{\text{ff}}$

Figure 2.7: Velocity profiles for methane confined in silicon slits of size (a) $20\sigma_{\text{ff}}$, (b) $9\sigma_{\text{ff}}$, (c) $4\sigma_{\text{ff}}$ and (d) $3\sigma_{\text{ff}}$. Continuum results are in solid line (blue), while MD results are represented by error bars (red).

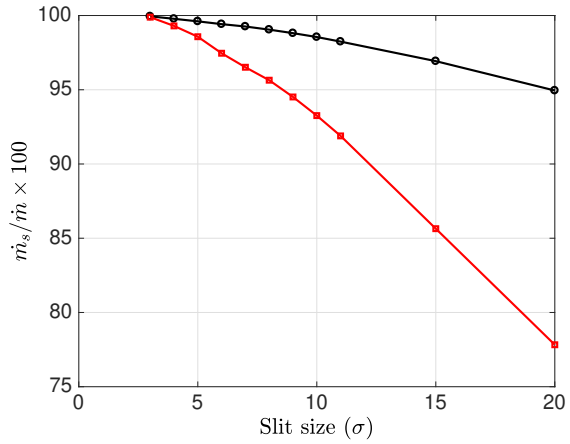

(a) C–CH_4 and C*–CH_4

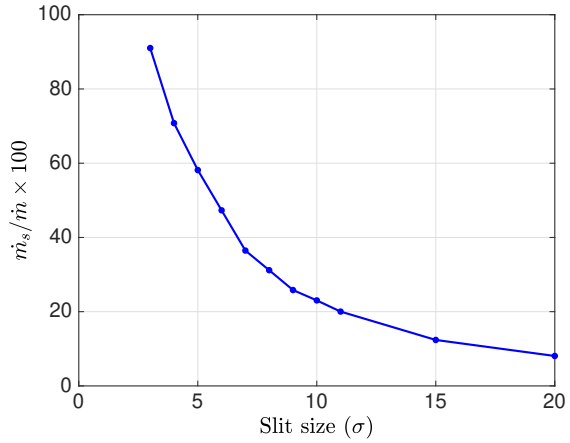

(b) Si–CH_4

Figure 2.8: Percent contribution of slip to mass flow rate (a) C–CH_4 system marked with open circles (black) and C*–CH_4 system with open squares (red) (b) Si–CH_4 system with bold circles. The lines are drawn as a guide to the data points.

Chapter 3

Interfacial Friction based Quasi-Continuum Hydrodynamical Model

In this chapter, we formulate a one-dimensional isothermal hydrodynamic transport model for water, which is an extension to the previous chapter. Viscosity variations in confinement are incorporated by the local average density method. Dirichlet boundary conditions are provided in the form of slip velocity that depends upon the macroscopic interfacial friction coefficient. The value of this friction coefficient is computed using a novel generalized Langevin Equation (GLE) formulation that eliminates the use of equilibrium molecular dynamics (EMD) simulation. Gravity driven flow of SPC/E water confined between graphene and silicon slit shaped nanochannels are considered as examples for low and high friction cases. The proposed model yields good quantitative agreement with the velocity profiles obtained from non-equilibrium molecular dynamics (NEMD) simulations.

3.1 Transport model

The starting point of a one-dimensional gravity driven flow in a slit channel is the Stokes equation

$$\frac{\mathrm{d}}{\mathrm{d}z}\left[\mu(z)\frac{\mathrm{d}u_x(z)}{\mathrm{d}z}\right] + m\rho(z)g_x = 0, \tag{3.1}$$

with boundary conditions

$$u_x\left(-\frac{L}{2}+\delta\right) = u_x\left(+\frac{L}{2}-\delta\right) = u_{\mathrm{s}}, \tag{3.2}$$

where (x, z) are the streaming direction (direction of the flow) and the confined direction, respectively; $u_x(z)$ is the unknown streaming velocity, m is the molecular mass of the fluid, g_x is the applied gravity in the streaming direction, $\rho(z)$ is the number density, $\mu(z)$ is the shear viscosity, and L is the channel width. The channel walls are located at $-L/2$ and $+L/2$. Dirichlet boundary conditions are provided at a distance δ from the wall, where the first fluid layer starts to develop after the void region near the interface, with u_{s} as the slip velocity. The continuity equation is satisfied under the assumption that u_z is identically zero. A

mathematically equivalent set of boundary conditions for the current problem can also be written as

$$A\mu(z)\frac{\mathrm{d}u_x(z)}{\mathrm{d}z}\bigg|_{z=-L/2+\delta} = \zeta_0 u_\mathrm{s}, \tag{3.3a}$$

$$\frac{\mathrm{d}u_x(z)}{\mathrm{d}z}\bigg|_{z=0} = 0, \tag{3.3b}$$

where A is the interfacial area and ζ_0 is the macroscopic interfacial friction coefficient. Eq. (3.3a), although similar to the slip boundary condition presented in Eq. (1.1), describes the force balance at the interface. At the interface, the wall shear force is balanced by the interfacial friction force, which is proportional to the relative velocity between the wall and the fluid (slip velocity). The second condition in Eq. (3.3b) is representative of the symmetry of the velocity profile at the center point of the slit channel. Integrating the Stokes equation (Eq. (3.1)) once in the region $(-L/2+\delta, 0)$ and using Eq. (3.3b), we get

$$-\mu(z)\frac{\mathrm{d}u_x(z)}{\mathrm{d}z}\bigg|_{z=-L/2+\delta} + mg_x \int_{-L/2+\delta}^{0} \rho(z)\mathrm{d}z = 0. \tag{3.4}$$

Now, making use of Eq. (3.3a) and observing that $\rho\left(-L/2, -L/2+\delta\right) = 0$, Eq. (3.4) can be reformulated to obtain an expression for the slip velocity (u_s) as

$$u_\mathrm{s} = A\frac{mg_x}{\zeta_0}\int_{-L/2}^{0} \rho(z)\mathrm{d}z. \tag{3.5}$$

This value of slip velocity can be used as a Dirichlet boundary condition in Eq. (3.2). Inputs required for this framework are density, viscosity, and the interfacial friction coefficient ζ_0. Density can be obtained from the EQT framework discussed in chapter 2. The methods to obtain the remaining inputs are discussed below.

3.1.1 Viscosity profiles

Similar to our previous approach, we compute the shear viscosity of the confined fluid using the LADM [167]. It coarse-grains the local density over one molecular diameter size, and effectively identifies a state of homogeneous fluid $(\bar{\rho}, T)$, for each location z in the confinement. The 1D local average density is calculated as

$$\bar{\rho}(z) = \frac{6}{\sigma_\mathrm{ff}^3}\int_{|z-z'|<\sigma_\mathrm{ff}/2} \left[\left(\frac{\sigma_\mathrm{ff}}{2}\right)^2 - (z-z')^2\right]\rho(z')\,\mathrm{d}z', \tag{3.6}$$

where σ_{ff} is the Lennard-Jones (LJ) diameter of the fluid, and for SPC/E water its value is 0.317 nm. The properties of homogeneous fluids are well understood and can easily be calculated from MD. Although equations of state for these properties exist for LJ type of fluids [41, 103, 170], no comprehensive database or formulae exist for the shear viscosity of bulk water. Therefore, we performed EMD simulations for bulk water and used Green-Kubo formulation to compute the shear viscosity of SPC/E water [49]. Further computational details are provided in Sec. 3.2.

3.1.2 Interfacial friction coefficient

To compute the interfacial friction coefficient ζ_0, we follow the linear response theory approach presented by Huang and Szlufarska in Ref. [71]. We first compute the friction coefficient ζ_0^j of an individual fluid particle j near the interface. Using linear response theory in conjunction with generalized Langevin equation (GLE), the Green-Kubo relation for ζ_0^j can be expressed in terms of equilibrium time correlation functions as

$$\zeta_0^j = \frac{\int_0^\infty \langle f_{x,j}^{\mathrm{wf}}(0) f_{x,j}^{\mathrm{wf}}(t)\rangle \mathrm{d}t}{k_{\mathrm{B}}T + \int_0^\infty \langle v_{x,j}(0) f_{x,j}^{\mathrm{wf}}(t)\rangle \mathrm{d}t}, \tag{3.7}$$

where $f_{x,j}^{\mathrm{wf}}$ and $v_{x,j}$ are the instantaneous streaming direction wall-fluid force and velocity of the particle j near the solid wall. The time correlation in the numerator is the single-particle wall-fluid force autocorrelation function (FACF) and denominator contains wall-fluid force–velocity cross-correlation function (FVCCF). Then, we sum the contributions from all the interfacial fluid particles to obtain the total interfacial friction coefficient ζ_0 as

$$\zeta_0 = \sum_j \zeta_0^j. \tag{3.8}$$

The FACF and FVCCF in Eq. (3.7) can be evaluated either from EMD simulation or any other particle sampling method that can simulate the single-particle dynamical motion of confined fluids in equilibrium. Once the friction coefficient is known, the slip velocity is computed from Eq. (3.5), thereby rendering the model closed.

In this work, we discuss a GLE based simulation approach to compute the interfacial friction coefficient. The description of a particle's motion by a GLE provides a powerful coarse-grained multiscale approach to study its equilibrium correlation functions. GLE describes the motion of a test particle in terms of dissipative

and thermal forces (thermal noise), which are coupled via fluctuation-dissipation (FD) relation [11, 33]. The practical use of GLE can be made to study physical systems provided the memory function that characterizes the dissipative force and the thermal noise autocorrelation, is known apriori. Sanghi and Aluru [143, 144] recently demonstrated that the thermal noise properties in confined fluids do not change significantly across the confinement. Further, thermal noise characteristics in confined fluids are not found to be significantly different than that of the same fluid in the corresponding bulk state. Therefore, the dynamics of confined fluid can be modeled using the noise characteristics of the bulk fluid; and confinement effects can be modeled by a position dependent mean force, which can be obtained from EQT. Using this GLE approach, they simulated the single-particle motion along the confined direction and computed several dynamical quantities (mean-squared displacement, survival probability, velocity autocorrelation function, etc.) at different spatial regions of confined slit channels. The computed quantities were found in good quantitative agreement with those obtained from EMD simulations. With this knowledge, to compute the interfacial friction coefficient, we formulate a two-dimensional (2D) GLE model as

$$m\frac{\mathrm{d}v_{z,j}(t)}{\mathrm{d}t} = -m\int_0^t K(t-t')v_{z,j}(t')\mathrm{d}t' + f_{z,j}^{\mathrm{tot}}(z_j(t)) + R_z(t), \tag{3.9a}$$

$$m\frac{\mathrm{d}v_{x,j}(t)}{\mathrm{d}t} = -m\int_0^t K(t-t')v_{x,j}(t')\mathrm{d}t' + f_{x,j}^{\mathrm{tot}}(x_j(t), z_j(t)) + R_x(t), \tag{3.9b}$$

$$\frac{\mathrm{d}z_j(t)}{\mathrm{d}t} = v_{z,j}(t), \quad \frac{\mathrm{d}x_j(t)}{\mathrm{d}t} = v_{x,j}(t). \tag{3.9c}$$

Here m is the mass of the fluid particle j, while $v_{z,j}$, $v_{x,j}$ are, respectively, the velocities in the confined (z) and streaming (x) directions. Time dependent memory function $K(t)$ characterizes the dissipative force, $f_{z,j}^{\mathrm{tot}}$ and $f_{x,j}^{\mathrm{tot}}$ are the instantaneous forces in z and x directions, respectively, experienced by the particle due to the structural inhomogeneity, while $R_z(t)$ and $R_x(t)$ are the random forces in confined and streaming directions, respectively. The random force satisfies the following statistical properties

$$\langle R_\alpha(t)\rangle = 0, \tag{3.10a}$$

$$\langle v_{\alpha,j}(0)R_\beta(t)\rangle = 0, \tag{3.10b}$$

$$\langle f_{\alpha,j}^{\mathrm{tot}}(0)R_\beta(t)\rangle = 0, \tag{3.10c}$$

$$\langle R_\alpha(0)R_\beta(t)\rangle = mk_{\mathrm{B}}TK(t)\delta_{\alpha\beta}, \tag{3.10d}$$

where α and β are the directions in the 2D system (x and z), and $\delta_{\alpha\beta}$ is the Kronecker delta, which is unity only when $\alpha = \beta$ and zero otherwise. The memory function $K(t)$ in both confined (Eq. (3.9a)) and streaming (Eq. (3.9b)) direction equations is the same. Since the memory function is same in the two directions, the thermal force also has identical statistical properties in both directions (noise is assumed isotropic, Eq. (3.10d)). Also, the memory function for this confined system is assumed to be the same as the memory function of the corresponding bulk water state. To justify this assumption, we compare the memory function $K(t)$ of bulk water and water confined within the first interfacial layer of $4\sigma_{\text{ff}}$ wide silicon slit channel in Fig. 3.2(a). The confined water is in equilibrium with bulk water at density 33.46 molecules/nm^3. It can be observed from the plot that the time decay characteristics and the correlation time of the memory function is not significantly different from corresponding bulk state even under high degree of confinement. The data for the memory function for bulk water is provided in the supplementary information of Ref. [17]. The instantaneous force values on particle j, i.e., $f_{z,j}^{\text{tot}}$ and $f_{x,j}^{\text{tot}}$, are realized from the static mean force maps $F_z^{\text{tot}}(z)$ and $F_x^{\text{tot}}(x,z)$. Since the magnitude of F_z^{tot} is very large near the interface, its variation along x is ignored, and it is directly obtained from EQT as $F_z^{\text{tot}}(z) = -\mathrm{d}U^{\text{tot}}(z)/\mathrm{d}z$. This means that the dynamics along the confined direction is primarily dictated by a 1D GLE formulation (Eq. (3.9a)), as demonstrated by Sanghi and Aluru [143, 144]. However, it is necessary to consider the variation of F_x^{tot} in both directions, since its variation in the streaming direction is necessary to capture the effect of surface corrugations on the friction coefficient, and its magnitude changes very sharply along the confined direction near the interface. Also, the total mean force map along the streaming direction can be approximated as the wall-fluid force map ($F_x^{\text{tot}}(x,z) \approx F_x^{\text{wf}}(x,z)$). This approximation means that the spatial inhomogeneity in the fluid density profile in the streaming direction primarily results due to the variation in the wall-fluid potential. Figures 3.2(b) and 3.2(c) show the comparison of the streaming direction total force and the wall-fluid force profile for graphene-water and silicon-water interfaces, calculated using EMD, at the location of the first density peak. It can be observed that the wall-fluid force profile does not differ significantly from the total force profile near the interface. The advantage of this approximation is that the two-dimensional

wall-fluid force map can be computed analytically using the structure of the wall as

$$U_{\mathrm{3D}}^{\mathrm{wf}}(x,y,z) = \sum_{r_i<R_{\mathrm{cut}}} u_{\mathrm{LJ}}^{\mathrm{wf}}(r_i), \tag{3.11a}$$

$$\frac{\mathrm{d}U_{\mathrm{3D}}^{\mathrm{wf}}}{\mathrm{d}x} = \sum_{r_i<R_{\mathrm{cut}}} \frac{\mathrm{d}u_{\mathrm{LJ}}^{\mathrm{wf}}}{\mathrm{d}r_i}\cdot\frac{x-x_i}{r_i}, \tag{3.11b}$$

$$F_x^{\mathrm{wf}}(x,z) = -\frac{\int_0^{L_y} \frac{\mathrm{d}U_{\mathrm{3D}}^{\mathrm{wf}}}{\mathrm{d}x}\exp(-\beta U_{\mathrm{3D}}^{\mathrm{wf}})\,\mathrm{d}y}{\int_0^{L_y}\exp(-\beta U_{\mathrm{3D}}^{\mathrm{wf}})\,\mathrm{d}y}, \tag{3.11c}$$

where $r_i = ((x-x_i)^2+(y-y_i)^2+(z-z_i)^2)^{1/2}$ is the distance between the wall particle centered at (x_i, y_i, z_i) to the point of interest (x, y, z), $u_{\mathrm{LJ}}^{\mathrm{wf}}$ is the 12–6 LJ wall-fluid interaction potential, $U_{\mathrm{3D}}^{\mathrm{wf}}$ is the three dimensional wall-fluid interaction energy, $\beta = 1/k_{\mathrm{B}}T$, and L_y is the box length in the y direction. The wall particles which are inside the cutoff length $R_{\mathrm{cut}} = 1.4$ nm are considered in the summation, similar to the confined MD simulations. Therefore, all the inputs needed to compute the interfacial friction coefficient are obtained without using computationally expensive EMD. The numerical details to solve 2D GLE model are discussed in Sec. 3.2. We will compare the accuracy of our proposed GLE approach versus the EMD in the results section.

3.2 Simulation Details

Different types of MD simulations are performed in the present work. We used the LAMMPS [123] package in all of our computations. Water-water interactions are described by the SPC/E model [10]. To calculate the electrostatic interactions between water molecules, Particle-Particle Particle-Mesh (PPPM) method is used. First, EMD simulations of bulk water are performed to evaluate the shear viscosity using the Green-Kubo method as [66]

$$\mu = \frac{V}{6k_{\mathrm{B}}T}\int_0^{\infty}\sum_{\alpha}\sum_{\beta\neq\alpha}\langle P_{\alpha\beta}(0)P_{\alpha\beta}(t)\rangle \mathrm{d}t, \tag{3.12}$$

where V is the volume of the simulation box, $P_{\alpha\beta}$ is the off-diagonal stress component, and α, β are the directions in the Cartesian coordinate system (x, y, z). These computations are performed for a range of reduced densities $\rho\sigma_{\mathrm{ff}}^3 = 0.1 - 1.6$ in a NVE ensemble. After that, we computed the time autocorrelation of the off-diagonal stress components and fitted the results to a Gaussian-exponential form to capture the two stage relaxation process of the autocorrelation [49]. We used the resultant fit to compute the integral in

Eq. (3.12). Our computed viscosity values around the state point $\rho\sigma_{\text{ff}}^3 = 1.0$ were found in good agreement (maximum 4% deviation) with the published data for SPC/E model [7]. The density versus viscosity data is then fitted to a cubic Hermite polynomial. The viscosity data along with the coefficients of the cubic Hermite polynomial are provided in the supplementary information of Ref. [17] The resultant fit is then used in conjunction with LADM to estimate viscosity in the confinement by interpolation. The EMD data points and the fit are plotted in Fig. 3.3.

EMD simulations of confined water are performed with two different surfaces representing contrasting levels of interfacial friction. Wall-fluid interactions are modeled by the 12–6 LJ potential. The first system consists of water confined in graphene sheets at 298 K [100], and serves as a low friction case. The carbon-water LJ interaction force-field is taken from Gordillo and Marti [56]. For this force-field, the interactions between the hydrogens of water and carbon are ignored. We also studied the graphene-water and graphite water systems with carbon-water interaction force-field provided by Wu and Aluru [173], which is realistic in terms of reproducing the experimental contact angle between water and graphite surface. The motivation behind the usage of different force-fields is two-fold, which is to test the fidelity of the transport model and to understand the effects of wall-fluid interaction parameters on the flow characteristics. For the second system, water is confined inside a two four-layered rigid silicon walls oriented in [111] direction at 300 K [99], and is representative of high friction type surface. The total number of particles in confined simulations correspond to a reference bulk state of 33.46 molecules/nm^3, and are estimated using the linear superposition approximation [150, 43]. Channel width is defined as the center to center distance between the first layer of wall atoms closest to the fluid. This definition is used to calculate the average channel density ρ_{avg}. The channel widths considered in this work are $20\sigma_{\text{ff}}$, $10\sigma_{\text{ff}}$, $7\sigma_{\text{ff}}$, and $4\sigma_{\text{ff}}$ to test the model accuracy for various length scales. In confined EMD simulations, systems are equilibrated for 5 ns by simulating an NVT ensemble with Nosé–Hoover thermostat [110] with a time constant of 0.2 ps. After that, production run for 10 ns is performed, with data collected every 0.02 ps for calculating the necessary correlations. This data is divided into 1000 similar samples of 10 ps, which serve as ensembles under the ergodic hypothesis, and the resultant correlations are averaged by the number of samples.

For confined NEMD simulations, different magnitudes of gravity field are considered to demonstrate the applicability of the continuum method under the linear response regime, i.e. the velocity profile scales linearly with the applied gravity, and the slip length is independent of the applied gravity [161]. To control the temperature in NEMD simulations, thermostat is only applied to non-streaming directions to prevent any artifacts in the simulation. To perform the ensemble average, 15 identical simulations are performed, differing only in their initial velocity distribution. Each ensemble is simulated for 20 ns, with first 10 ns

discarded to obtain the fully developed, steady-state velocity profile.

In the transport model, the slip plane location (δ) is defined to be the distance from the surface until which the density value is less than 10^{-3} molecules/nm^3. For graphene-water [56] system, this value is 0.27 nm, while for silicon-water system, it is 0.24 nm. The location of the slip plane is dependent upon the thermodynamic state and the force-fields used in the MD simulation. Density profiles are obtained from EQT and its implementation details can be found in Ref. [99]. To compute the interfacial friction, 2D GLE simulations are performed with a time step of 0.01 ps, with the production trajectory of 400 ps, with data saved every other step (0.02 ps). The numerical procedure to obtain the memory function $K(t)$ and the time integration of the GLE are discussed in Ref. [144]. First 100 ps of the simulation trajectory was discarded to allow the equilibration of the fluid particle. We used $\sim 2 \times 10^4$ instances of particle trajectories to compute the time correlations in Eq. (3.7).

A typical GLE simulation for 100 ps equilibration and 400 ps production run takes about 144 seconds in CPU time. In contrast, a typical EMD simulation is orders of magnitude slower (approximately 24 CPU hours to simulate a 500 ps run for graphene water $10\sigma_{\text{ff}}$ system). Also, as GLE is a single particle formulation, it can be run on a personal workstation, as opposed to EMD/NEMD, which require suitable parallelization and High Performance Computing Cluster environments to reduce the wall-time. The continuum formulation typically takes 3-4 seconds as compared to NEMD, where meaningful data for velocity profiles requires 53350 CPU hours of production runs. Therefore, our GLE/continuum framework provides a massive speedup over NEMD to obtain the velocity profiles.

3.3 Results

In this section, we test the efficacy of the current framework by comparing the velocity profiles predicted from the model with those obtained from NEMD simulations. We also compare the accuracy of the correlation functions obtained using the proposed GLE approach with the EMD results.

3.3.1 Interfacial friction coefficient

For EMD calculations of the friction coefficient, a perpendicular distance of $1\sigma_{\text{ff}}$ from the wall in the confined direction is chosen as cutoff distance, and the region between the wall and the cutoff distance is defined as interfacial region. Initial time occupancy based tagging [122, 143] is used to compute the time correlations. This means that only the particles that are present in the interfacial region at an initial time contribute to the interfacial friction. This is done because for large cutoff lengths, the friction coefficient will include both

the viscous and the slip effects and therefore will not remain an intrinsic property of the wall-fluid interface, as assumed in the formulation. This point has been discussed in detail by Hansen et al. [64] Also, Huang and Szlufarska [71] have acknowledged the issue, and have verified the formulation by computing the friction coefficient inside 2 molecular diameter wide channel, where the entire body of the fluid becomes a wall-fluid interface. In GLE, the single particle friction is multiplied by the average number of particles in the cutoff region instead of the summation, which is obtained from the 1D density profiles. We show the comparison of the single-particle force autocorrelation function (FACF) calculated from EMD and GLE formulations for graphene [56] and silicon walls in Figs. 3.4(a) and 3.4(b), respectively. It can be observed from these figures that the correlations computed from the GLE trajectories are in good quantitative agreement to their EMD counterpart. Silicon interface offers higher friction than graphene [13], which is clearly evident from the FACF plots where its variance is significantly higher in the case of silicon. Figure 3.4(c) displays the comparison of the FVCCF for the two interfaces as obtained from GLE and EMD simulations. It can be observed from the plot that the silicon interface presents a strong short-time force–velocity cross-correlation which is captured accurately by GLE based dynamics. However, the FVCCF for graphene water interface is almost negligible. As a result, the contribution to the friction coefficient from the FVCCF term is only significant (in comparison to the thermal energy $k_{\mathrm{B}}T \approx 2.5$ kJ/mol) for the silicon interface (with integral value -0.536 kJ/mol), as compared to graphene interface (with integral value -0.018 kJ/mol). The reason for this difference can be understood from Figs. 3.2(b) and 3.2(c), which show the variation of the streaming direction wall-fluid force for the two interfaces. It can be observed that both the magnitude and the period of the wall-fluid force is smaller for graphene in comparison to silicon, leading to a very small residence time of the water molecule near the graphene interface (~ 0.2 ps). Therefore, the motion of water molecule in the streaming direction for graphene interface is thermal noise dominant, giving rise to a significantly smaller contribution to the FVCCF. Table 3.1 shows the comparison of the friction coefficient computed using the GLE approach with those obtained from EMD simulations. Assuming the EMD value as a benchmark, the deviation in the friction coefficient calculated from the GLE is within 3%. Thus, the proposed GLE formulation provides a robust and computationally efficient alternative to compute the interfacial friction.

3.3.2 Poiseuille flow velocity profiles

To compare the accuracy of our transport model, NEMD simulations of confined water in graphene and silicon surfaces are used as a benchmark. Using our approach, we first seek to address the important question of relative contributions of viscous and slip flow in the velocity profile. After the friction coefficient is

calculated, we compute the slip velocity u_s by using Eq. (3.5) and solve the transport model. As expected, smooth surfaces (low interfacial friction) will enhance the relative motion between the wall and the adjoining fluid layer, rendering slip as the dominant transport mechanism. This is reflected in the plug-like velocity profiles of water in graphene nanochannels as shown in Figs. 3.5(a)-3.5(d). For atomistically rough surfaces (high interfacial friction), such as water confined within silicon walls, the role of viscosity becomes more important as seen from Figs. 3.6(a)-3.6(d). Increased corrugations on silicon surface hinder the motion of adjacent fluid layer considerably, and transport is dominated by viscous flow. Density and viscosity variations in the current framework capture the non-parabolic velocity profiles, which is more pronounced near the interface and can be seen clearly in narrower channels such as $7\sigma_{ff}$ (Fig. 3.6(c)), and $4\sigma_{ff}$ (Fig. 3.6(d)). It can also be observed that for $4\sigma_{ff}$ wide channel, significant velocity gradient reversals are present in NEMD profile, which are not captured accurately using the LADM calculated viscosity. For smaller channels with dominant viscous contributions, the use of LADM to capture non-local effects of viscosity might not suffice. In such instances, a transport model with strict non-local constitutive relationship between the stress and strain rate can be utilized to rectify these discrepancies [162, 163, 53, 42]. Approximating density and viscosity as a constant value would fail to capture this non-parabolic behavior, and therefore should be avoided.

3.3.3 Slip length

We computed the slip length l_s using the velocity profiles obtained from the continuum model, defined through Eq. (1.1) for graphene (from force-fields of Gordillo and Marti [56]) and silicon, and report these values in Table 3.2. We also compare these values to the one obtained from EMD method. We observe that the computed slip length is nearly constant for a specific liquid-solid interface at a particular thermodynamic state. This observation can be utilized to identify slip length as a single parameter capable of characterizing the surface-fluid transport properties. The value of slip length of water on graphene surface is in accordance with the previous findings summarized by Kannam et al. in Table 1 of Ref. [82]. Using the force-field provided by Wu and Aluru [173], it is observed that the slip length decreases from 45 nm to 32 nm (ζ_0 = 180.26 kJ-ps/mol/nm^2) for the graphene-water interface. This is due to the increased hydrophilic nature of the interaction parameters resulting in higher interfacial friction, and is clear from Fig. 3.7(a), where the same value of applied gravity (10^{-4} nm/ps^2) in $20\sigma_{ff}$ channel yields a smaller value of slip velocity (compare to Fig. 3.5(a)). The slip length further decreases to 27 nm (ζ_0 = 221.79 kJ-ps/mol/nm^2) for graphite water interface (see Fig. 3.7(b) for velocity profile), owing to the increased attraction between the wall and the fluid due to the addition of an extra wall layer. Based on these observations, we conclude that the wall-fluid

interaction parameters significantly affect the slip length and the velocity profile, and the proposed interfacial friction based model is able to capture this phenomenon with high fidelity.

Contrary to our findings, there are studies that report slip length dependence on channel width [154, 64, 90], which saturates to a constant slip length value for channel widths greater than $20\sigma_{\mathrm{ff}}$. We interpret that these findings might stem from treatment of the problem keeping the pore average density ρ_{avg} as a constant while varying the channel width, which changes the thermodynamic state of the fluid across the channels. We argue that the slip length would remain constant when the following conditions are met

1. The thermodynamic state of the fluid inside the channels is consistent, i.e., the chemical potential across the confinement is constant for all channel widths.
2. Density and viscosity variations are accounted appropriately in the transport model.
3. The applied gravity value does not drive the flow out of the linear response regime [161].

In addition to the above requirements, caution must be exercised while studying very small channel widths. A typical limit on the applicability of our method would be the cases where the wall-fluid potentials from the two confining walls overlap considerably. As discussed in detail by Kumar and Bhatia in Ref. [2], when the channel width is decreased, the wall-fluid potential well becomes deeper to a minimum, after which it rises again. A so called "levitation effect" occurs at the transition point, where the assistance to the transport is maximum, i.e., the fluid particle achieves super-mobility. Below this critical size of the channel, the particle motion is hindered. A rough estimate of this critical dimension neglecting the effects of kinetic energy is given as $L \sim 2(2^{1/6})\sigma_{\mathrm{wf}}$. Since the channel widths considered here are above this critical dimension, we have not observed this effect in the present study.

3.3.4 Couette flow velocity profile

For shear driven (Couette) flow, the flow is induced by moving the confining walls in the streamwise direction. In this case, the governing equation reduces to

$$\frac{\mathrm{d}}{\mathrm{d}z}\left[\mu(z)\frac{\mathrm{d}u_x(z)}{\mathrm{d}z}\right] = 0, \tag{3.13}$$

with boundary conditions

$$u_x\left(-\frac{L}{2}+\delta\right) = u_{\mathrm{s1}}, \tag{3.14a}$$

$$u_x\left(+\frac{L}{2}-\delta\right) = u_{\mathrm{s2}}. \tag{3.14b}$$

Following a force balance on the two interfaces, the following expression for the slip velocities u_{s1} and u_{s2} is obtained

$$u_{s1} = \frac{(1 + I_\mu \zeta_0/A)u_{w1} + u_{w2}}{2 + I_\mu \zeta_0/A}, \tag{3.15a}$$

$$u_{s2} = \frac{(1 + I_\mu \zeta_0/A)u_{w2} + u_{w1}}{2 + I_\mu \zeta_0/A}, \tag{3.15b}$$

where u_{w1} and u_{w2} are the velocities of the wall and $I_\mu = \int_{-L/2+\delta}^{+L/2-\delta} 1/\mu(z)\mathrm{d}z$. We plot and compare the shear driven flow velocity profiles for a $20\sigma_{ff}$ wide graphene channel obtained from the model with those from NEMD simulations in Fig. 3.8, and observe a good agreement. Here, we have used the value of interfacial friction obtained using the GLE simulation. This means that the liquid-solid interfacial friction is an intrinsic property of the interface, and is independent of the flow situation.

In this chapter, we have developed a continuum based hydrodynamic transport model for gravity driven flow of water in slit shaped nanochannels. The boundary condition is formulated in the form of a slip velocity, which is dependent on the interfacial friction coefficient. The friction coefficient provides the atomistic to continuum bridge by incorporating the effect of the lattice structure and the nature of wall-fluid interactions. It is estimated using the wall-fluid force autocorrelation and force-velocity cross-correlation functions, which are computed using a GLE based dynamical framework. The correlations computed using the GLE model are in good agreement with those computed using EMD simulations of confined fluid. Furthermore, it is revealed from the velocity profiles that the slip length is invariant with channel width under certain conditions, and therefore it can serve as the single transport parameter characterizing the surface-fluid interaction for a fixed thermodynamic state.

Table 3.1: Friction coefficient ζ_0 (kJ-ps/mol/nm^2)

Surface	EMD	GLE
Graphene Water [56]	123.73	125.14
Silicon Water	4.05×10^4	3.93×10^4

Table 3.2: Slip lengths (nm) of water on different interfaces. CVG is an abbreviation for Continuum Velocity Gradient method (Eq. (1.1)), and EMD value is computed using $l_s = A\mu(-L/2 + \delta)/\zeta_0$

System	$20\sigma_{ff}$		$10\sigma_{ff}$		$7\sigma_{ff}$		$4\sigma_{ff}$	
	CVG	EMD	CVG	EMD	CVG	EMD	CVG	EMD
Graphene [56]	44.52	45.19	44.50	45.19	44.47	45.19	44.60	45.27
Silicon	0.33	0.32	0.33	0.32	0.33	0.32	0.36	0.34
Graphene [173]	31.32	31.77	—	—	—	—	—	—
Graphite [173]	26.31	26.69	—	—	—	—	—	—

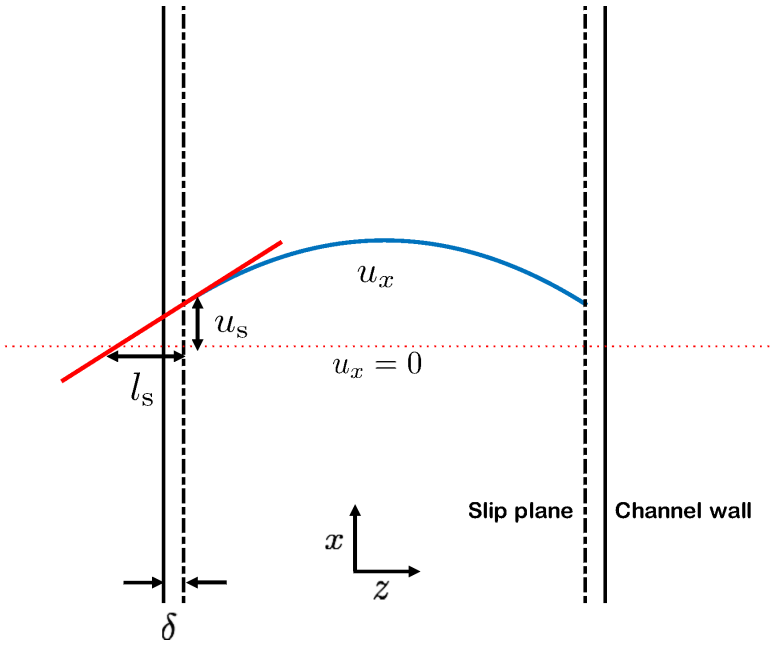

Figure 3.1: Schematic plot of the 1D transport problem illustrating slip velocity u_s and slip length l_s.

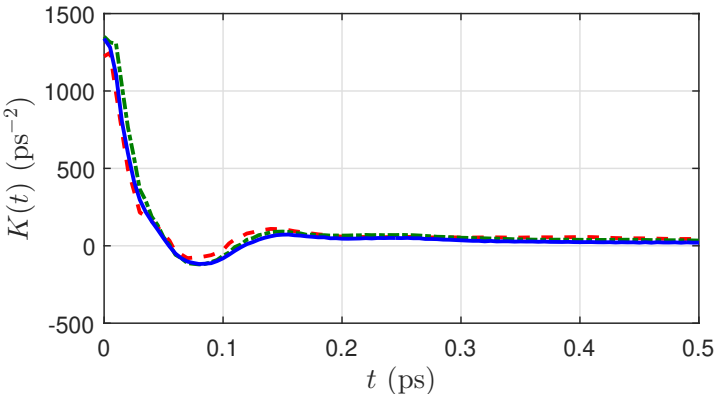

(a) Memory function

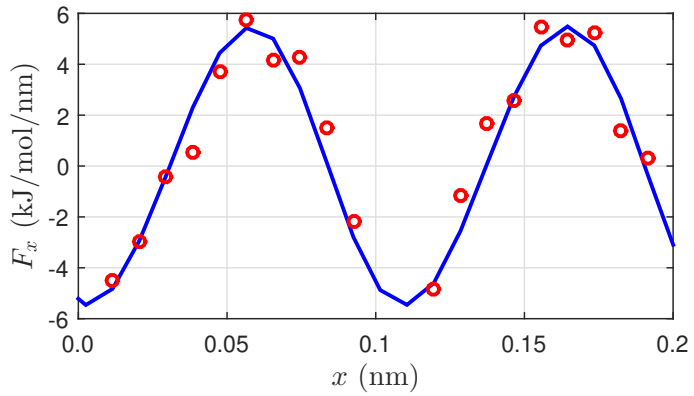

(b) Graphene-Water

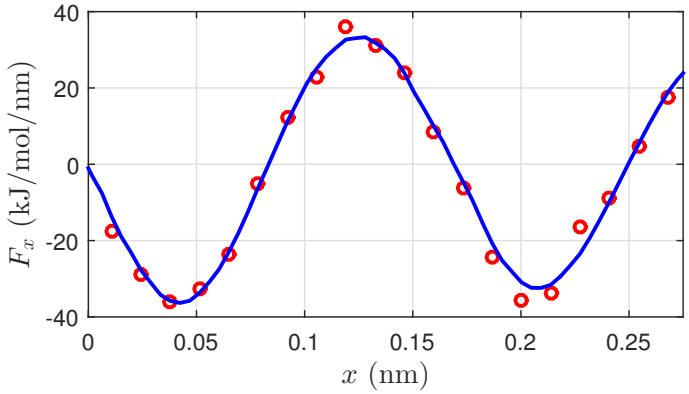

(c) Silicon-Water

Figure 3.2: Memory function of SPC/E bulk water (blue line) at 298 K and density 33.46 molecules/nm^3. Also plotted are memory function of water in the streaming (green dash-dot line) and confined (red dashed line) direction for $4\sigma_{\text{ff}}$ wide Silicon-water system. Mean wall-fluid (solid blue line) and total (red open circles) force in the streaming direction for (b) graphene-water, and (c) silicon-water interface.

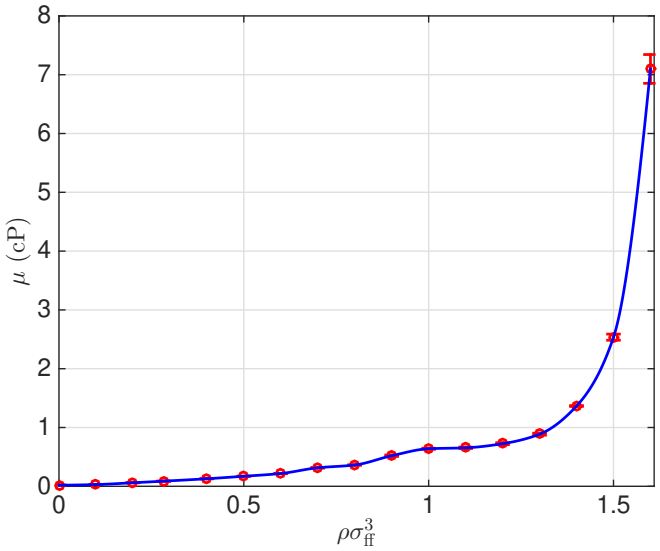

Figure 3.3: Viscosity variation of SPC/E water in centiPoise units (cP) with reduced density at 298K. Open circles (red) represent EMD data points, while solid line (blue) represents Cubic Hermite interpolation. Error bars in EMD data are of the size of the circles, except for $\rho\sigma_{\mathrm{ff}} = 1.6$.

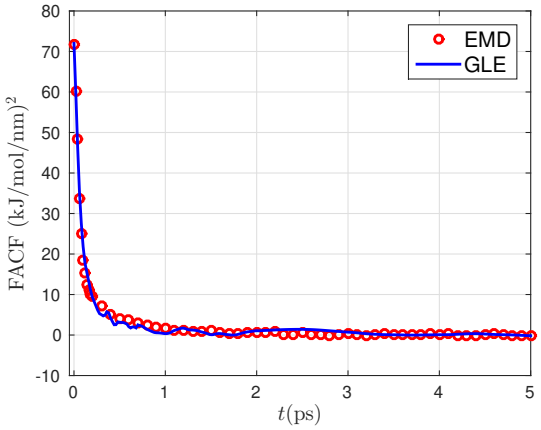

(a) Graphene-Water FACF

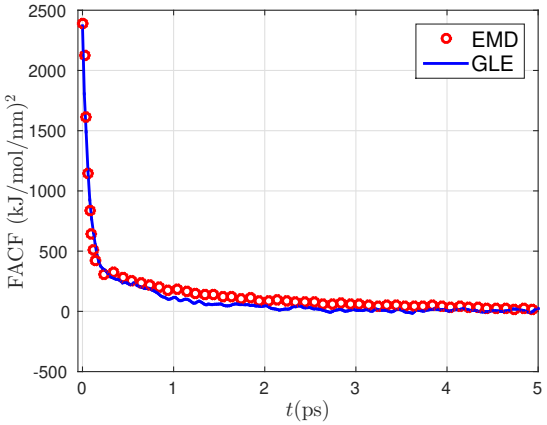

(b) Silicon-Water FACF

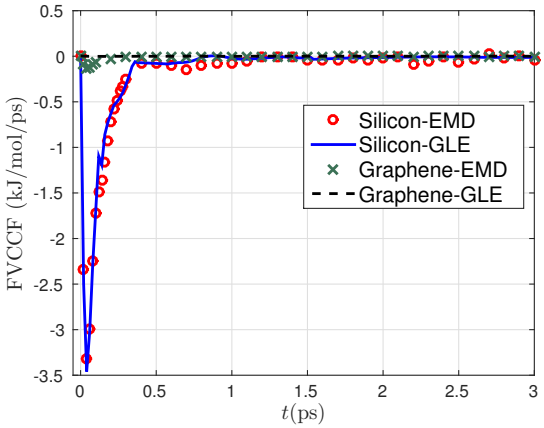

(c) FVCCF

Figure 3.4: Wall-fluid FACF from GLE (bold line, blue) and EMD (circles, red) for (a) graphene-water [56] and (b) silicon-water interfaces. (c) FVCCF from GLE and EMD for water with graphene and silicon interfaces.

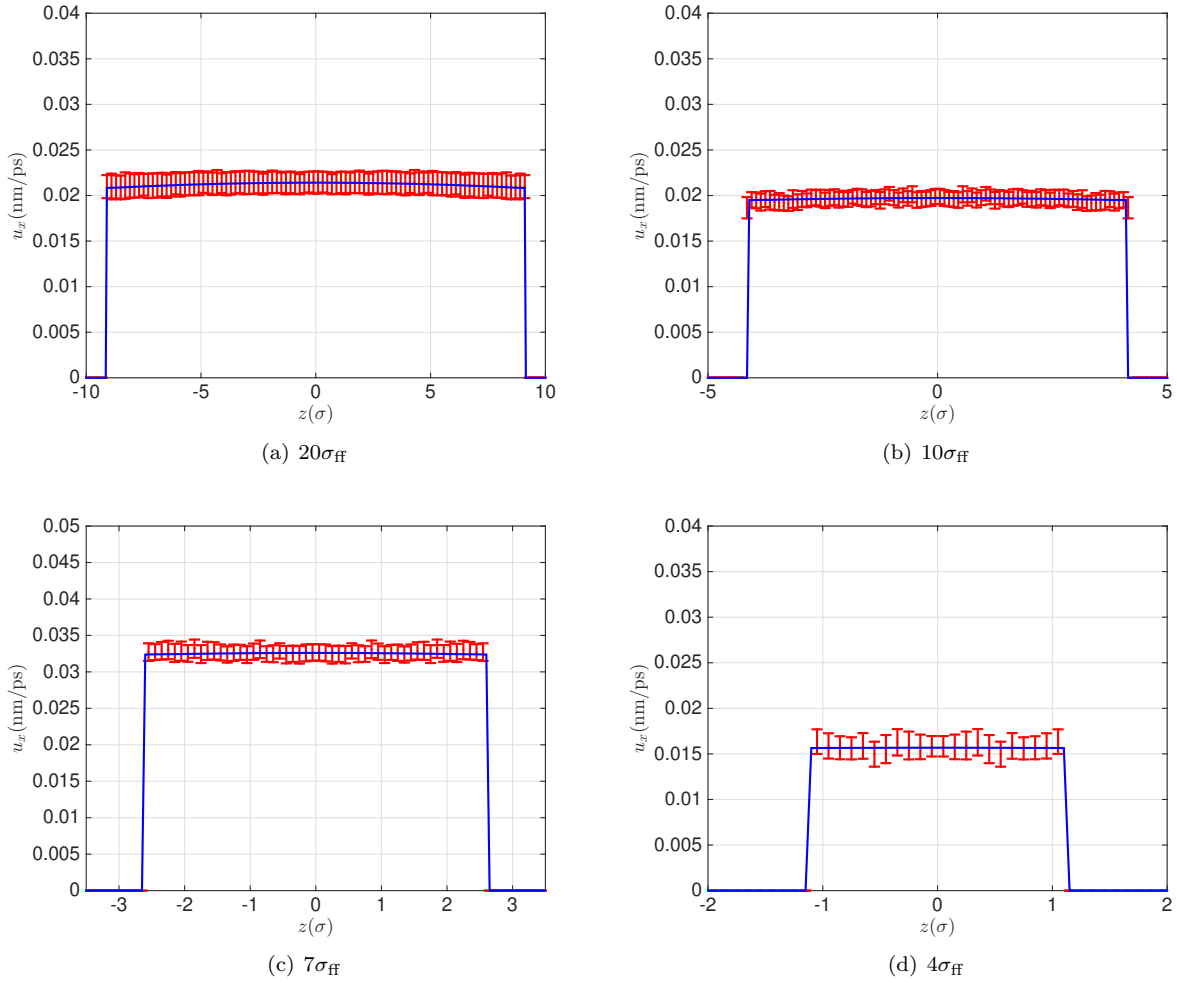

(a) $20\sigma_{\text{ff}}$ (b) $10\sigma_{\text{ff}}$

(c) $7\sigma_{\text{ff}}$ (d) $4\sigma_{\text{ff}}$

Figure 3.5: Velocity profiles of water in graphene slits of size (a) $20\sigma_{\text{ff}}$ for $g_x = 1 \times 10^{-4}$ nm/ps^2, (b) $10\sigma_{\text{ff}}$ for $g_x = 2 \times 10^{-4}$ nm/ps^2, (c) $7\sigma_{\text{ff}}$ for $g_x = 5 \times 10^{-4}$ nm/ps^2 and (d) $4\sigma_{\text{ff}}$ for $g_x = 5 \times 10^{-4}$ nm/ps^2 using force-field of carbon-water from Gordillo and Marti [56]. Continuum results are in solid line (blue), while MD results are represented by error bars (red).

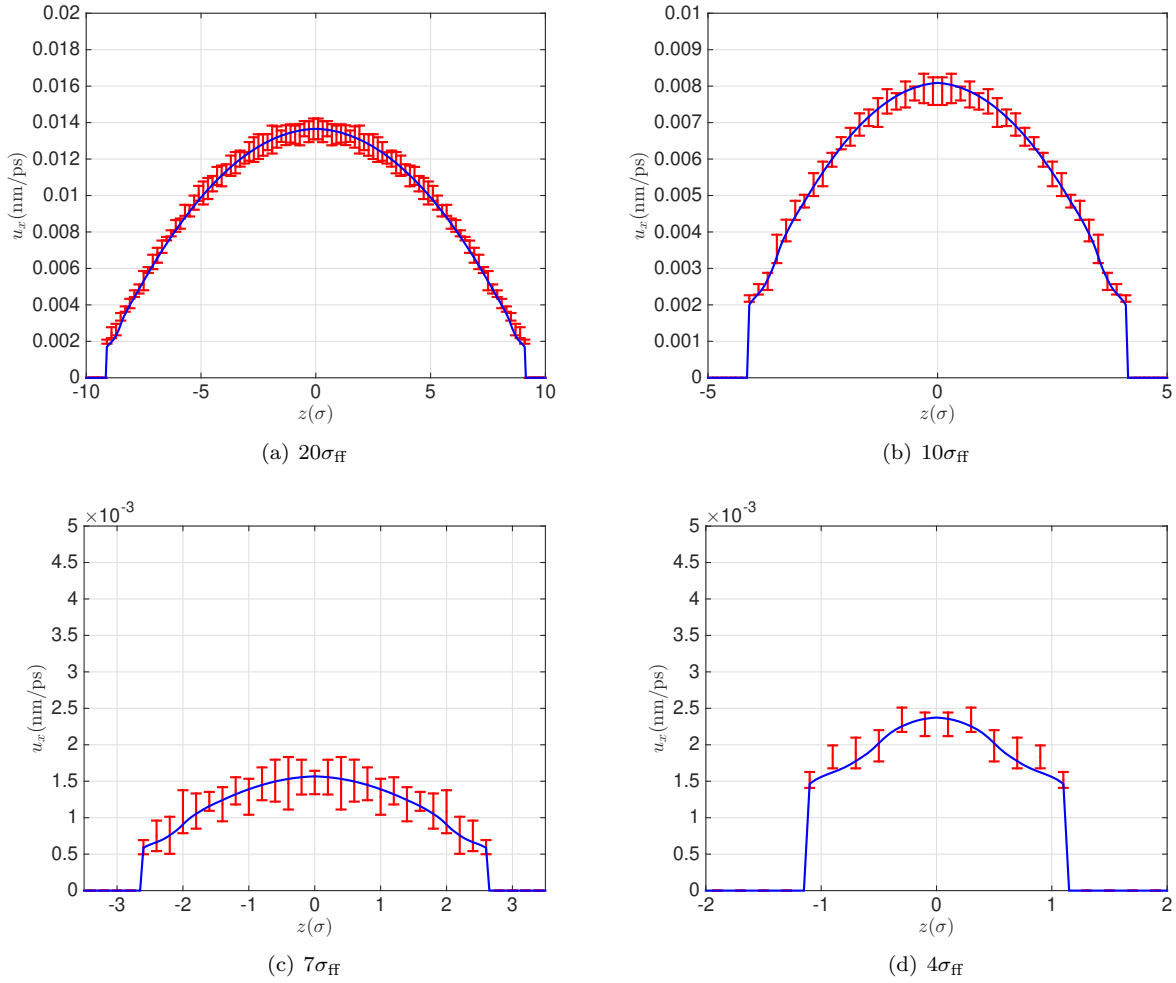

(a) $20\sigma_{\text{ff}}$ (b) $10\sigma_{\text{ff}}$

(c) $7\sigma_{\text{ff}}$ (d) $4\sigma_{\text{ff}}$

Figure 3.6: Velocity profiles of water in silicon slits of size (a) $20\sigma_{\text{ff}}$ for $g_x = 2 \times 10^{-3}$ nm/ps^2, (b) $10\sigma_{\text{ff}}$ for $g_x = 5 \times 10^{-3}$ nm/ps^2, (c) $7\sigma_{\text{ff}}$ for $g_x = 2 \times 10^{-3}$ nm/ps^2 and (d) $4\sigma_{\text{ff}}$ for $g_x = 5 \times 10^{-3}$ nm/ps^2. Continuum results are in solid line (blue), while MD results are represented by error bars (red).

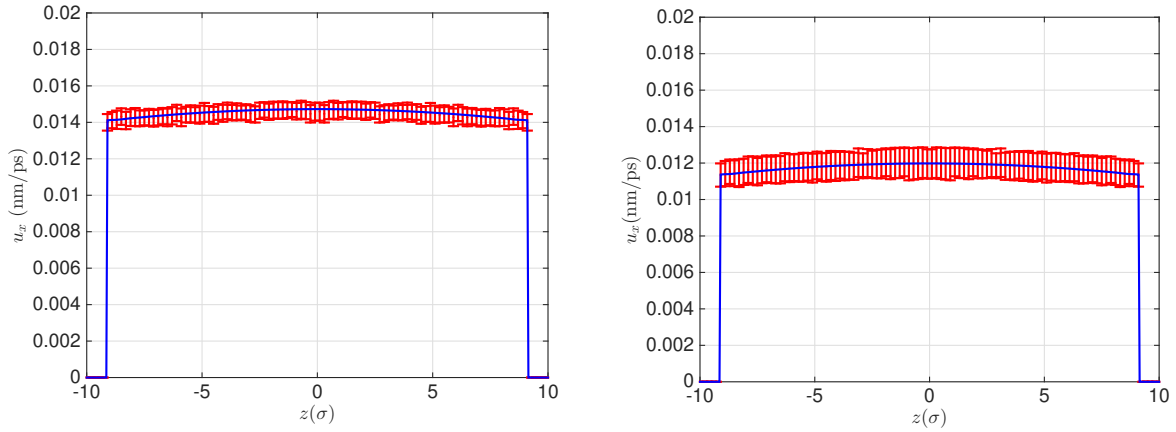

(a) Graphene-Water

(b) Graphite-Water

Figure 3.7: Velocity profiles of water in $20\sigma_{\text{ff}}$ wide (a) graphene, and (b) graphite slits using force-field of carbon-water from Wu and Aluru [173], for $g_x = 10^{-4}$ nm/ps^2. Continuum results are in solid line (blue), while MD results are represented by error bars (red).

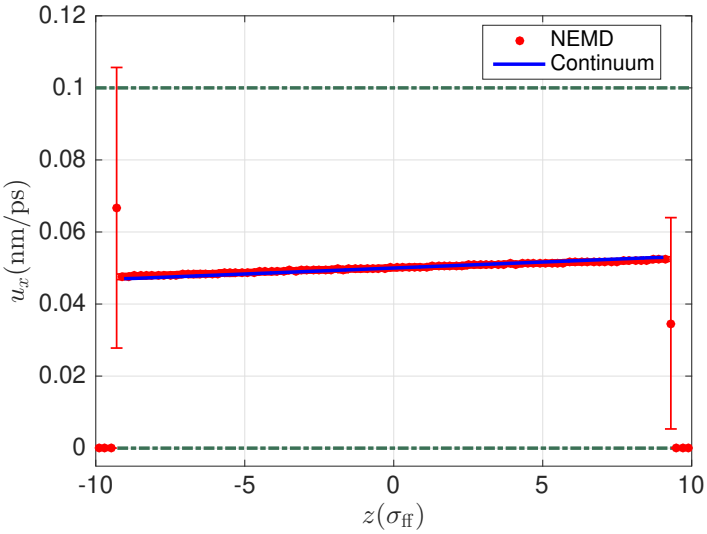

Figure 3.8: Couette flow velocity profiles of water in $20\sigma_{\mathrm{ff}}$ wide channel with $u_{\mathrm{w1}} = 0.1$ nm/ps and $u_{\mathrm{w2}} = 0.0$ nm/ps. Continuum results are in solid line (blue), while MD results are represented by error bars (red). The wall velocity is indicated by green dashed lines.

Chapter 4

Gravity Driven Transport of Binary Mixtures Confined in Nanochannel

In this chapter, we propose a one-dimensional isothermal hydrodynamic transport model for non-reacting binary mixtures in slit shaped nanochannels. The coupled species momentum equations contain viscous dissipation and interspecies friction term of Maxwell-Stefan form. Species partial viscosity variations in the confinement are modeled using the van der Waals one fluid approximation and the local average density method. Species specific macroscopic friction coefficient based Robin boundary conditions are provided to capture the species wall slip effects. The value of this friction coefficient is computed using a species specific generalized Langevin formulation. Gravity driven flow of methane-hydrogen and methane-argon mixtures confined between graphene slit shaped nanochannels are considered as examples. The proposed model yields good quantitative agreement with the velocity profiles obtained from the non-equilibrium molecular dynamics simulations. The mixtures considered are observed to behave as single species pseudo fluid, with the interfacial friction displaying linear dependence on molar composition of the mixture. The results also indicate that the different species have different slip lengths, which remain unchanged with the channel width.

4.1 Species momentum conservation

The 1D momentum equation for an arbitrary species α of an isothermal, non-reacting binary mixture can be written as [84, 86, 24, 19, 85]

$$\frac{\mathrm{d}}{\mathrm{d}z}\left[\mu_{\alpha}^{\mathrm{P}}\frac{\mathrm{d}u_{\alpha}}{\mathrm{d}z}\right]+m_{\alpha}\rho_{\alpha}g_{\alpha}+\sum_{\substack{\beta=1\\ \beta\neq\alpha}}^{2}\frac{k_{\mathrm{B}}T\rho_{\alpha}\rho_{\beta}}{\rho_{t}D_{\alpha\beta}}\left(u_{\beta}-u_{\alpha}\right)=0, \tag{4.1}$$

where z is the direction of the confinement, $u_{\alpha}(z)$ and $u_{\beta}(z)$ are the unknown streaming direction (x) velocity fields, while $\rho_{\alpha}(z)$ and $\rho_{\beta}(z)$ are the concentration fields of the species $\alpha=1,2;\ \beta=1,2$ inside the slit channel, $\rho_{t}(z)=\sum_{\alpha}\rho_{\alpha}(z)$ is the mixture density, m_{α} is the molecular mass, g_{α} is the applied gravity in the streaming direction of the species α, k_{B} is the Boltzmann constant and T is the temperature. The partial

viscosity $\mu_\alpha^{\mathrm{P}}(z)$ is used to characterize the intra-species momentum transfer. The variable $D_{\alpha\beta}(z)$ is the binary Maxwell-Stefan diffusivity, the inverse of which is understood as interspecies friction between species α and β. It should be noted that the interspecies friction term in Eq. (4.1) contains the total contribution of all pairs of α and β species, in a generalized multicomponent case. The binary diffusivities are symmetric, i.e., they follow $D_{\alpha\beta} = D_{\beta\alpha}$, so therefore for a two component system there is only one diffusivity characterizing the interspecies friction. The derivation of the 1D transport equation from a complete 3D form is presented in Appendix A. The FBC's are applied at the slip plane located at $z = -L/2 + \delta$, where $\delta = \max(\delta_1, \delta_2)$, and δ_1 and δ_2 denote the nearest distance from the wall where species number densities are greater than a specified tolerance value ρ_{tol}. The FBC can be written as

$$A\mu_\alpha^{\mathrm{P}}(z)\frac{\mathrm{d}u_\alpha(z)}{\mathrm{d}z}\bigg|_{z=-L/2+\delta} = \zeta_\alpha u_{\alpha\mathrm{s}}, \tag{4.2}$$

where A is the interfacial area and ζ_α is the macroscopic interfacial friction coefficient for species α. The FBC describes the species force balance at the interface, where the wall shear force is balanced by the interfacial friction force that is proportional to the relative velocity between the wall and the fluid (slip velocity). In addition to the FBC, a second condition that is representative of the symmetry of the velocity profiles at the center point of the slit channel can be written as

$$\frac{\mathrm{d}u_\alpha(z)}{\mathrm{d}z}\bigg|_{z=0} = 0. \tag{4.3}$$

Inputs required for this framework are density, viscosity, Maxwell-Stefan diffusivity, and the interfacial friction coefficient for both components. The methods to obtain these inputs are discussed below.

4.1.1 Viscosity and Maxwell-Stefan diffusivity

To capture the viscosity variation along the confined direction, we use the LADM [27, 28, 167] on species density profiles to obtain the coarse grained density as

$$\bar{\rho}_\alpha(z) = \frac{6}{\sigma_{\alpha\alpha}^3}\int\limits_{|z-z'|<\sigma_{\alpha\alpha}/2}\left[\left(\frac{\sigma_{\alpha\alpha}}{2}\right)^2 - (z-z')^2\right]\rho_\alpha(z')\,\mathrm{d}z', \tag{4.4}$$

where $\sigma_{\alpha\alpha}$ is the LJ diameter of species α. The coarse grained density $\bar{\rho}_\alpha$ along with temperature T provides an equivalent thermodynamic state of the species in a locally homogeneous mixture. The potential parameters of a pseudo LJ fluid, which has the same thermodynamic properties (excess potential energy and

compressibility) as that of the homogeneous mixture, are computed using the vdW1 approximation [29], as

$$m_{\mathrm{f}} = \sum_{\alpha=1}^{2} \chi_\alpha m_\alpha, \tag{4.5a}$$

$$\sigma_{\mathrm{f}}^3 = \sum_{\alpha=1}^{2}\sum_{\beta=1}^{2} \chi_\alpha \chi_\beta \sigma_{\alpha\beta}^3, \tag{4.5b}$$

$$\epsilon_{\mathrm{f}}\sigma_{\mathrm{f}}^3 = \sum_{\alpha=1}^{2}\sum_{\beta=1}^{2} \chi_\alpha \chi_\beta \epsilon_{\alpha\beta}\sigma_{\alpha\beta}^3, \tag{4.5c}$$

where $\chi_\alpha = \bar{\rho_\alpha}/\bar{\rho}$ is the molar fraction of species α, $\bar{\rho} = \sum_\alpha \bar{\rho_\alpha}$ being the total homogeneous mixture density; and m_{f}, σ_{f} and ϵ_{f} are the mass, LJ diameter and LJ energy parameter of the pseudo LJ fluid. Lorentz-Berthelot (LB) combination rules are used to obtain the cross parameters $\sigma_{\alpha\beta}$ and $\epsilon_{\alpha\beta}$. Once the homogeneous pseudo fluid state of the mixture is characterized, we computed its viscosity to use as mixture viscosity following the correlations provided by Galliéro et al. [51], that have strong foundation of the comprehensive dataset provided by Meier et al. [104]. These correlations are summarized as

$$\mu_{\mathrm{f}} = \mu_0 + \Delta\mu^*\left(T^*, \bar{\rho}^*\right)\frac{\sigma_{\mathrm{f}}^2}{\sqrt{m_{\mathrm{f}}\epsilon_{\mathrm{f}}}}, \tag{4.6a}$$

$$\mu_0 = \frac{5}{16\sigma_{\mathrm{f}}^2}\sqrt{\frac{m_{\mathrm{f}}k_{\mathrm{B}}T}{\pi}}\frac{f_\mu}{\Omega^{(2,2)}}, \tag{4.6b}$$

$$\Delta\mu^* = b_1[e^{b_2\bar{\rho}^*} - 1] + b_3[e^{b_4\bar{\rho}^*} - 1] + \frac{b_5}{(T^*)^2}[e^{b_6\bar{\rho}^*} - 1]. \tag{4.6c}$$

The dilute gas viscosity μ_0 is at the vanishing density limit, and density dependent residual viscosity $\Delta\mu^*$ is added to get the mixture viscosity μ_{f}. LADM and vdW1 methods are used to evaluate the reduced homogeneous density $\bar{\rho}^* = \bar{\rho}\sigma_{\mathrm{f}}^3$ and reduced temperature $T^* = k_{\mathrm{B}}T/\epsilon_{\mathrm{f}}$. The collision integral $\Omega^{(2,2)}$, and variable f_μ are discussed in Ref. [117]. The coefficients b_γ, where $\gamma = 1, 2 \ldots 6$, are provided in Table 1 of Ref. [51]. To compute the local partial viscosities μ_α^{P}, we adopt the approach of Bhatia and Nicholson [24, 19]. In their method, the shear stress of the homogeneous mixture is assumed to be equal to the sum of species stresses, yielding the relation $\mu_\alpha^{\mathrm{P}} = \omega_\alpha\mu_{\mathrm{f}}$, where ω_α is the mass fraction of species α, and is computed using the species coarse grained density $\bar{\rho}_\alpha$ from Eq. (4.4). There also exist alternative semi-empirical methods to compute partial viscosities of a binary mixture [169, 85], with limited accuracy for mixtures of heavy and light gases [26].

To compute the interspecies diffusion coefficient D_{12}, we adopt the method proposed by Reis et al. [139]. Their correlations are generic for LJ chain fluids, so we provide a simplified expression for monoatomic LJ

fluids as

$$D_{12} = \frac{D_0}{\left(\frac{g(\bar{\rho})}{R(\hat{\rho},\ \hat{T})} + \frac{0.04}{\hat{T}^{1.5}}\right)}; \tag{4.7a}$$

$$D_0 = \frac{3}{8\bar{\rho}\sigma_{12}^2}\left(\frac{k_{\mathrm{B}}T}{2\pi m_{12}}\right); \tag{4.7b}$$

$$g(\bar{\rho}) = \frac{1}{1-\xi_3} + \frac{3\sigma_{11}\sigma_{22}}{(\sigma_{11}+\sigma_{22})}\frac{\xi_2}{(1-\xi_3)^2} + 2\left[\frac{\sigma_{11}\sigma_{22}}{(\sigma_{11}+\sigma_{22})}\right]^2\frac{\xi_2^2}{(1-\xi_3)^3}; \tag{4.7c}$$

$$\xi_l = \frac{\pi}{6}\bar{\rho}\sum_{\alpha=1}^{2}\chi_\alpha\sigma_{\alpha\alpha}^l,\ \text{for } l = 2,3; \tag{4.7d}$$

$$R(\hat{\rho},\ \hat{T}) = \left(1 - \frac{\hat{\rho}}{1.12\hat{T}^{0.2}}\right)\left[1 + 0.97\hat{\rho}^{0.5} + 5.1\hat{\rho}^2 + \frac{3.1\hat{\rho} - 2.9\hat{\rho}^{0.5}}{\hat{T}^{1.5}}\right]\ \exp\left(-\frac{\hat{\rho}}{2\hat{T}}\right); \tag{4.7e}$$

$$\hat{T} = k_{\mathrm{B}}T/\hat{\epsilon};\quad \hat{\epsilon} = \sum_{\alpha=1}^{2}\sum_{\beta=1}^{2}\chi_\alpha\chi_\beta\epsilon_{\alpha\beta}, \tag{4.7f}$$

where a reduced mixture density is defined as $\hat{\rho} = \sum_\alpha \bar{\rho}_\alpha\sigma_{\alpha\alpha}^3$, where $\bar{\rho}_\alpha$ is the usual local average density of species α. The reduced mass is defined as $m_{12} = m_1m_2/(m_1+m_2)$, and is used to calculate the low density kinetic theory limit (D_0) of the interspecies diffusion [39]. Further corrections to the low density estimate of diffusion are incorporated using the hard sphere radial distribution function at the contact $g(\bar{\rho})$ [96], and finite density polynomial correction using $R(\hat{\rho},\ \hat{T})$ [140]. At this stage, all confinement effects along the confined direction are accounted for. Next we would discuss the streaming direction slip effects.

4.1.2 Surface friction: boundary conditions

In this section, we discuss the method to compute the species-specific friction coefficients ζ_1 and ζ_2. Similar to the single component case, the species interfacial friction is additive [71, 17]. Therefore, we first compute the friction coefficient of a single particle j of species α using the expression

$$\zeta_0^j = \frac{\int_0^\infty \langle f_{x,j}^{\mathrm{wf}}(0) f_{x,j}^{\mathrm{wf}}(t)\rangle \mathrm{d}t}{k_{\mathrm{B}}T + \int_0^\infty \langle v_{x,j}(0) f_{x,j}^{\mathrm{wf}}(t)\rangle \mathrm{d}t};\ j \in \alpha, \tag{4.8}$$

where ζ_0^j is the friction coefficient of the particle, $f_{x,j}^{\mathrm{wf}}$ and $v_{x,j}$ are the instantaneous streaming direction wall-fluid force and velocity of the particle near the solid wall. The angular brackets $\langle \cdots \rangle$ denote the ensemble average. The time correlation appearing in the numerator is the well known single-particle wall-fluid force autocorrelation function (FACF), while the denominator consists of wall-fluid force–velocity cross-correlation function (FVCCF). The total value of the macroscopic friction coefficient is obtained by adding contributions from all interfacial particles as $\zeta_\alpha = \sum_{j\in\alpha} \zeta_0^j$. This value of the macroscopic friction coefficient is used in the FBC described by Eq. (4.2), which closes the transport model.

Similar to our previous work [17], we generate the trajectory of the representative particle j using the GLE. The coarse-grained phenomenological dynamical framework of GLE allows one to evolve the dynamics of the single particle sandwiched between the atomically rough surfaces by taking the streaming and confined direction force fields into account. The dissipative and thermal motion of the particle is accounted by incorporating a non-Markovian friction force and its corresponding random force. The equations of motion can be written as

$$m_\alpha \frac{\mathrm{d}v_{z,j}(t)}{\mathrm{d}t} = -m_\alpha \int_0^t K_\alpha(t-t')v_{z,j}(t')\mathrm{d}t' + f_{z,j}^{\mathrm{tot}}(z_j(t)) + R_{z,j}(t), \tag{4.9a}$$

$$m_\alpha \frac{\mathrm{d}v_{x,j}(t)}{\mathrm{d}t} = -m_\alpha \int_0^t K_\alpha(t-t')v_{x,j}(t')\mathrm{d}t' + f_{x,j}^{\mathrm{tot}}(x_j(t), z_j(t)) + R_{x,j}(t), \tag{4.9b}$$

$$\frac{\mathrm{d}z_j(t)}{\mathrm{d}t} = v_{z,j}(t), \quad \frac{\mathrm{d}x_j(t)}{\mathrm{d}t} = v_{x,j}(t), \tag{4.9c}$$

where m_α is the mass of the particle j representing species α, while $v_{z,j}$ and $v_{x,j}$ are the velocities of the particle in the confined and streaming direction, respectively. The random forces $R_{z,j}(t)$ and $R_{x,j}(t)$ in the corresponding directions have zero mean, and are only auto-correlated by virtue of the fluctuation-dissipation theorem as $\langle R_{x,j}(0)R_{z,j}(t)\rangle = m_\alpha k_{\mathrm{B}}TK_\alpha(t)\delta_{xz}$, with δ_{xz} being the Kronecker delta. The corresponding structure based instantaneous force values on particle, i.e., $f_{z,j}^{\mathrm{tot}}$ and $f_{x,j}^{\mathrm{tot}}$, are sampled using the static mean force maps $F_z^{\mathrm{tot}}(z)$ and $F_x^{\mathrm{tot}}(x,z)$, that can be analytically calculated as explained in Ref. [17]. The presented equations are quite similar to that of the single species case, with one exception being the memory function $K_\alpha(t)$ in Eqs. (4.9a) and (4.9b) does not correspond to the pure component. Instead, it describes the noise characteristics of species α for its thermodynamic state in the mixture. The non-Markovian dissipative effects from other species are implicitly accounted in this representation. More explicit representations of memory function are discussed for colloidal mixtures by Chávez-Rojo et al. [40], where it is expressed in terms of the partial intermediate scattering functions involving the inter and intra-species contributions; but are not attractive due to their complexity and approximate nature.

To calculate the species specific memory function in the mixture, we use the corresponding memory function equation (MFE) [144], that can be written as

$$\frac{\mathrm{d}\psi_j(t)}{\mathrm{d}t} = -\int_0^t K_\alpha(t-t')\psi_j(t')\mathrm{d}t', \tag{4.10a}$$

$$\psi_j(t) = \frac{\langle \boldsymbol{v}_j(t)\cdot\boldsymbol{v}_j(0)\rangle}{\langle \boldsymbol{v}_j(0)\cdot\boldsymbol{v}_j(0)\rangle}; j\in\alpha, \tag{4.10b}$$

where $\psi_j(t)$ is the input velocity autocorrelation function (VACF) of species α from a bulk EMD simulation of the corresponding homogeneous mixture. Note that a vector value of particle velocity $\boldsymbol{v}_j(t)$ is used because noise is isotropic in the homogeneous mixture. Also, being a bulk homogeneous case, the FVCCF term does not appear in Eq. (4.10a). The numerical method to solve Volterra type integro-differential equation (Eq. (4.10a)) is discussed in Ref. [12]. Further discussion on the memory function at different molar compositions of the mixture, along with comments on the accuracy of the corresponding confined GLE simulations versus EMD is provided in Sec. 4.3.

4.2 Simulation Details

Different types of MD simulations are performed in the present work using the LAMMPS package [123]. All molecules are modeled as single site LJ particles, with their interactions described using the LJ 12–6 potential force fields. The majority of the examples in the present work comprise of methane and hydrogen mixtures at variable molar fractions. To test the robustness of the continuum method, additional calculations are performed for methane and argon mixture at a fixed molar fraction. For methane-hydrogen mixtures, an integration time step of 0.5 fs is used, while for methane-argon mixture, a time step of 1 fs is used in MD simulations. The cut-off parameter for all simulations is 1.5 nm, and the interaction parameters are listed in Table 4.1. All cross parameters are obtained using the LB combination rule. All EMD simulations are performed for 12 ns, where the first 2 ns data is discarded to allow system equilibration, and the trajectory data is saved at every 20 fs. We use the convention "X–Y α-β" to identify the bulk state molar composition. For example, a 30–70 methane-hydrogen mixture would mean a binary mixture consisting of 30% methane by molar fraction.

We first perform a series of EMD simulations of methane-hydrogen mixture in bulk homogeneous environment using a isothermal-isobaric (NPT) ensemble at variable molar fractions. The temperature is set to 300 K using a Nosé–Hoover thermostat [110] with a time constant of 0.2 ps, and the pressure to 1580 bar using a Parrinello-Rahman barostat [119]. The values of chosen temperature and pressure correspond to a

supercritical thermodynamic state of the mixture. The total number of particles in each molar composition is kept constant at 1660; only to be redistributed to fix the molar fraction of the species. The volume is allowed to fluctuate to fix the species densities. We perform 5 statistically identical NPT runs for every molar fraction case. The fluctuations in the box volume in these statistically identical NPT runs are averaged to compute the species bulk densities at a given molar fraction. The resulting species and mixture bulk densities for methane-hydrogen cases are plotted in Fig. 4.1, where it can be seen that the density of the mixture decreases with increasing molar fraction of methane at constant pressure. Further, a NVT run using the averaged box dimensions from NPT calculations is performed for each molar fraction, where the output pressure value is confirmed equal to the target value. These simulations are used for computing and verifying bulk dynamical properties, e.g. VACF to obtain the species memory function $K_\alpha(t)$ using Eq. (4.10). The procedure is identical for 70–30 methane-argon mixture at 3680 bar and 300 K.

Next, confined EMD runs of the mixture sandwiched between two rigid graphene surfaces (channel width 6.34 nm) are performed keeping the lateral pressure equal to the target pressure. Channel width is defined as the center to center distance between the first layer of wall atoms, and is used to calculate the average channel density ρ_{avg}. The other channel widths considered in this work are 3.21 nm, 2.25 nm, and 1.28 nm to test the model accuracy for various length scales, and are only simulated for 30–70 methane-hydrogen mixture. For smaller channel widths, the number of species particles are estimated using the linear superposition approximation that ensures the confined fluid pressure is constant under variable channel width [150, 43]. The simulation trajectory is divided into 1000 samples of 10 ps, which under ergodic hypothesis serve as ensembles to compute the necessary correlations for friction coefficient.

For confined NEMD simulations, we apply different magnitudes of gravity to test and demonstrate the applicability of the continuum formulation under the linear response regime, where the velocity profile scales linearly with the applied gravity, and the slip length is independent of the applied gravity [161]. The thermostat controlling the temperature is only applied to non-streaming directions to prevent any artifacts in the simulation, i.e., bias in the velocity profiles. To perform the ensemble average, 10 identical simulations are performed, differing only in their initial velocity distribution. Each ensemble is simulated for 30 ns, with the first 10 ns discarded to obtain the fully developed, steady-state velocity profiles.

In the transport model, the slip plane location (δ) is defined to be the larger of the distances δ_1 and δ_2, which correspond to the respective positions where the fluid layers of the two species start to develop. They (δ_1 and δ_2) are estimated using the tolerance on the species densities as 10^{-3} molecules/nm^3. For methane-hydrogen system, this value is approximately 0.24 nm for all molar fraction cases, while for 70–30 methane-argon system, it is 0.3 nm. Its precise location is dependent upon the thermodynamic state and

the force-fields used in the MD simulation. To compute the species interfacial friction, 2D GLE simulations are performed with a time step of 0.01 ps, with the production trajectory of 400 ps, with data saved at every other step (0.02 ps). The numerical method for time integration of the GLE is discussed in Ref. [144]. First 100 ps of the simulation trajectory was discarded to allow the equilibration of the species GLE particle. Approximately 2×10^4 instances of particle trajectories were generated to compute the relevant time correlations in Eq. (4.8).

To compare the time estimates, we compared the Central Processing Unit (CPU) time, which is wall-clock time multiplied by the number of parallel processors in a simulation. A single process GLE simulation for 100 ps equilibration and 400 ps production run takes about 120 seconds in CPU time. In comparison, a typical EMD simulation is orders of magnitude slower (approximately 540 CPU hours to simulate a 12 ns run for largest system size). Also, GLE can be run on a personal workstation as it uses a single CPU process, and it does not scale with particle number, as compared to EMD/NEMD simulation, which require massive parallelization to curtail the wall-time. The continuum formulation for a binary mixture typically takes 300 seconds as compared to NEMD, where meaningful data for velocity profiles requires 33230 CPU hours of production runs. Therefore, our GLE/continuum framework provides a massive speedup over NEMD to obtain the velocity profiles.

4.3 Results

In this section, we test the accuracy of the continuum framework by comparing the predicted velocity profiles against the ones provided by the NEMD simulations. Using the species density profiles ρ_α, presented in Fig. 4.2(a) for 30–70 methane-hydrogen mixture in 6.34 nm wide slit channel, we first calculate the local average density $\bar{\rho}_\alpha$ of the species using Eq. (4.4) and plot them in Fig. 4.2(b). It can be observed that (a) hydrogen being smaller in size than methane, has density peak closer to the wall, and (b) the coarse grained local average density is a homogenized version of local density and contains non-local effects due to the spatial averaging of the latter. The local average density of the mixture is then obtained as the sum of local average density of the species and is used to compute the shear viscosity of mixture as a pseudo LJ fluid using Eqs. (4.5) and (4.6) as shown in Fig. 4.2(c). This is further divided by the local mass fraction $\omega_\alpha(z)$ of the species to obtain the species partial viscosities. Although the number density of the hydrogen is higher than that of methane in the center of the slit channel, the partial viscosity of methane is higher as it is approximately 8 times heavier than hydrogen. We then calculate interspecies diffusion coefficient D_{12} using Eq. (4.7) and plot it in Fig. 4.2(d). We also compared the value of D_{12} obtained in the center of the channel

with one obtained from the corresponding bulk homogeneous EMD simulation using the method outlined by Heyes in Ref. [67] and found good agreement with the values predicted by empirical correlations [139].

Next, we compare the effectiveness of the GLE framework to provide species friction coefficient, by comparing the time correlations appearing in Eq. (4.8) with EMD calculations. As explained previously [17], we only consider a small interfacial region (about 0.4 nm from the wall) contribution towards the interfacial friction, in conjunction with initial time occupancy based tagging method [122, 144]. This is necessary to exclude the viscous effects from the friction computations [64, 71]. In order to obtain the memory function, we use the MFE in Eq. (4.10), with bulk EMD simulation VACF. We plot the resultant memory function of methane (Fig. 4.3(a)) and hydrogen (Fig. 4.3(b)) for a homogeneous mixture at 1580 bar and 300 K for different molar fractions. As a consistency check, we performed bulk GLE simulations (in the absence of structure based mean forces) of methane and hydrogen to reproduce the input VACF from EMD. It can be understood from the plots that the noise relaxation (memory of dissipation) of hydrogen is faster than that of methane, and change in molar fraction does not alter the noise relaxation time significantly. However, the variance of the thermal force, which is proportional to $K(0)$ as understood by the fluctuation-dissipation theorem, increases with increase in molar fraction of methane, with reversing trends for increase in hydrogen composition. Therefore, one can conclude that methane rich mixtures are more dissipative in nature as compared to hydrogen rich mixtures. We show the comparison of the species FACF calculated from EMD and GLE formulations for 30–70 methane-hydrogen mixture in Figs. 4.4(a) and 4.4(b). We observe that there is a good agreement between the two approaches, again validating our choice of using the implicit memory function to compute the transport properties. The contribution of FVCCF to friction coefficient on graphene surface was found to be negligible, in accordance with our previous observations of water on graphene surface [17].

We now compare the species velocity profiles predicted by the continuum/GLE framework with the ones obtained from NEMD simulations. Figures 4.5(a) and 4.5(b) depict the comparison for methane and hydrogen velocities respectively for 30–70 methane-hydrogen mixture for different gravity values and channel widths, where a good agreement is observed between the two methods. Similar accuracy is obtained for all molar compositions of the mixture, including the limiting cases comprising of only one species. The momentum equation (Eq. (4.1)) in the limiting case appropriately reduces to that of one component fluid transport because in the limit $\rho_\beta \to 0$, the interspecies friction term vanishes and $\mu_\alpha^{\mathrm{P}} \to \mu_{\mathrm{f}}$. Also, the pseudo fluid viscosity in Eq. (4.6) obtained from vdW1 approximation (Eq. (4.5)) reduces to pure component viscosity, thereby providing an internal consistency of this formulation for limiting cases. We also tested the framework for 70–30 methane-argon mixture confined in graphene and observed similar fidelity for velocity

profiles as depicted in Figs. 4.6(a) and 4.6(b) for methane and argon. By construction, the model includes both viscous and slip effects that are superimposed. The relatively dominant contribution of slip in graphene nanochannels results in plug type of velocity profiles instead of the parabolic type. A systematic analysis of high to low degree of slip with different wall types has been presented before [13, 17], which demonstrate the transition from slip to no-slip type of velocity profiles.

In order to check the accuracy of the framework with differing value of gravity for the two species, we compared the results with $g_1 = 1 \times 10^{-4}$ nm/ps^2, and $g_2 = 2 \times 10^{-4}$ nm/ps^2, for 30–70 methane-hydrogen mixture in a 6.34 nm wide graphene slit as shown in Figs. 4.7(a) and 4.7(b). Even under the action of different force per unit mass, the faster species drags the slower species with itself, giving rise to very similar velocity profiles that are corroborated from NEMD and theoretical framework.

Next, we discuss the mixture barycentric velocities. In principle, they can be obtained by taking the mass weighted average of species velocity profiles, but an approximate single fluid representation can also be provided. We start with adding the momentum equation of two species to obtain

$$\frac{\mathrm{d}}{\mathrm{d}z}\left[\mu_1^{\mathrm{P}}\frac{\mathrm{d}u_1}{\mathrm{d}z} + \mu_2^{\mathrm{P}}\frac{\mathrm{d}u_2}{\mathrm{d}z}\right] + m_1\rho_1 g_1 + m_2\rho_2 g_2 = 0, \tag{4.11}$$

where the last two terms represent the total body force on the mixture, and the term inside the square brackets is the sum of the shear stresses of the species that can be approximated by the mixture shear stress as $\mu_{\mathrm{f}}\ \mathrm{d}u_{\mathrm{f}}/\mathrm{d}z$. Then, the resulting formulation transforms to an equivalent one component transport problem involving pseudo fluid, and can be solved with FBC $A\mu_{\mathrm{f}}\ \mathrm{d}u_{\mathrm{f}}/\mathrm{d}z = \zeta_{\mathrm{f}}u_{\mathrm{f}}$ at the slip plane. The effective friction for the mixture ζ_{f} can be apportioned as the sum of species friction as $\zeta_{\mathrm{f}} = \zeta_1 + \zeta_2$, by utilizing its additive nature. As an alternative to the FBC to solve Eq. (4.11), one can also use the Dirichlet type boundary condition discussed in our previous work for single component transport [17]. We carried out the calculations for the mixture barycentric velocity profile and observed good agreement with the NEMD computed mixture velocity. Next, we computed the value of mixture friction coefficient at different molar concentrations for methane-hydrogen mixture, and observed a linear variation as shown in Fig. 4.8. Therefore, once the pure component friction coefficients of the species are known at a fixed temperature and pressure, the molarity dependent mixture friction coefficient can be predicted by utilizing the linear relationship, without necessitating additional GLE or EMD computations.

Last, we calculate the species slip length $l_{\alpha\mathrm{s}}$ using the continuum velocity profiles from the expression

$$l_{\alpha\mathrm{s}}\frac{\mathrm{d}u_\alpha(z)}{\mathrm{d}z}\bigg|_{z=-L/2+\delta} = u_{\alpha\mathrm{s}}, \tag{4.12}$$

and observed that the species slip length remains unchanged for different channel widths with the same mixture composition (with reference cases being 30–70 methane-hydrogen and 70–30 methane-argon). However, it varies with the mixture composition, and is not same for the two species (see Table 4.2), despite seemingly similar velocity profiles. To understand this, we write the expression for the ratio of the slip lengths

$$\frac{l_{1\mathrm{s}}}{l_{2\mathrm{s}}} = \frac{\zeta_2}{\zeta_1}\frac{\mu_1^{\mathrm{P}}(z)}{\mu_2^{\mathrm{P}}(z)}\bigg|_{z=-L/2+\delta} = \frac{\zeta_2}{\zeta_1}\frac{\omega_1(z)}{\omega_2(z)}\bigg|_{z=-L/2+\delta}, \tag{4.13}$$

where we utilize the aforementioned relationship of partial viscosities to pseudo fluid viscosity as $\mu_\alpha^{\mathrm{P}} = \omega_\alpha \mu_{\mathrm{f}}$. It is clear that the equal slip lengths would require the ratio ζ_1/ζ_2 equal to ω_1/ω_2, which is not strictly satisfied.

In this chapter, we have developed a continuum based hydrodynamic transport model for isothermal, non reacting mixture transport in slit shaped nanochannels. We have focused on species transport equation instead of mixture motion as a whole. Viscous contributions are incorporated using partial viscosities, which are evaluated using vdW1 and LADM formulation. A Maxwell-Stefan type term is included to characterize the interspecies friction. The boundary conditions are provided in the form of a friction based condition that contains the species-specific interfacial friction coefficient. The friction coefficient is computed using a refined GLE based dynamical framework for mixtures. The species-specific memory function for the GLE is obtained implicitly by utilizing the corresponding MFE of the single particle VACF. The resulting correlations show good agreement with their EMD counterparts. Under application of gravity, the species velocity profiles are predicted that are in excellent agreement with NEMD velocities. The accuracy of the model remains unchanged in cases of species driven by different gravity fields. In the cases considered, the mixture was observed to behave as a pseudo fluid, that can be solved with preexisting one component transport models. Furthermore, it is also revealed from the calculations that the effective friction coefficient of the mixture varies linearly with molar composition at constant pressure and temperature, and therefore can be directly predicted from the pure component friction coefficients. The slip lengths of the species are observed to be different from each other.

Table 4.1: LJ parameters of different species used to study mixture transport.

Type	σ (nm)	ϵ/k_B (K)	mass (g/mol)
Carbon (C)	0.3400	28.0	12.0107
Methane (CH_4)	0.3810	148.1	16.0429
Hydrogen (H_2)	0.2915	38.0	2.0160
Argon (Ar)	0.3410	119.8	39.9480

Table 4.2: Slip lengths (nm) of species on graphene interfaces for select methane-hydrogen mixtures.

Molar Fraction	Methane	Hydrogen
0-100	—	6.6354
30-70	13.8585	3.5225
50-50	12.7025	2.7957
70-30	11.9140	2.0656
100-0	10.5062	—

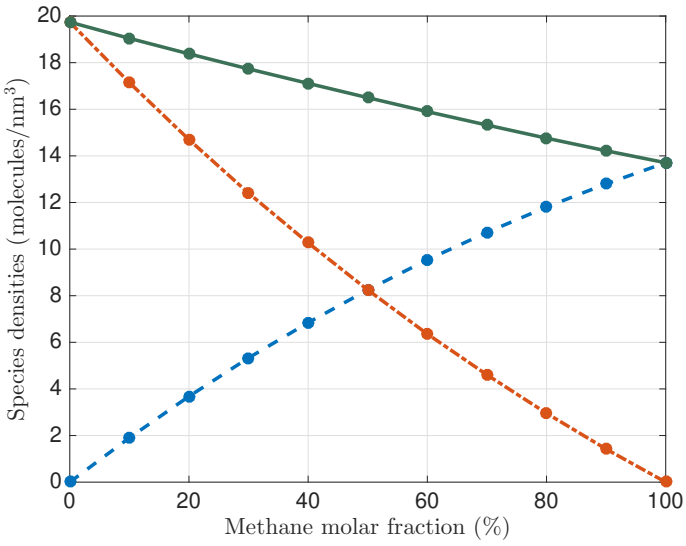

Figure 4.1: Mixture (green line, solid) and species bulk density at 1580 bar pressure and 300 K temperature for different molar compositions of a methane-hydrogen mixture. Methane is represented by blue dashed line, while hydrogen is orange dash dot line. Results are averaged over 5 NPT ensembles and errorbars are smaller than the size of the symbols.

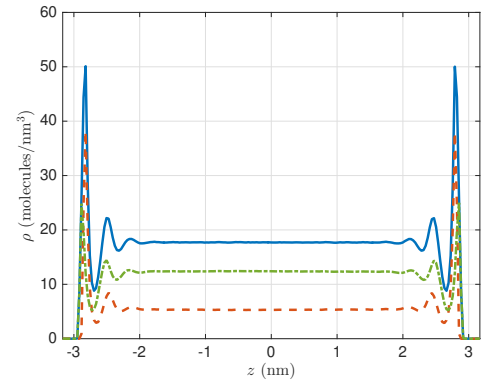

(a) Local density

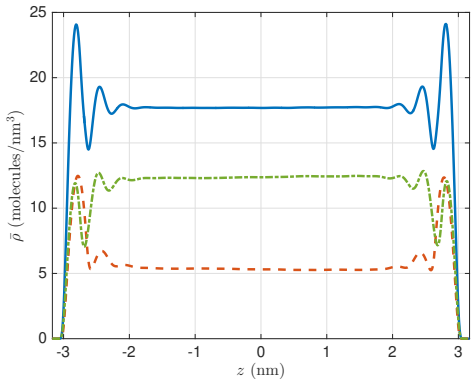

(b) Local average density

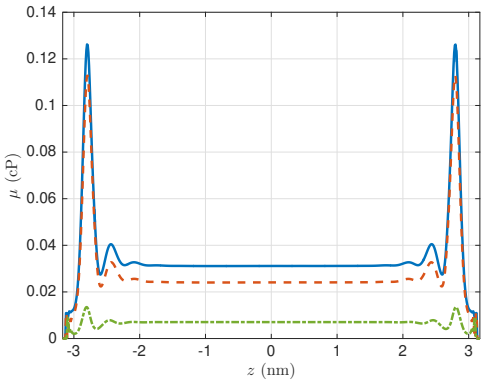

(c) Viscosity

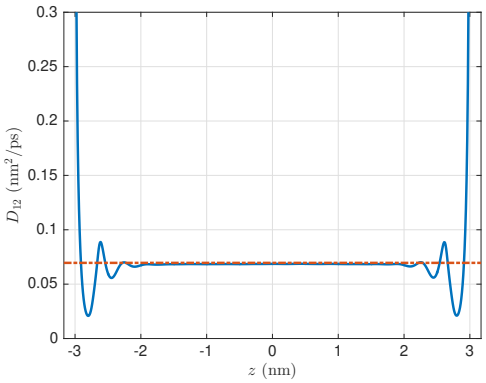

(d) Interspecies diffusion

Figure 4.2: Variation of (a) local density, (b) local average density, (c) shear viscosity, and (d) interspecies diffusion for 30–70 methane-hydrogen mixture in a 6.34 nm wide graphene slit. Mixture is represented by solid blue line, while methane is orange dash line and hydrogen is green dash dot line. The dotted red line in (d) is from bulk homogeneous EMD calculations outlined in Ref [67].

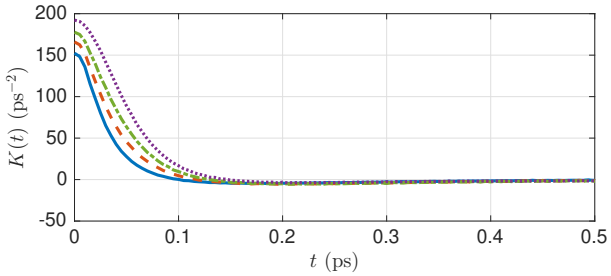

(a) Methane

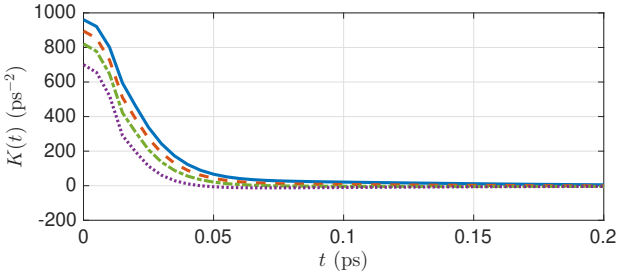

(b) Hydrogen

Figure 4.3: Memory function at 300 K and 1580 bar of (a) methane in 30–70 (blue line, solid), 50–50 (red line, dash), 70–30 (green, dash-dot), and 100–0 (purple, dot), and (b) hydrogen in 70–30 (blue line, solid), 50–50 (red line, dash), 30–70 (green, dash-dot), and 0–100 (purple, dot) methane-hydrogen mixture.

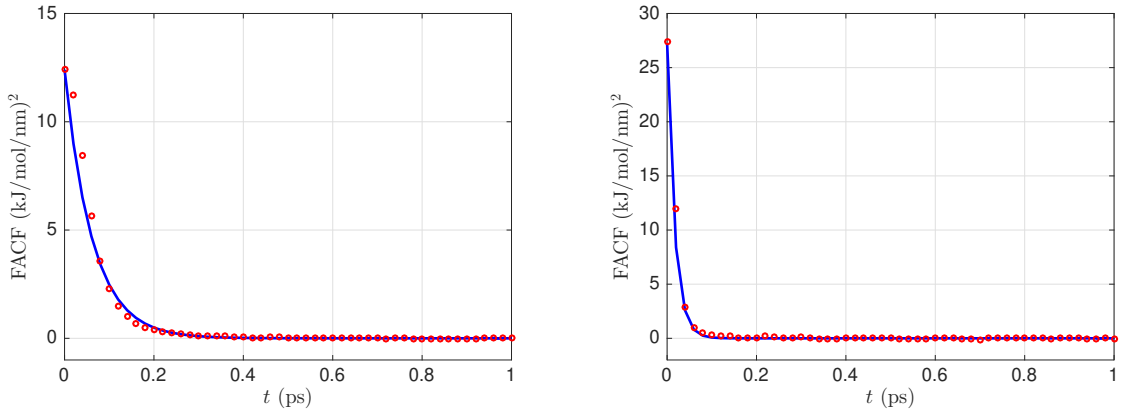

(a) Methane

(b) Hydrogen

Figure 4.4: Wall-fluid FACF from GLE (bold line, blue) and EMD (circles, red) for (a) methane, and (b) hydrogen in 30% methane rich mixture composition.

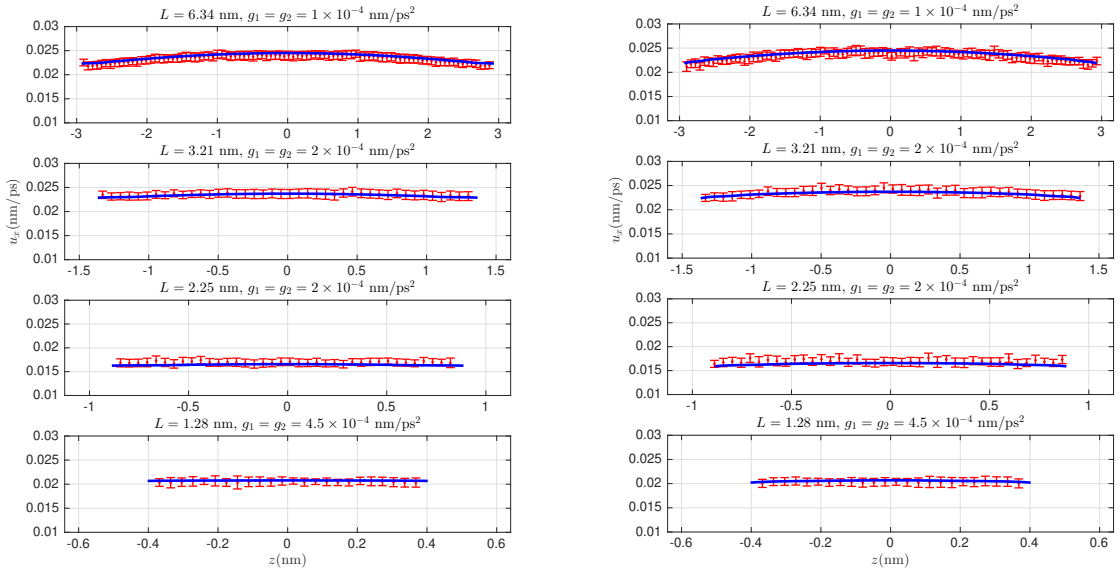

(a) Methane

(b) Hydrogen

Figure 4.5: Methane, and (b) Hydrogen velocity profiles for 30-70 methane-hydrogen mixture. Continuum results are in solid line (blue), while MD results are represented by error bars (red).

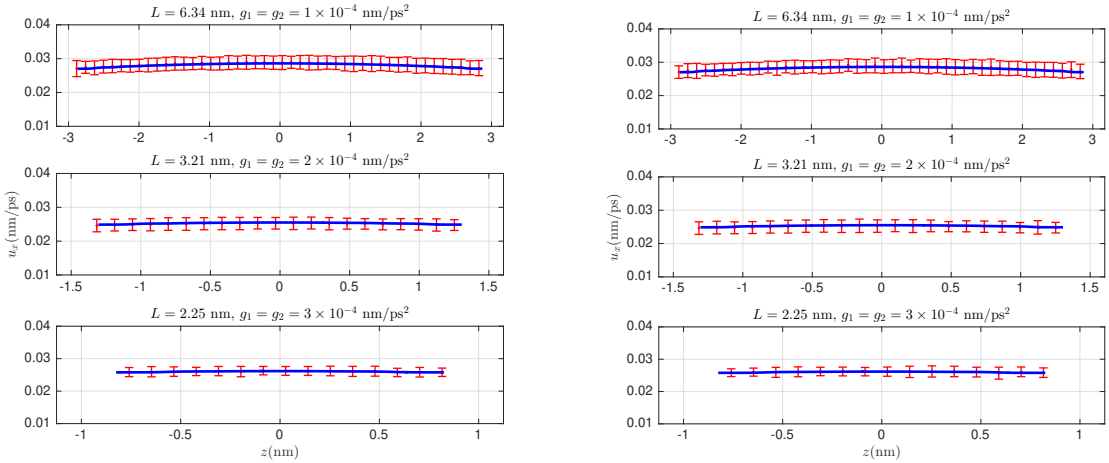

(a) Methane

(b) Argon

Figure 4.6: Methane, and (b) Argon velocity profiles for 70-30 methane-argon mixture. Continuum results are in solid line (blue), while MD results are represented by error bars (red).

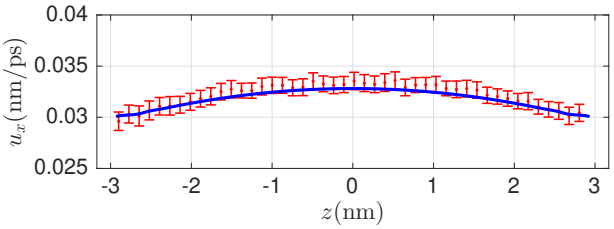

(a) Methane with $g_1 = 1 \times 10^{-4}$ nm/ps^2

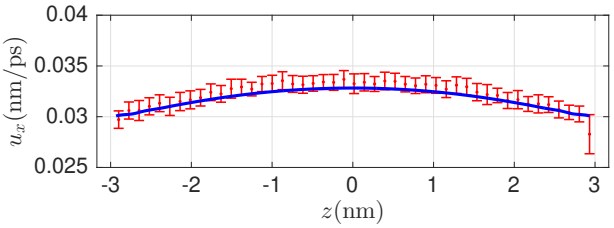

(b) Hydrogen with $g_2 = 2 \times 10^{-4}$ nm/ps^2

Figure 4.7: Methane and Hydrogen velocity profiles of 30-70 methane-hydrogen mixture with methane gravity $g_1 = 1 \times 10^{-4}$ nm/ps^2 and hydrogen gravity $g_2 = 2 \times 10^{-4}$ nm/ps^2. Continuum results are in solid line (blue), while MD results are represented by error bars (red).

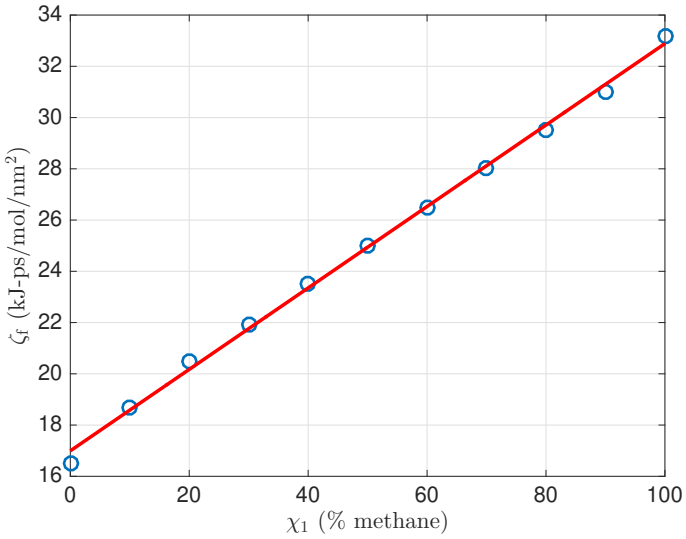

Figure 4.8: Friction factor of mixture dependence on methane molar concentration in methane-hydrogen mixtures at 1580 bar and 300 K. GLE computed data points are displayed in blue open circles, while the red line is the linear least squares fit.

Chapter 5

Nanochannel electroosmotic flow: effects of discrete ion, enhanced viscosity and surface friction

When ions are dissolved in a solvent confined between charged solid surfaces, an electric double layer (EDL) is formed that consists of spatially varying charge in the liquid-solid interface. Under the application of an external electric field tangential to the confined direction, the ions experience a driving force. The resultant migration of ions drags the solvent along, resulting in electroosmotic flow (EOF). The EOF has received significant attention, especially at micro- and nano-scale systems, primarily due to its ease of manipulation and control that make it usable in a multitude of areas, including but not limited to biological flows in transmembrane protein channels such as α-hemolysin [111], proton exchange membrane based fuel cells [35], and micro- and nano-fluidic field effect rectification [147, 83].

In "extreme" cases when the surface charge density of the solid wall exceeds a critical value [95], the co-ion density becomes higher than that of counter-ion in a certain region of EDL resulting in a phenomenon known as "charge-inversion" [133]. The charge inversion in mainly manifested due to the discrete nature of ions and solvent. Simultaneously, the counter-ion may also undergo contact adsorption at the liquid-solid interface and render itself unable to transfer momentum to the solvent [133, 176, 175]. Further away from the surface, where the surface charge effects are minimal, the co-ion is mobile and has a higher number density due to charge inversion. A combination of this physics drags the solvent in the opposite direction than the one predicted by the classical electroosmotic transport theory, resulting in EOF reversal phenomenon.

Recently, Yoshida et al. [176, 175] have applied the Onsager's generalized irreversible thermodynamics framework to nanochannel electrokinetic flows. In their work, relevant fluxes (i.e. species mass flow, electric current etc.) are described equal to the linear combination of the corresponding forces (gravity, electric field etc.) by a force-flux relationship. The prefactor of this force-flux relationship are the transport coefficients that obey Onsager reciprocal relation [113, 114]. These transport coefficients, in turn, can be evaluated using the Green-Kubo framework in conjunction with Equilibrium Molecular Dynamics (EMD). The framework is successful in predicting flow reversal, by virtue of negative electroosmotic collective transport coefficients. However, it is unable to describe the EOF velocity profiles as the treatment of the problem is not local.

The classical treatment of EOF uses the Gouy-Chapman (GC) theory for predicting the charge concen-

tration profile, which in turn provides the measure of the electrical driving force in the Navier-Stokes (NS) equations. The GC theory, being a mean field approach that does not take into account the discrete nature of ions and assumes a constant dielectric permittivity of the solvent, predicts a charge distribution that is exponential in nature. Because of these limitations, the GC model cannot describe the charge-inversion effect even in a qualitative manner, and consequently, is inaccurate in predicting flow reversal [133]. Therefore, correct charge distribution that incorporates electrochemical potential of mean force (PMF) on the ions [102], along with appropriate space dependent solvent polarization [54] is necessary for EOF predictions.

In addition to the inhomogeneous charge concentration, a correct viscosity variation is central to the success of the EOF model. It has been previously demonstrated that the solvent interfacial viscosity is enhanced in the presence of ions and charged surface [65, 92, 135]. Several mechanisms of viscosity enhancement have been identified, including increased hydrogen bonding [134] and reduced mobility of the ions in the interfacial region due to contact-adsorption at the wall [172]. Finally, the assumption of no-slip condition also leads to serious quantitative errors in the predicted EOF velocity profile. At the nanoscale, the fluid layer next to the wall acquires a relative "slip" velocity with respect to the wall. Near charged surfaces, quantities such as solvent interfacial friction and slip length are affected due to combined electro-hydrodynamic effects [78, 15].

In this chapter, we propose an isothermal, one-dimensional, electroosmotic flow model for slit-shaped nanochannels. Nanoscale confinement effects are embedded into the transport model by incorporating the spatially varying solvent and ion concentration profiles that correspond to the electrochemical potential of mean force. Local viscosity is dependent on the solvent local density and is modeled using the local average density method. The excess component of the local solvent viscosity is modeled by the local application of Onsager and Fouss theory, and Hubbard-Onsager electro-hydrodynamic equation based dielectric friction theory. A Dirichlet-type boundary condition is provided in the form of the slip velocity that is dependent on the macroscopic interfacial friction. This solvent-surface specific interfacial friction is estimated using a dynamical generalized Langevin equation based framework. The electroosmotic flow of Na^+ and Cl^- as single counterions and NaCl salt solvated in SPC/E water confined between graphene and silicon slit-shaped nanochannels are considered as examples. The proposed model yields good quantitative agreement with the solvent velocity profiles obtained from the non-equilibrium molecular dynamics simulations, including the cases of anomalous transport such as EOF reversal.

5.1 Electroosmotic Flow model

The relevant 1D formulation for an isothermal, low Reynolds number, electroosmotic flow in a slit channel can be written as a Stokes equation [134, 135]

$$\frac{\mathrm{d}}{\mathrm{d}z}\left[\mu(z)\frac{\mathrm{d}u_{\mathrm{eo}}}{\mathrm{d}z}\right]+\sum_{i\,\in\,\pm}\rho_i(z)\tilde{z}_i e E_x^{\mathrm{ext}}=0, \tag{5.1}$$

with boundary conditions

$$u_{\mathrm{eo}}\left(-\frac{L}{2}+\delta\right)=u_{\mathrm{eo}}\left(+\frac{L}{2}-\delta\right)=u_{\mathrm{s}}, \tag{5.2}$$

where L is the channel width, with confining walls located at $\pm L/2$, and (x, z) are the streaming and confined directions, respectively. $u_{\mathrm{eo}}(z)$ is the EOF velocity field in the streaming direction, e is the electronic charge, E_x^{ext} is the applied electric field in the direction parallel to the wall, $\rho_i(z)$ is the ion concentration field, and $\tilde{z}_i$ is the valency of the ion i, which may be a cation $(+)$ or anion $(-)$. The summation runs over all ionic species $(i\ \in\ \pm)$ to compute the total electroosmotic driving force. Spatial variation of the solvent viscosity $\mu(z)$ is considered to reflect its dependence on inhomogeneous properties along the confined direction such as solvent and ion densities, solvent permittivity and ion conductivity. Dirichlet type boundary conditions are provided at a distance δ from the wall, which is the first location where the solvent density (ρ_0) satisfies $\rho_0 > \rho_{0,\mathrm{tol}}$, with u_{s} as the electroosmotic slip velocity. The boundary conditions are expressed in FBC form as

$$A\mu(z)\frac{\mathrm{d}u_{\mathrm{eo}}(z)}{\mathrm{d}z}\bigg|_{z=-L/2+\delta}=\zeta_0 u_{\mathrm{s}}, \tag{5.3}$$

where A is the interfacial area and ζ_0 is a macroscopic parameter known as the interfacial friction coefficient of the solvent. In addition, a symmetry boundary condition at the center point of the channel can be written as

$$\frac{\mathrm{d}u_{\mathrm{eo}}(z)}{\mathrm{d}z}\bigg|_{z=0}=0. \tag{5.4}$$

As discussed previously [17], we can recast Eqs. (5.1), (5.3) and (5.4) to provide an expression for the electroosmotic slip velocity as

$$u_{\mathrm{s}}=\frac{AeE_x^{\mathrm{ext}}}{\zeta_0}\sum_{i\,\in\,\pm}\tilde{z}_i\int_{-L/2+\delta}^{0}\rho_i(z)\mathrm{d}z. \tag{5.5}$$

This value of the electroosmotic slip velocity is used as boundary condition in Eq. (5.2). Inputs required for this framework are the ion concentration, solvent viscosity, and the interfacial friction coefficient for the solvent. The methods to obtain these inputs are discussed below.

5.1.1 Ion concentration and solvent viscosity variation

In this section, we discuss methodologies to capture inhomogeneities of the fluid properties in the confined direction. Due to the presence of charged confining walls, the electrochemical PMF of ions and the polar solvent (SPC/E water in our case) shows oscillations normal to the wall. Consequently, the density profiles exhibit significant layering in the confined direction. Variations in the ion/solvent densities can be quantified using MD simulations with appropriate spatial binning. Alternatively, one can utilize continuum based theories such as EQT [137, 141, 142, 99, 100, 101, 106, 102], which a multiscale formulation to compute density and the corresponding PMF profiles in the nanochannel. The advantages of using EQT over particle-based methods are significant in terms of computing speed since it is orders of magnitude faster. Recently, the approach has also been used to calculate various thermodynamic properties in confined systems, e.g., lateral and confined direction pressure, surface tension, solvation force, and adsorption isotherms [101]. The EQT framework has also been extended to study multicomponent systems such as a binary Lennard-Jones (LJ) mixture [106], and ion/solvent systems with charged walls [102]. Since our objective in this work is to calculate the EOF velocity profiles, we have used the density and PMF profiles obtained from EMD simulations.

Due to the inhomogeneities of the solvent density and the presence of mobile ions and charged walls, solvent viscosity is not a constant value, instead it varies along the confinement. The total viscosity variation due to both of these effects can be apportioned separately as

$$\mu(z) = \mu_{\mathrm{p}}(z) + \mu_{\mathrm{ex}}(z), \tag{5.6}$$

where $\mu_{\mathrm{p}}(z)$ is the pure-component viscosity profile, and it only models the effects of solvent density variation on the total viscosity, while $\mu_{\mathrm{ex}}(z)$ is the variation of the excess part of the viscosity due to the presence of charges (ions and charged walls). We use the LADM [27, 28, 167] to predict the pure-component viscosity profile. Here, the 1D solvent density profile $\rho_0(z)$ is first weight-averaged to obtain a coarse-grained density profile as

$$\bar{\rho}_0(z) = \frac{6}{\sigma_0^3} \int\limits_{|z-z'|<\sigma_0/2} \left[\left(\frac{\sigma_0}{2}\right)^2 - (z-z')^2 \right] \rho_0(z')\, \mathrm{d}z', \tag{5.7}$$

where the average is performed over the length scale of solvent LJ diameter σ_0. The coarse grained solvent density $\bar{\rho}_0$ along with temperature T provides an equivalent homogeneous, pure-component thermodynamic state of the solvent, which can then be utilized to compute the local pure-component viscosity $\mu_{\mathrm{p}}(z)$ using an appropriate equation of state [17].

The corresponding change in the excess viscosity $\mu_{\rm ex}(z)$ of the solvent is dependent on the concentration of the ions. The preliminary estimates of the excess term were provided by Falkenhagen [48] that are valid for symmetrical electrolytes, and later extended by Onsager and Fouss [115] to account for asymmetrical electrolytes. More rigorous, microscopic expressions for the excess viscosity have also been derived by Chandra and Bagchi [38], where they have used the mode coupling theory (MCT) to account for the realistic ion-ion transverse stress correlations. Their expression also reduces to that of Falkenhagen in the limit of low ionic concentration. However, their formulation involves the computation of additional parameters such as ionic structure factors and the frequency dependent van Hove functions. In this work, the excess contribution $\mu_{\rm ex}$ due to the layering of the charges can be expressed as

$$\mu_{\rm ex}(z) = \sum_{i \in \pm} \left[a \sqrt{\frac{2I(z)}{\varepsilon_{\rm r}(z)T}} \frac{\bar{\rho}_i(z) \left|\tilde{z}_i\right|^3}{2I(z)\lambda_i(z)} + \mu_{\rm p}(z) B_i(z) \bar{\rho}_i(z) + 1.6 \mu_{\rm p}(z) B_i^2(z) \bar{\rho}_i^2(z) \right]. \tag{5.8}$$

The first term on the right in Eq. (5.8) represents the Onsager and Fuoss expression for excess viscosity due to long range Coulombic interactions among ions in a dielectric medium, and the second term is due to solute-solvent interactions [120]. The last term appearing in Eq. (5.8) represents higher order solute-solute association effects, and cannot be interpreted unambiguously [45]. Therefore, we have considered it to be dependent on its preceding term as an ansatz proposed by Breslau and Miller [34]. The relative permittivity of solvent $\varepsilon_{\rm r}$, ion conductivities λ_i, and viscosity B-coefficient of ion i (B_i) are considered to be inhomogeneous in the confinement. The ionic strength is defined as $I = 0.5 \sum_i \bar{\rho}_i \tilde{z}_i^2$, where $\bar{\rho}_i$ is the local average ion concentration calculated using the LADM on ion concentration profile, and T is the operating temperature. The prefactor $a = Fe^2 10^8 \sqrt{N_{\rm A}}/480\pi\sqrt{10^3 \varepsilon_0 k_{\rm B}} = 0.3645$ provides viscosity in Pa-s when $\bar{\rho}$ is expressed in mol/L and λ in $\Omega^{-1}\text{mol}^{-1}\text{cm}^2$. Here, F is the Faraday's constant, ε_0 is the permittivity of vacuum, $k_{\rm B}$ is the Boltzmann constant, T is the operating temperature, and $N_{\rm A}$ is the Avogadro's constant.

5.1.2 Solvent permittivity: Polarization model

To capture the spatial variation of relative permittivity of solvent ($\varepsilon_{\rm r}$), we utilize the polarization model as [54, 55]

$$\varepsilon_{\rm r}(z) = 1 - \frac{P(z)}{\varepsilon_0 \phi'(z)}, \tag{5.9}$$

where ε_0 is the vacuum permittivity, $P(z)$ is the variation of solvent polarization, $\phi(z)$ is the electrostatic potential, and $\phi'(z) = {\rm d}\phi/{\rm d}z$. The solvent polarization is calculated as

$$P(z) = \rho_0(z) \mu_d \langle \cos\theta(z) \rangle, \tag{5.10}$$

where μ_d is the magnitude of the solvent dipole moment, and $\langle\cos\theta(z)\rangle$ is the mean cosine of the angle of the solvent dipole vector with the z-axis. Its variation in the confinement is calculated using the Langevin point dipole model as [54]

$$\langle\cos\theta(z)\rangle = -\mathcal{L}(\beta\mu_d\phi'(z)), \tag{5.11}$$

where $\mathcal{L} = (\coth(x) - 1/x)$ is the Langevin function, and $\beta = 1/k_{\mathrm{B}}T$. To calculate the electrostatic potential $\phi(z)$, we solve a 1D Poisson equation

$$\frac{\mathrm{d}}{\mathrm{d}z}\left(\varepsilon_{\mathrm{r}}(z)\frac{\mathrm{d}\phi}{\mathrm{d}z}\right) = -\frac{1}{\varepsilon_0}\sum_{i\,\in\,\pm}\rho_i(z)\tilde{z}_i e, \tag{5.12}$$

with boundary conditions

$$\left.\frac{\mathrm{d}\phi}{\mathrm{d}z}\right|_{z=\pm L/2} = \pm\frac{\sigma_{\mathrm{wall}}}{\varepsilon_0}, \tag{5.13a}$$

$$\phi(z=0) = 0, \tag{5.13b}$$

where σ_{wall} is the wall-charge density. Ion concentration values from the EMD simulation are used to solve the Poisson equation. Eqs. (5.9), (5.10), (5.11), and (5.12) are solved self consistently to obtain the variation of the relative permittivity $\varepsilon_{\mathrm{r}}(z)$, polarization $P(z)$, average dipole angle $\langle\cos\theta(z)\rangle$, and 1D electrostatic potential $\phi(z)$. Here, the value of the solvent dipole moment is calculated by taking the limit $\phi'(z) \to 0$ in Eq. (5.9) as

$$\varepsilon_{\mathrm{r,b}} = 1 + \frac{\rho_{0,\mathrm{b}}\mu_d^2\beta}{3\varepsilon_0}, \tag{5.14}$$

where $\varepsilon_{\mathrm{r,b}}$ is the bulk value of relative permittivity of the solvent (in the absence of an external electric field), and $\rho_{0,\mathrm{b}}$ is the bulk density of the solvent. Further details on the polarization model are presented in Refs. [54, 55, 102].

5.1.3 Ionic conductivity

The variation of ionic conductivity in the confinement is modeled using a modified Nernst-Einstein model as

$$\lambda_i = \left(\frac{F^2}{RT}\right) D_i^0 \gamma_i^{\alpha_i} \tag{5.15}$$

where $R = k_{\mathrm{B}}N_{\mathrm{A}}$ is the universal gas constant. The ion diffusivity in the solvent at infinite dilution limit D_i^0 is calculated by integrating the velocity autocorrelation of the ion in the solvent. The activity coefficient

γ_i is modeled with the extended Debye-Hückel model [171] as

$$\log_{10}\gamma_i = -\frac{\tilde{A}|\tilde{z}_i|^2\sqrt{I}}{1+\tilde{B}\mathring{a}|\tilde{z}_i|\sqrt{I}}, \tag{5.16a}$$

$$\mathring{a} = \sum_{i\in\pm}\frac{\bar{\rho}_i|\tilde{z}_i|^2\sigma_i}{2I}, \tag{5.16b}$$

$$\tilde{A} = \frac{1.8247\times10^6}{(\varepsilon_{\mathrm{r}}T)^{3/2}}\ \mathrm{M}^{-1/2}, \tag{5.16c}$$

$$\tilde{B} = \frac{502.901}{(\varepsilon_{\mathrm{r}}T)^{1/2}}\ \mathrm{M}^{-1/2}\ \mathrm{nm}^{-1}. \tag{5.16d}$$

It should be noted that in the infinite dilution limit, i.e. $\rho_\pm \to 0$, the activity coefficient $\gamma_i \to 1$ and Eq. (5.15) reduces to the Nernst-Einstein equation. For finite ion concentration, an ion-ion correlation based correction factor is introduced via the parameter α_i that is parameterized as [3]

$$\alpha_i = \begin{cases} 0.6/|\tilde{z}_i|^{0.5}, & \text{if } I < 0.36\ \mathrm{M} \\ \sqrt{I}/|\tilde{z}_i|, & \text{otherwise.} \end{cases} \tag{5.17}$$

5.1.4 Viscosity B-coefficient

The local B-coefficients are estimated using the local application of dielectric friction based model developed by Ibuki and Nakahara as [74]

$$B_i = y_i R_i^3 + \exp\left[2.631 + \sum_{k=1}^{4} a_k \left(\frac{R_i}{R_{\mathrm{HO}}}\right)^k\right], \tag{5.18}$$

where R_i is the hydrated ion radius estimated using ion-solvent radial distribution function, y_i is chosen as $10\pi/3$ for counter-ions to model contact-adsorption at the interface and $4\pi/3$ for co-ions. The values of the constants a_k are presented in Ref. [74]. The parameter R_{HO} is the Hubbard-Onsager radius of the solvent, and is expressed as

$$R_{\mathrm{HO}}^4 = e^2\frac{(\varepsilon_{\mathrm{r}}-\varepsilon_\infty)\tau_D}{64\pi^2\varepsilon_0\varepsilon_{\mathrm{r}}^2}, \tag{5.19}$$

where ε_∞ is the high frequency dielectric constant and τ_D is the Debye relaxation time, which is approximated by the expression provided by Powles [124] as $\tau_D = [3\varepsilon_{\mathrm{r}}/(2\varepsilon_{\mathrm{r}}-\varepsilon_\infty)]\tau_p$. The microscopic dipole relaxation time of the solvent τ_p is calculated as

$$\tau_p = \int_0^\infty \frac{\langle \boldsymbol{p}(0)\cdot\boldsymbol{p}(t)\rangle}{\langle \boldsymbol{p}(0)\cdot\boldsymbol{p}(0)\rangle}\mathrm{d}t. \tag{5.20}$$

The expression in Eq. (5.20) involves estimating the dipole-dipole correlation function $\langle \boldsymbol{p}(0)\cdot\boldsymbol{p}(t)\rangle$, which was computed using a bulk EMD simulation. Additionally, the high frequency dielectric constant $\varepsilon_\infty \ll \varepsilon_\mathrm{r}$, and is therefore neglected in present calculations, resulting in $\tau_D \approx 1.5\tau_p$. We plot the dependence of Hubbard-Onsager radius with reduced density of SPC/E water at 300 K in Fig. 5.1, where it can be seen that R_HO decreases with increasing water density. These observations are consistent with previously reported trends of R_HO vs. water density at higher temperatures (400 K and 600 K) [73]. At this stage, all inhomogeneities of material properties due to confinement effects have been included in the model. In the next section we discuss the GLE based friction model for electroosmotic slip.

5.1.5 Solvent interfacial friction due to charged wall: boundary conditions

In this section, we present the methodology to estimate the friction ζ_0 between charged wall and a polar solvent. We begin with the analysis first presented by Huang and Szlufarska [71] that was later adapted for SPC/E water near uncharged wall [17] and binary mixtures [14]. The friction contribution ζ_0^j from a single solvent particle j in the interfacial region can be expressed as

$$\zeta_0^j = \frac{\int_0^\infty \langle f_{x,j}^\mathrm{wf}(0) f_{x,j}^\mathrm{wf}(t)\rangle \mathrm{d}t}{k_\mathrm{B}T + \int_0^\infty \langle v_{x,j}(0) f_{x,j}^\mathrm{wf}(t)\rangle \mathrm{d}t}, \tag{5.21}$$

where $f_{x,j}^\mathrm{wf}$ and $v_{x,j}$ are the instantaneous streaming direction wall-solvent force and velocity of the solvent particle near the solid wall. The time correlation appearing in the numerator is the wall-solvent FACF, while the denominator contains wall-solvent FVCCF. The angular brackets $\langle . \rangle$ denote the ensemble average of the quantities. Exploiting the additive nature of the friction, the total value of the macroscopic friction coefficient is obtained by adding the contributions from all interfacial solvent particles as $\zeta_0 = \sum_j \zeta_0^j$. This value of solvent friction is further used to calculate the EOF slip velocity described by Eq. (5.5), resulting in the closure of the EOF model.

The trajectory of the representative solvent particle j is generated using the coarse-grained phenomenological dynamical framework of GLE [17, 14, 15, 145, 16]. The relevant equations of motion of the representative particle include a dissipative, non-Markovian friction force and its corresponding random force that is orthogonal to the particle velocity, as explained in the Mori-Zwanzig projection operator formalism [105, 180, 58].

The equations of motion can be written as

$$m_0 \frac{\mathrm{d}v_{z,j}(t)}{\mathrm{d}t} = -m_0 \int_0^t K_0(t-t')v_{z,j}(t')\mathrm{d}t' + f_{z,j}^{\mathrm{tot}}(t) + R_{z,j}(t), \tag{5.22a}$$

$$m_0 \frac{\mathrm{d}v_{x,j}(t)}{\mathrm{d}t} = -m_0 \int_0^t K_0(t-t')v_{x,j}(t')\mathrm{d}t' + f_{x,j}^{\mathrm{tot}}(t) + R_{x,j}(t), \tag{5.22b}$$

$$\frac{\mathrm{d}z_j(t)}{\mathrm{d}t} = v_{z,j}(t), \quad \frac{\mathrm{d}x_j(t)}{\mathrm{d}t} = v_{x,j}(t), \tag{5.22c}$$

where m_0 is the mass of the particle j representing the solvent molecule, $v_{z,j}$ and $v_{x,j}$ are its instantaneous velocities, and $f_{z,j}$ and $f_{x,j}$ are the structure based forces acting on the particle in the confined and streaming direction, respectively. The random forces $R_{z,j}(t)$ and $R_{x,j}(t)$ in the corresponding directions have zero mean, i.e., $\langle R_{x/z,j}(t)\rangle = 0$, and they follow the fluctuation-dissipation theorem as $\langle R_{x,j}(0)R_{z,j}(t)\rangle = m_0 k_{\mathrm{B}}TK_0(t)\delta_{xz}$, with δ_{xz} being the Kronecker delta. In addition to that, being orthogonal to the velocity [58], they also satisfy $\langle v_{x/z,j}(0)R_{x/z,j}(t)\rangle = 0$. The memory function of the solvent $K_0(t)$ is assumed to be isotropic and therefore ensures the identical statistical properties of the thermal noise in both streaming and confined directions. The memory function is assumed to be same as that of the bulk water at density 33.46 molecules/nm^3.

The structure based instantaneous force values on the particle are sampled using the static mean force maps as $f_{z,j}^{\mathrm{tot}}(t) = F_z^{\mathrm{tot}}(z_j(t))$, and $f_{x,j}^{\mathrm{tot}}(t) = F_x^{\mathrm{tot}}(x_j(t), z_j(t))$. It has been demonstrated earlier by Sanghi and Aluru [144], that the GLE formulation in Eq. (5.22a) is sufficient in accurately describing the dynamics of the representative particle in the confined direction. In their work, the 1D variation of structure based force is calculated as $F_z^{\mathrm{tot}}(z) = -\mathrm{d}U_{\mathrm{1D}}^{\mathrm{tot}}(z)/\mathrm{d}z$, where $U_{\mathrm{1D}}^{\mathrm{tot}}(z)$ is the 1D variation of the solvent total PMF. The total PMF, in turn, can be evaluated from the density profile of solvent as $U_{\mathrm{1D}}^{\mathrm{tot}}(z) = -k_{\mathrm{B}}T\log(\rho_0(z)/\rho_{0,\mathrm{b}})$, where $\rho_{0,b}$ is the density of the solvent in the bulk like center region of the confinement.

The streamwise force map ($F_x^{\mathrm{tot}}(x,z)$) is periodic in the x-direction, reflecting the lattice structure of the wall on the solvent. Additionally, its amplitude decays in the z-direction, and becomes zero beyond the interfacial region as the solvent is homogenized. Therefore, 2D maps of $F_x^{\mathrm{tot}}(x,z)$ and $F_x^{\mathrm{wf}}(x,z)$ are required to capture the effects of lattice structure on the solvent friction coefficient. We compare the force maps computed using the EMD simulations, at the location of the solvent density peak, for NaCl and SPC/E water system confined between silicon walls, in Fig. 5.2. It can be noted that near the interface, the wall-solvent forces are dominant and they approximate the total forces on the solvent as $F_x^{\mathrm{tot}}(x,z) \approx F_x^{\mathrm{wf}}(x,z)$. Further, the wall-solvent electrostatic contribution to the streamwise forces is also found to be negligible. Based on these observations, one can deduce that the wall-solvent LJ forces are the pertinent forces for simulating the

GLE based interfacial dynamics. Their 2D map can be analytically computed as discussed in Chapter 3, and is used to solve the streamwise direction GLE (Eq. (5.22b)). Details to solve the GLE framework are provided in Sec. 5.2, and the accuracy of the correlations computed using GLE framework with respect to the EMD simulations is discussed in Sec. 5.3.

5.2 Simulation Details

We perform different types of MD simulations in the present work using the LAMMPS package [123]. Water is modeled using the SPC/E model [10]. Ions are considered as monovalent ($\tilde{z}_\pm = \pm 1$), and modeled as 12–6 LJ spheres with point charges at their center. LJ interaction parameters for unlike particles are estimated using the Lorentz-Berthelot combination rules and are truncated at 1.4 nm. In this work, we consider sodium and chloride ions as cation and anion, respectively, with the ion-water force-field parameters provided by Smith and Dang [149], which have yielded good estimates of transport properties such as viscosity [116]. Water and graphene carbon interactions are modeled using the force field of Gordillo and Marti [56]. A summary of the simulation force field parameters is provided in Table 5.1. First, bulk EMD simulations of single ions in water are performed to calculate the limiting value of ionic diffusivity. Here, only short-range electrostatic interactions are considered using a cutoff value of 0.9 nm, to avoid the interaction of the ion with its periodic image. The exclusion of long-range electrostatics for single ion in bulk water EMD simulations does not introduce significant errors in computation of ionic diffusivities [91, 87]. The limiting ionic diffusion coefficient is computed using the integral of the velocity autocorrelation function (VACF) of the ion and is further used to calculate the ionic conductivity in Eq. (5.15).

In this work, we primarily consider six examples of EOF in semi-infinite slit channels made up of two different surfaces that highlight contrasting level of friction experienced by the solvent. The first class of systems consist of two single layers of graphene(Gr) separated by 3.804 nm, while the other has two four-layered silicon(Si) sheets oriented in [111] direction and separated by 3.49 nm. Additionally, to study electroosmotic flow reversal, we consider a 1.2 M solution of NaCl confined between two silicon walls with high wall charge density ($\sigma_{\text{wall}} = -0.2852$ C/m^2). Channel separation width is defined as the distance between the innermost layers of top and bottom walls. For each wall, only the innermost layer in contact with the fluid is charged, with a wall charge value of $q_w = -(N_+ - N_-)e/N_w$, where N_+ is the number of cation particles, N_- is the number of anion particles, and N_w is the number of innermost wall particles. The slit systems are periodic in x and y directions. In the z direction, a vacuum layer of size five times of the channel width separates the periodic images to exclude their interactions. Out of the six cases considered, four consist

only of single ions (cation or anion) solvated in the confined water. In these cases, the charge neutrality is not achieved in the center region of the channel, leading to a large EDL and consequently high Debye lengths. In addition to pure counter-ion cases, we also consider the presence of co-ions in confined water to understand the EOF in small Debye length situations. Subsequently, confined MD (both equilibrium and non-equilibrium) simulations are performed to compute the relevant quantities as a benchmark. For all of the MD simulations involving multiple ions in water, long range electrostatic interactions are considered via Particle-Particle Particle-Mesh (PPPM) method to ensure accuracy in computed forces. The temperature of the fluid (both ion and solvent) is set at 300 K using the Nosé–Hoover thermostat [110] with a time constant of 0.2 ps. In the NEMD simulations, the thermostat is not coupled to the streaming direction to avoid any artifacts in the simulation. The equations of motion are integrated using the velocity-Verlet algorithm with a timestep of 1 fs. Table 5.2 provides the values of wall charge density, the applied electric field to generate EOF, along with nomenclature of the cases under consideration for brevity.

For EMD simulations, systems are equilibrated for 5 ns. After that, a production run of 10 ns is performed. Data is stored at every 5 fs for the computation of VACF in the bulk EMD simulations, and every 20 fs in confined EMD cases for computing the relevant time correlations in Eq. (5.21). For NEMD simulations, the EOF is allowed to develop for 10 ns, and subsequently, a production run is performed for 15 ns to obtain the fully-developed, steady state velocity profiles, with data stored at every 0.1 ps. The macroscopic quantities from each case are ensemble averaged over 10 statistically identical MD simulations, which differ by the initial configuration of particles and seed of Maxwellian velocity distribution.

In the transport model, the slip plane location (δ) is defined using the tolerance on the solvent density as 10^{-3} molecules/nm^3, and it is approximately one solvent molecular diameter ($1\sigma_0$) away from the wall. To compute the species interfacial friction, 2D GLE simulations are performed with a time step of 0.01 ps. About 5×10^4 instances of particle trajectories of 500 ps are generated to compute the relevant time correlations. Data is saved at every other step (0.02 ps) and the first 100 ps are discarded to allow for equilibration. The numerical method for the time integration of the GLE is outlined elsewhere [144].

As a metric of speedup, we compare the Central Processing Unit (CPU) time, which is real wall-clock time times the number of parallel processors in a simulation. A representative GLE simulation for 100 independent particles (single processor task) for 100 ps equilibration and 400 ps production run takes about 20 seconds of CPU time. Such small computation time permits us to perform GLE calculations on a personal workstation in contrast to MD simulations, which require massive parallelization. The continuum formulation typically takes 5 seconds, where meaningful data for velocity profiles from NEMD simulation requires 11520 CPU hours of production runs.

5.3 Results

In this section, we compare the accuracy of the proposed multiscale transport model for EOF by comparing its predicted velocity profiles against the NEMD simulation results. We first elucidate the limitations of the classical model for the 1D EOF that uses the mean-field Gouy-Chapman model for the ion concentration profiles, in conjunction with a constant viscosity based 1D Stokes equation with no-slip boundary conditions for the solvent velocity profile. In the classical model, Neumann boundary condition of the wall charge density are applied at the slip plane. The classical EOF model is different from the multiscale transport model in several aspects. First, since it assumes a mean-field distribution of ions, it leads to a different measure of the driving force on the solvent (see second term in Eq. (5.1)). Second, due to the assumption of a constant value of the solvent viscosity, the effects of viscosity enhancement due to the interfacial layering of the solvent and ions is not captured. Finally, the effects of interfacial slip are also absent in the classical model. The limitations of the classical model in predicting the velocity profile of a nanoscale EOF can be understood from Figs. 5.3(a) and 5.3(b), where we compare its results with the NEMD calculations for the NaCl-Si case for conventional ($\sigma_{\text{wall}} = -0.0621$ C/m^2) and reversed ($\sigma_{\text{wall}} = -0.2852$ C/m^2) EOF. For low wall charge case, it can be clearly observed that although the general features of the nanoscale EOF are resolved using the classical model, it lacks the quantitative accuracy. However, for high wall charge case, the flow reversal phenomena is completely misrepresented by the classical model as it does not account for the aforementioned attributes.

The proposed multiscale transport model seeks to correct the deficiencies of classical EOF model. Here, we first estimate the viscosity variation in the nanochannel. To compute the viscosity profile, we calculate the relative dielectric permittivity profile $\varepsilon_{\text{r}}(z)$ of SPC/E water using the polarization model (Eq. (5.9)). We plot the resultant permittivity profile for NaCl-Si system ($\sigma_{\text{wall}} = -0.0621$ C/m^2) in Fig. 5.4(a) and compare it with the EMD value computed using the method illustrated in Ref. [32]. A reasonable agreement between the two profiles is observed, and therefore the polarization model is subsequently used to estimate the variation of the relative permittivity in all the cases considered. Next, we estimate the inhomogeneity in the ionic conductivity. To this end, we first calculate the limiting value of the ion diffusion using ion VACF obtained from bulk ion EMD simulations described in Sec. 5.2 as

$$D^0_{\pm} = \frac{1}{3}\int_0^{\infty} \langle \boldsymbol{v}_{\pm}(0) \cdot \boldsymbol{v}_{\pm}(t) \rangle \mathrm{d}t, \tag{5.23}$$

where the vector value of ion velocity is used to calculate the VACF as it is isotropic in a bulk system. We obtain the values $D^0_+ = 1.26 \times 10^{-3}$ nm^2/ps and $D^0_- = 2.28 \times 10^{-3}$ nm^2/ps. The resultant ionic conductivity

profiles of $Na^+$and Cl^- ions computed using Eqs. (5.16) and (5.17) for the NaCl-Si ($\sigma_{\text{wall}} = -0.0621$ C/m^2) system are plotted in Fig. 5.4(b). It can be understood from the plot that the ionic conductivities in the interfacial region show oscillations due to the interfacial layering of the ions, and the location of their minimum value is consistent with the location of the peaks of the ionic strength profile (Fig. 5.4(c)).

The phenomenon of interfacial solvent thickening can be understood from Eq. (5.8) that displays an inverse relationship between ionic conductivities and solvent viscosity. As the ion mobility in the interfacial region is significantly hindered, the resultant interfacial viscosity of the surrounding solvent is increased [135, 172]. For confirmation, we also plot the variation of the excess part of the viscosity due to the electrostatic effects $\mu_{\text{ex}}(z)$ for the NaCl-Si system ($\sigma_{\text{wall}} = -0.0621$ C/m^2) in Fig. 5.4(d) where it can be seen that it closely resembles the ionic strength profile. For higher wall charge case of NaCl-Si system ($\sigma_{\text{wall}} = -0.2852$ C/m^2), the separate pure-component and excess components of the viscosity are plotted in Fig. 5.5(a), where the excess contribution to the viscosity is very high near the interface reflecting its dependence on the Na^+ concentration peak. Around $z = -1.5$ nm, the excess component (μ_{ex}) is minimum while the pure component contribution (μ_{P}) is maximum. Here, μ_{ex} and μ_{P} are also comparable in magnitude and, as we will demonstrate later, have significant effects on the EOF velocity profile in this region. For this case, we also calculated the viscosity using the Stokes-Einstein (SE) relationship as

$$\mu(z) = \frac{k_{\text{B}}T}{3\pi d_{\text{s}} D(z)}, \tag{5.24}$$

where $D(z)$ is the self-diffusion coefficient of the solvent calculated using EMD simulations with the method of Předota et al. [129, 128], and $d_{\text{s}} = 0.24$ nm is the Stokes diameter. We compare the EMD+SE computed viscosity with the viscosity model predictions in Fig. 5.5(b). A semi-quantitative agreement between the two methods is observed, with the SE method also predicting two distinct regions of viscosity enhancement in the interfacial region. This can be understood by the non-monotonic variation of water diffusion coefficient in the interfacial region as shown in Fig. 5.5(c). We would comment on the effect of the viscosity variation on the subsequent velocity profiles later in the text.

We now compare the friction coefficient defined in Eq. (5.21) and the intermediate time correlations obtained using GLE versus EMD calculations. We consider the contributions from the representative solvent particles in the small interfacial region [64, 71], which is defined as the region spanned from the wall up to a cutoff distance of $1\sigma_0$ normal to the wall. We use the initial time occupancy based method to compute the time correlations, where all particles present in the interfacial region at an initial time are considered in the computation of total friction, regardless of their final location [122]. We present the FACF for Na-Gr

(Fig. 5.6(a)), Cl-Gr (Fig. 5.6(b)), and NaCl-Gr (Fig. 5.6(c)) systems, where a good comparison between GLE and EMD computed correlations is observed. It can also be inferred from the plots that the variance of FACF is higher for the positively charged wall system (Cl-Gr), as compared to the negatively charged wall systems (Na-Gr and NaCl-Gr). Also, the relaxation time of the FACF in Cl-Gr system is slightly higher than the other two cases. Due to the preferred orientation of the SPC/E water near a positively charged surface, the oxygen atom in the water molecule is closer to the wall compared to hydrogen atoms, leading to a higher value of attractive LJ forces. Similar observations have been presented in Ref. [78], where they have split the contributions of the FACF into LJ–LJ, LJ–ES, and ES–ES, where ES stands for electrostatic contributions. Further, they have argued that the contributions from the LJ–ES term is significantly higher than ES–ES. Therefore, the orientational effects contribute significantly to the variance of FACF. A slight increase in the relaxation time also indicates that the water molecule stays close to the positively charged wall a little longer before being re-thermalized. A similar pattern is also observed in the silicon wall cases. Also, for silicon walls -0.0621 C/m^2, the increased value of LJ energy parameter of wall-solvent pair potential along with its lattice structure gives rise to a significantly higher force variance (Fig. 5.7(a)) than those observed for graphene systems. In addition to that, a significant coupling between wall-solvent force and velocity is present as depicted by a non-zero value of FVCCF function (Fig. 5.7(b)). This phenomenon is not uniquely associated with the presence of wall charges and has been observed for a pure water case [17], where both FACF and FVCCF contribute to the interfacial friction in the case of silicon wall, compared to the graphene wall where the FVCCF is negligible. Increasing the wall charge density to -0.2852 C/m^2 also increases the friction coefficient, as understood from Figs. 5.7(c) and 5.7(d). The values of the friction coefficient for different cases are reported in Table 5.2, where the friction parameter is higher for silicon wall as compared to graphene. Also, for a similar magnitude of wall charges, its value is systematically higher for positively charged walls (compare Na-Gr with Cl-Gr and their respective silicon counterparts).

Next, we discuss the EOF velocity profiles obtained from the multiscale transport model and compare them with NEMD profiles. The EOF velocity profiles for Na-Gr and Cl-Gr cases are plotted in Figs. 5.8(a) and 5.8(b). These exhibit plug type flow and are in contrast with the EOF profiles obtained for Na-Si (Fig. 5.9(a)) and Cl-Si (Fig. 5.9(b)), where viscous contributions to the flow are apparent. This is because the friction parameter for graphene walls is almost two orders of magnitude smaller than silicon walls. The lattice structure of the graphene wall and low wall-solvent LJ energy parameter collectively provide a smooth landscape for solvent particles. Although accounted in the transport model, the viscous features of the EOF are obscured for graphene systems due to a high degree of hydrodynamic slip (see insets in Figs. 5.8(a) and 5.8(b)). Among the silicon systems, the viscous effects are more pronounced in the Cl-Si case compared

to Na-Si, which is consistent with the previous observations [135]. Since the charge neutrality is not achieved in the region far away from the wall (specifically due to the absence of co-ions), the shear stress is non-zero except at the center of the channel from symmetry considerations. This results in a non-zero strain rate, resulting in a viscosity mediated parabolic velocity profile.

For the NaCl-Si ($\sigma_{\text{wall}} = -0.0621$ C/m^2) case (Fig. 5.10(a)), because of high interfacial friction (less slip) and charge neutrality in the bulk like region of the channel, a conventional form of the EOF profile is observed where velocity gradients are pronounced in the EDL region along with a plug like behavior in the center region of the channel. The NaCl-Gr system, owing to large slip contribution again exhibits a slip dominant profile as understood from Fig. 5.10(b). However, closer inspection of the velocity profile shown in the inset displays similar viscous features as NaCl-Si system. We also studied the NaCl-Gr case with the water-graphene force-field provided by Wu and Aluru [173], for identical driving electric field ($E_x^{\text{ext}} = +0.015$ V/nm) in Fig. 5.10(c). The parameters of this force field are developed from the ab-initio calculations and predict the graphite-water contact angle in close agreement with experimental results. It is observed that the slip velocity decreases due to the hydrophilic nature of graphene wall resulting in a higher value of interfacial friction ($\zeta_0 = 9.361 \times 10^2$ kJ-ps/mol/nm^2). Based on these observations, one can conclude that the wall-solvent interaction parameters affect the flow profile in a significant manner, and our EOF model is able to capture these effects accurately.

Next, we check the model accuracy for flow reversal situations. The top subplot in Fig. 5.11 shows the concentration profiles of water and ions across the nanochannel half width calculated using the MD simulation of confined NaCl solution. Due to the phenomenon of charge inversion, the driving force becomes negative. Next, plot the streaming direction velocity profile for the NaCl-Si ($\sigma_{\text{wall}} = -0.2852$ C/m^2) with $E_x^{\text{ext}} = +0.55$ V/nm calculated using the multiscale EOF model and compare it against the NEMD profiles in Fig. 5.12(a), where a good quantitative agreement is observed. For comparison, we also plot the velocity profiles obtained from the integration of the Stokes equation with the spatial viscosity computed using the SE method. The velocity profile predicted using the SE viscosity is more accurate than the one obtained using the theoretical model for viscosity in the region -1.53 nm $< z < -1.2$ nm, where the electrical driving force is positive. This can be explained by comparing the viscosity profiles in Fig. 5.5(b). In the region -1.53 nm $< z < -1.4$ nm, the EMD viscosity is higher than that predicted from the theoretical model. As a result, the theoretical viscosity model based velocity profile rises sharply as compared to the one obtained from EMD viscosity. Further, into the confinement, the theoretical model predicts a larger value of the viscosity in the region -1.4 nm $< z < -1.2$ nm, resulting in a steeper decline of the velocity profile. Beyond $z > -1.2$ nm, the velocity profiles predicted from the two viscosities are in excellent quantitative agreement

with the NEMD profile. In the region -0.48 nm $< z < 0$ nm, the net charge density goes to zero resulting in vanishing electrical driving force (see Fig. 5.11), leading to the plug-like velocity in that region. Similar qualitative trends are also observed in the KCl solution (replacing Na^+ by K^+, keeping the same wall-charge density) as shown in Fig. 5.5(b), where we plot the EOF profile for $E_x^{\text{ext}} = +0.25$ V/nm. The quantitative differences in the velocity profiles of the two cases can be primarily attributed to the decreased value of the interfacial friction coefficient for the KCl solution ($\zeta_{0,\text{KCl}} = 4.0233 \times 10^5$ kJ-ps/mol-nm^2), which leads a higher value of slip velocity. Therefore, the presented multiscale model is applicable to both low and high wall charge density channels.

In this chapter, we have presented an interfacial friction based multiscale transport model for electroosmotic flow. Spatial inhomogeneity in the solvent viscosity is modeled with separate contributions due to the layering of solvent density and ion densities. Local viscosity variations include contributions from the solvent structure using LADM and ion concentration dependent excess contributions by the local application of Fuoss-Onsager theory, and Hubbard-Onsager electro-hydrodynamic equation based dielectric friction theory. Interfacial friction dependent slip velocity is used as the boundary condition. The friction parameter depends upon the time correlations, which are in turn computed using a refined GLE framework that uses the electrochemical wall-solvent force map as an input, and is observed to compare well with their EMD computed values. The segregation of flow profile into the slip and viscous contributions allows us to separately predict the phenomenon of interfacial thickening of the solvent and enhanced interfacial friction due to the coupling of LJ and electrostatic forces. It is inferred that the interfacial friction for a positively charged wall is higher as compared to the negatively charged wall of equal charge density magnitude. The proposed model shows good agreement of EOF velocity profiles against NEMD computed ones for a variety of input parameters such as wall-type, surface charge densities and applied electric fields, including the cases of anomalous transport such as EOF reversal.

Table 5.1: LJ interaction parameters in MD simulations of EOF.

Atom	σ (nm)	ϵ (kJ/mol)
H	0.0	0.0
O	0.317	0.6503
Na^+	0.235	0.5439
Cl^-	0.44	0.4184
C	0.339	0.2334
Si	0.3385	2.447

Table 5.2: Summary of the systems considered to study nanochannel EOF.

System	Wall type	σ_{wall} (C/m^2)	E_x^{ext} (V/nm)	ζ_0 (kJ-ps/mol/nm^2)
Na-Gr	Graphene	-0.1527	$+0.015$	7.95×10^2
Cl-Gr	Graphene	$+0.1527$	-0.02	1.131×10^3
NaCl-Gr	Graphene	-0.1018	$+0.015$	5.13×10^2
Na-Si	Silicon	-0.1242	$+0.25$	6.293×10^4
Cl-Si	Silicon	$+0.1242$	-0.15	4.692×10^5
NaCl-Si	Silicon	-0.0621	$+0.2$	3.872×10^4
NaCl-Si	Silicon	-0.2852	$+0.55$	3.458×10^7

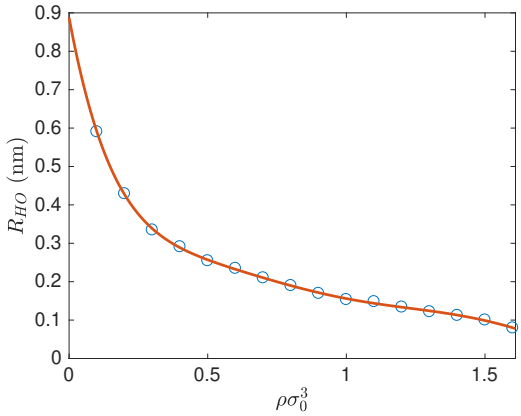

Figure 5.1: Density dependence of Hubbard-Onsager radius of SPC/E water at 300 K (blue circles) computed via EMD simulations using Eq. (5.19). Also shown (red solid line) is the 7^{th} order polynomial fit to the data.

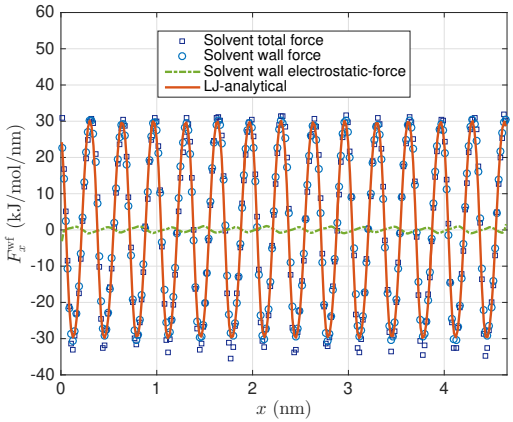

Figure 5.2: Comparison of solvent streamwise forces for NaCl and SPC/E water system confined in silicon walls ($\sigma_{\text{wall}} = -0.0621$ C/m^2). Total force (squares) contains contributions from ion-solvent, solvent-solvent, and wall-solvent interactions. Wall-solvent (circles) include LJ and electrostatic (green dashed-dot line) contributions. Also plotted is the analytical LJ force map (red solid line) computed using the method discussed in Ref. [17].

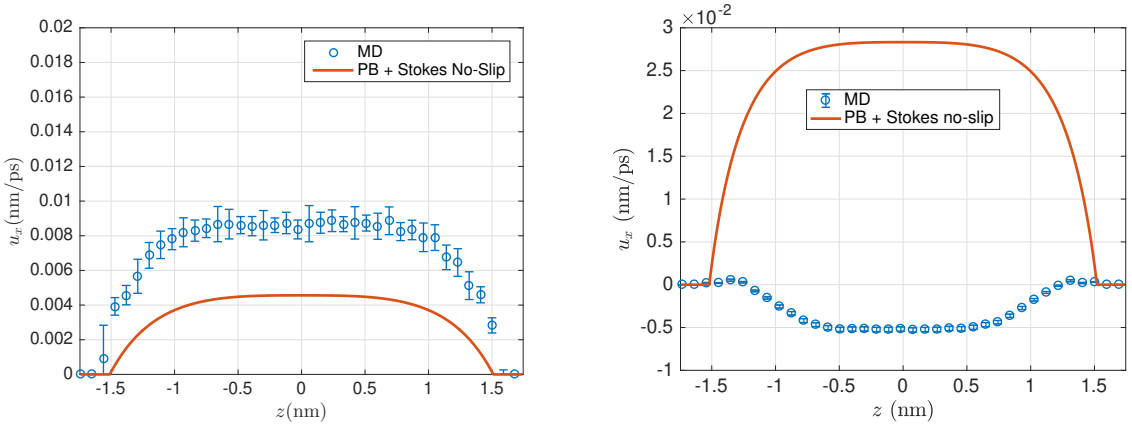

(a) (b)

Figure 5.3: Classical model predictions(using $\mu(z) = 0.65$ centiPoise) of EOF velocity profiles of NaCl-Si system for wallcharge (a) -0.0621 C/m^2, and (b) -0.2852 C/m^2. Classical results are in solid line (red), while MD results are represented by error bars (blue).

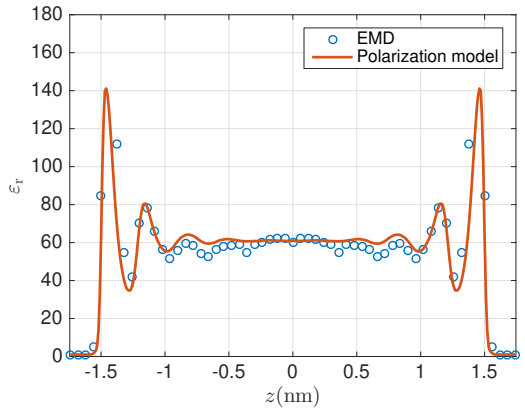

(a) Relative permittivity

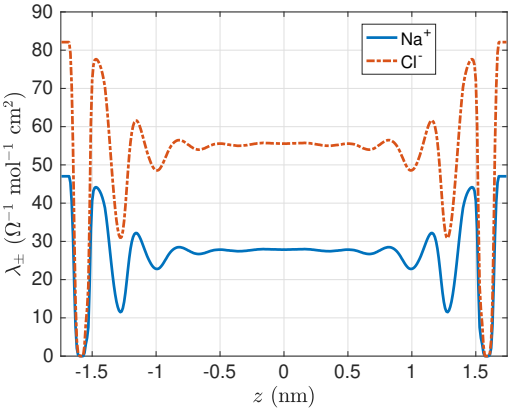

(b) Ionic conductivity

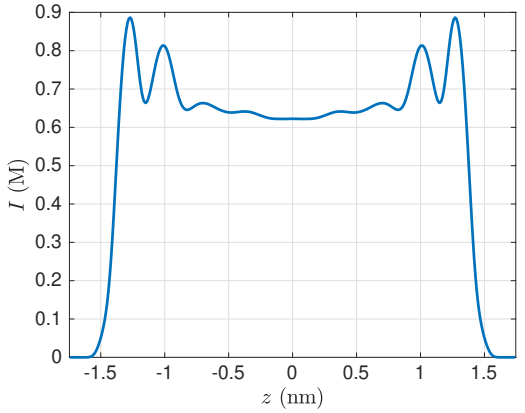

(c) Ionic Strength

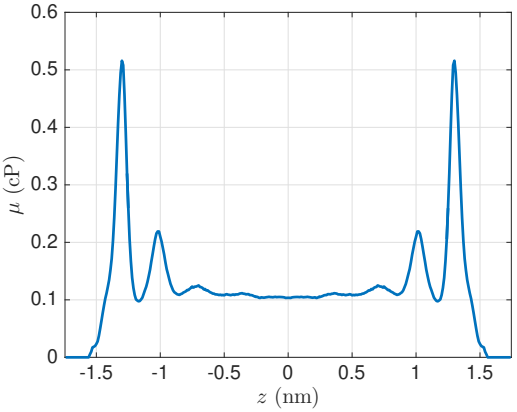

(d) Excess viscosity

Figure 5.4: (a) Relative permittivity from polarization model (red line, using $\varepsilon_{r,b} = 60$ and $\mu_d = 4.18$ Debye), and its comparison with EMD computed values (blue circles), (b) ionic conductivities, (c) ionic strength, and (d) excess viscosity for the NaCl-Si ($\sigma_{wall} = -0.0621$ C/m^2) system.

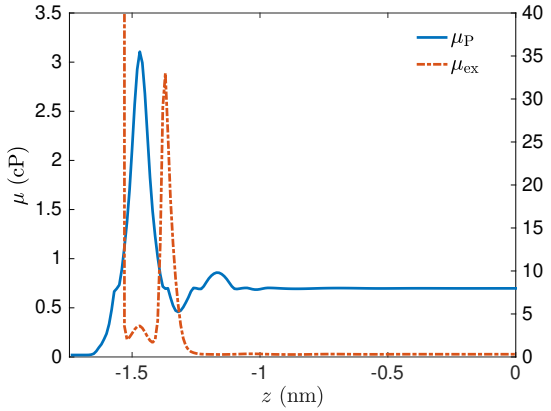

(a) μ_P and μ_{ex} components of viscosity

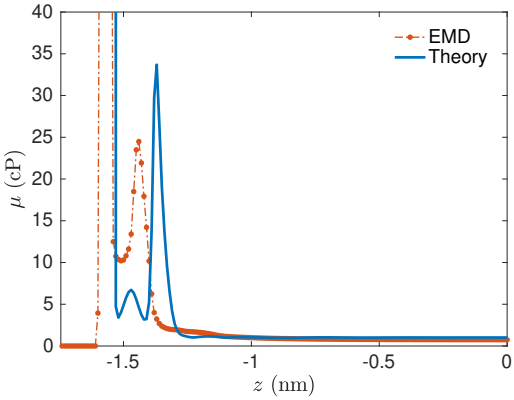

(b) Viscosity

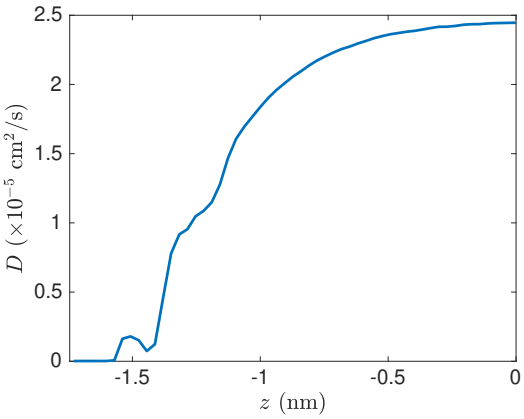

(c) Diffusion coefficient

Figure 5.5: (a) Pure component (μ_P, left axis) and excess (μ_{ex}, right axis) contributions to the local viscosity of the solvent predicted from the model for NaCl-Si ($\sigma_{wall} = -0.2852$ C/m^2). Figure (b) shows the comparison between the model predicted (LADM + Eq. (5.8)) and EMD computed (using Stokes-Einstein relation in Eq. (5.24)) local viscosities. (c) Variation of water diffusion coefficient computed using EMD simulations. Only half-width is shown because of symmetry of profiles in the z-direction.

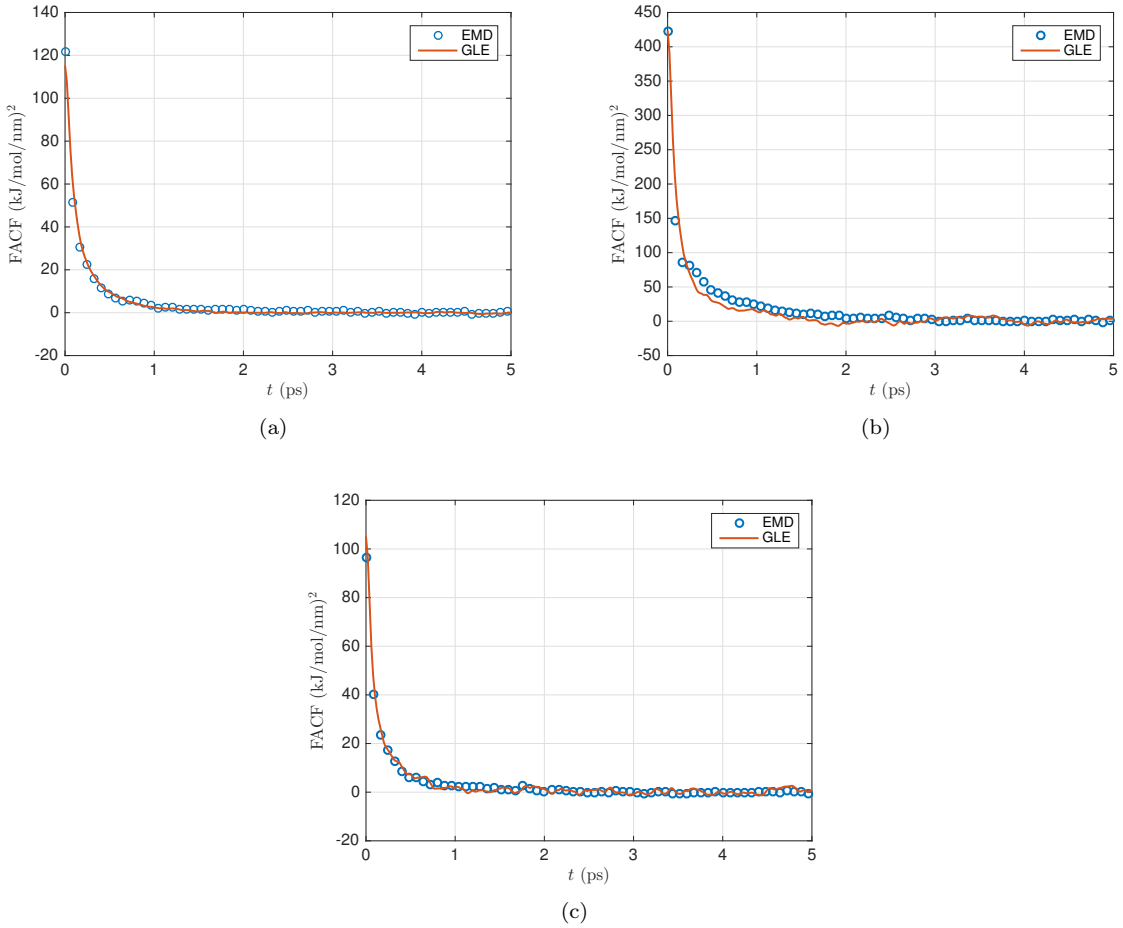

Figure 5.6: Wall-solvent FACF from GLE (bold line, red) and EMD (circles, blue) for (a) Na-Gr, (b) Cl-Gr, and (c) NaCl-Gr systems.

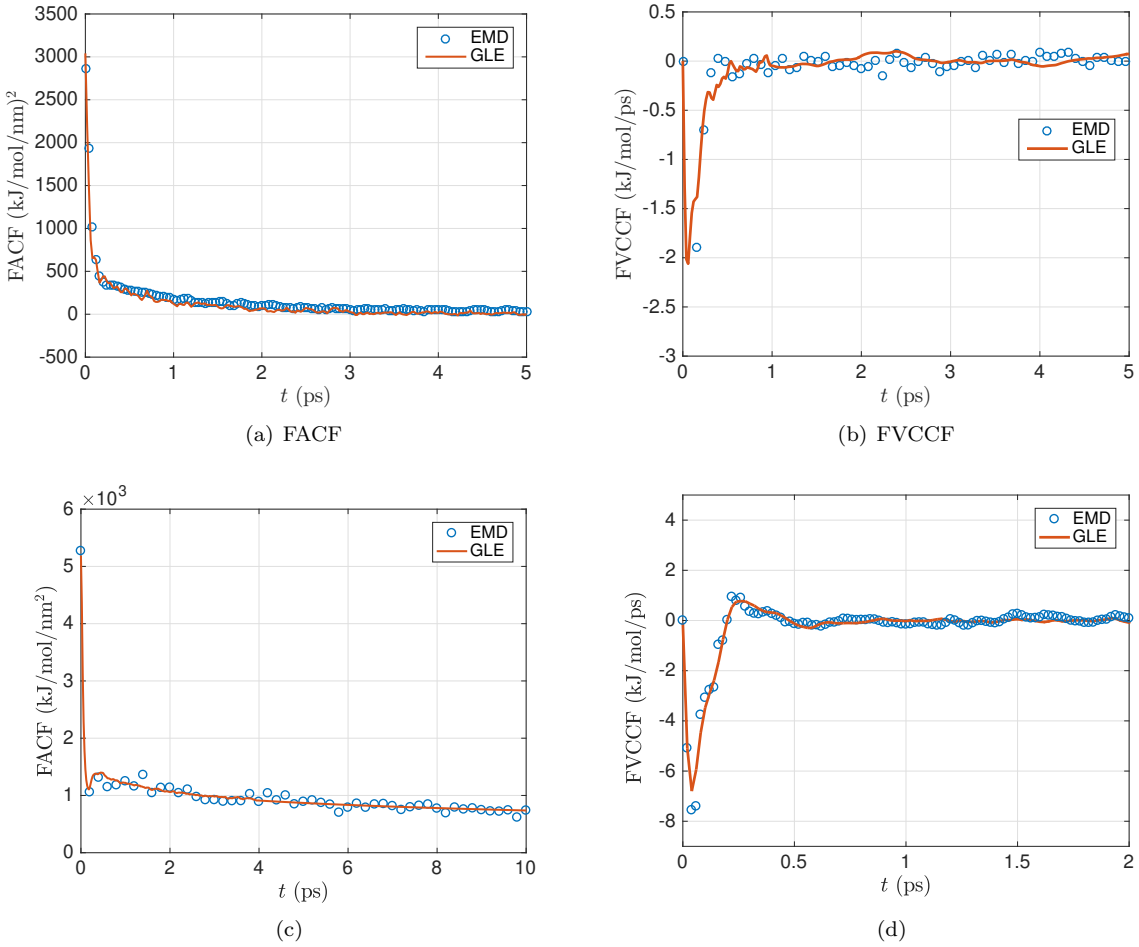

(a) FACF (b) FVCCF

(c) (d)

Figure 5.7: Wall-solvent (a) FACF, (b) FVCCF calculated using GLE (bold line, red) and EMD (circles, blue) for NaCl-Si ($\sigma_{\text{wall}} = -0.0621$ C/m^2) system, and (c) FACF, (d) FVCCF calculated using GLE (bold line, red) and EMD (circles, blue) for NaCl-Si ($\sigma_{\text{wall}} = -0.2852$ C/m^2) system.

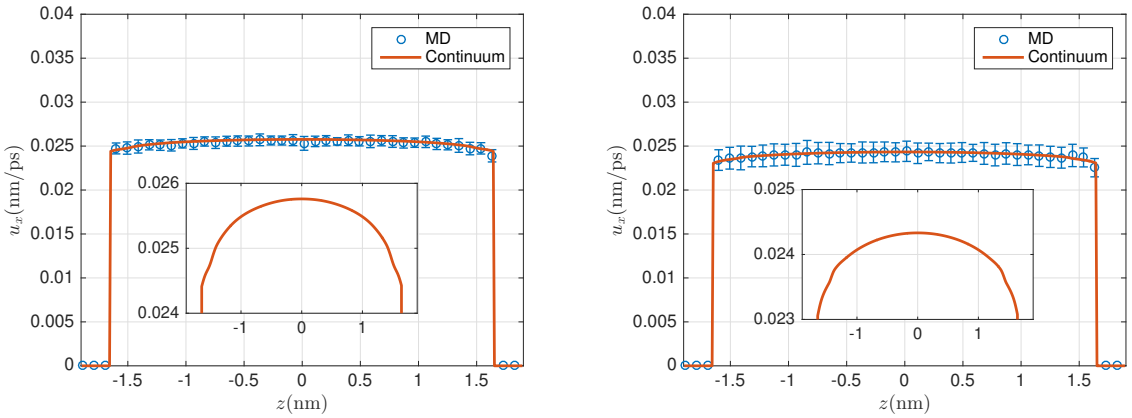

Figure 5.8: EOF velocity profiles for (a) Na-Gr, and (b) Cl-Gr systems. Continuum results are in solid line (red), while MD results are represented by error bars (blue). Insets show the viscous contributions from multiscale transport model to the EOF in more detail.

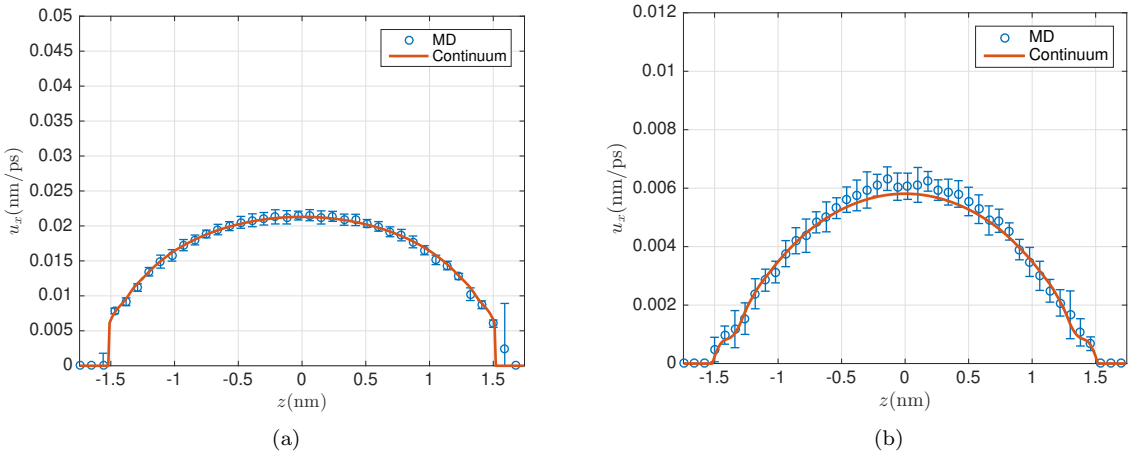

Figure 5.9: EOF velocity profiles for (a) Na-Si, and (b) Cl-Si systems. Continuum results are in solid line (red), while MD results are represented by error bars (blue).

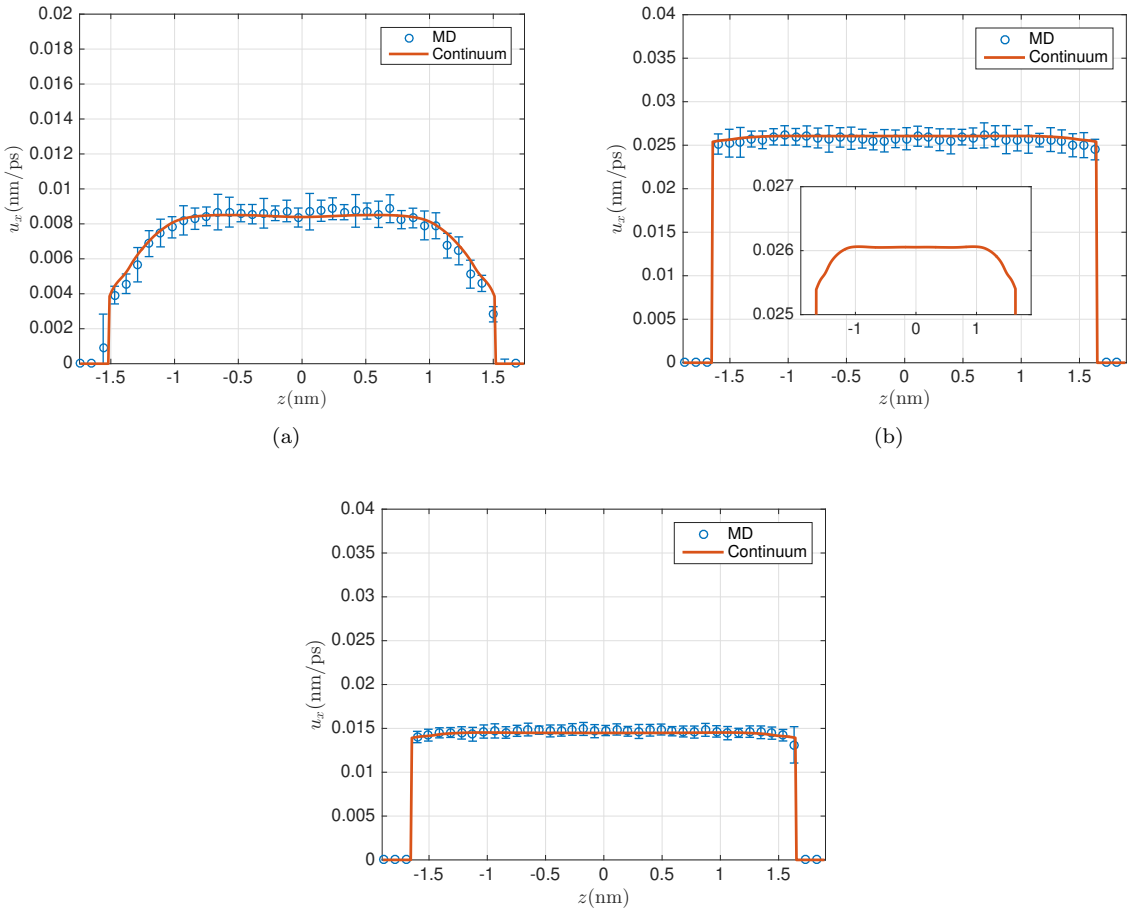

Figure 5.10: EOF velocity profiles for (a) NaCl-Si ($\sigma_{\text{wall}} = -0.0621$ C/m^2), (b) NaCl-Gr, and (c) NaCl-Gr using the force-field of carbon-water from Wu and Aluru [173]. Continuum results are in solid line (red), while MD results are represented by error bars (blue). Inset in (b) shows the viscous contributions from multiscale transport model to the EOF in more detail.

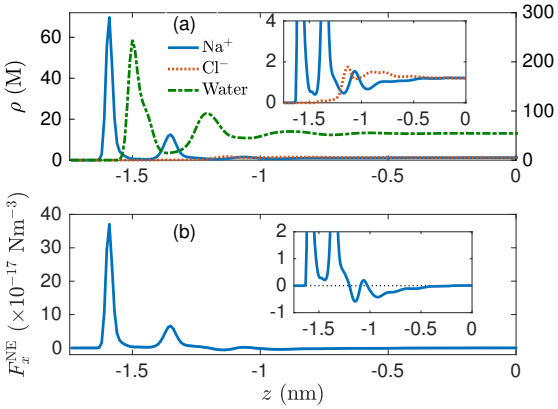

Figure 5.11: (top) Water (right axis) and ion (left axis) concentration profiles, and (bottom) electrical driving force across the confinement. Only half-width is shown because of symmetry of profiles in the z-direction.

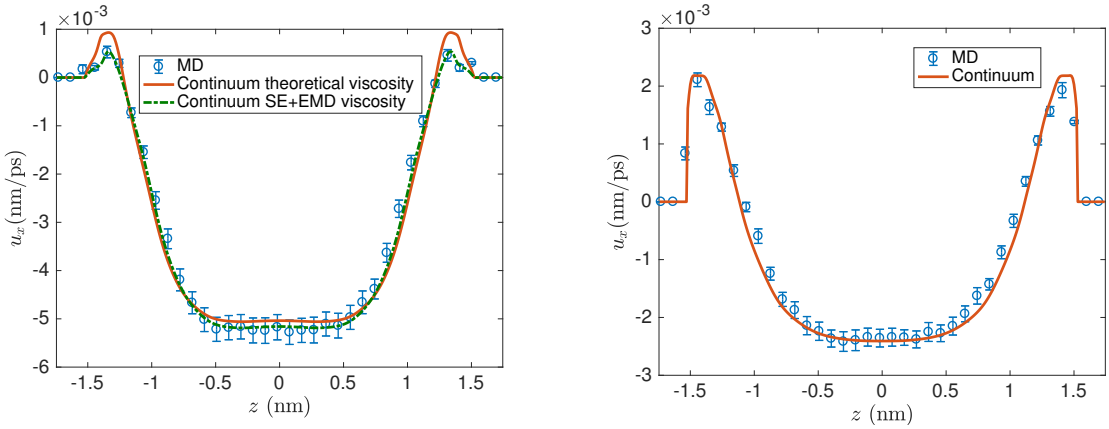

Figure 5.12: (a) Comparison of multiscale transport model EOF velocity (solid red line) with the NEMD simulations (blue circles) for NaCl-Si ($\sigma_{\mathrm{wall}} = -0.2852$ C/m^2) with $E_x^{\mathrm{ext}} = +0.55$ V/nm. Also plotted is the result of the transport model using EMD computed viscosity (green dash-dot line) using the Stokes-Einstein method from Eq. (5.24). Inset enhances the interfacial region. (b) Same as (a), but for KCl solution with $E_x^{\mathrm{ext}} = +0.25$ V/nm.

Chapter 6

Non-local continuum model for nanochannel flow

In this chapter, we present a non-local multiscale transport model to describe the confined flow in nanochannels. The point-wise constitutive relationship between the fluid shear stress and strain-rate is revised to be characterized by a viscous kernel that incorporates strain rate contributions from the neighboring points, as proposed by Evans and Morriss [Statistical Mechanics of Nonequilibrium Liquids (Cambridge University Press, 2008)]. The viscous kernel is parameterized from an isotropic bulk system using Sinusoidal Transverse Force (STF) methodology, first presented by Gosling et al. [57]. The slip effects are treated separately by computing Green-Kubo like expressions for the interfacial friction coefficient. The interfacial particle trajectories are, in turn, generated by a recently proposed Generalized Langevin Equation-based framework. The proposed model can accurately describe the velocity profiles where the length scales of strain-rate variation are of the order of the molecular diameter of the fluid. It is also able to resolve the pathological issue in the local constitutive relationship in gravity driven channel flows, where strain-rate is zero, but the shear stress is non-zero.

6.1 Background

6.1.1 Non-local constitutive relationship

In general, the non-local constitutive relationship between the stress and strain rate can be expressed as

$$\tau(\boldsymbol{r},t) = \int_{-\infty}^{+\infty}\int_{0}^{+\infty} \mu(\boldsymbol{r},t,\boldsymbol{r}',t')\dot{\varepsilon}(\boldsymbol{r}',t')\mathrm{d}t'\mathrm{d}\boldsymbol{r}', \tag{6.1}$$

where $\tau(\boldsymbol{r},t)$ and $\dot{\varepsilon}(\boldsymbol{r},t)$ are stress and strain-rate at a arbitrary point $\boldsymbol{r}$ and time t, and are related via the viscous kernel $\mu(\boldsymbol{r},t,\boldsymbol{r}',t')$ via a convolution relationship. The temporal non-locality manifests in the form of viscoelastic effects where memory effects are important. For steady state situations, the temporal

dependence is dropped, and the non-locality becomes purely spatial. It can be expressed as

$$\tau(\boldsymbol{r}) = \int_{-\infty}^{+\infty} \mu(\boldsymbol{r}, \boldsymbol{r}')\dot{\varepsilon}(\boldsymbol{r}')\mathrm{d}\boldsymbol{r}'. \tag{6.2}$$

For a homogeneous fluid, the viscous kernel in Eq. (6.2) can be assumed isotropic, and therefore only dependent on the separation distance $|\boldsymbol{r} - \boldsymbol{r}'|$, so the constitutive relationship becomes

$$\tau(\boldsymbol{r}) = \int_{-\infty}^{+\infty} \mu(|\boldsymbol{r} - \boldsymbol{r}'|)\dot{\varepsilon}(\boldsymbol{r}')\mathrm{d}\boldsymbol{r}'. \tag{6.3}$$

Todd et al. have performed numerous studies [63, 177, 36] to extract the isotropic kernel in bulk and confinement. It should be noted that, by construction, the isotropic kernel in real space is an even function and its integration in the space gives total viscosity

$$\mu_0 = \int_{-\infty}^{+\infty} \mu(r)\mathrm{d}r, \tag{6.4}$$

where μ_0 is the viscosity of the fluid. In the Fourier (k) space, the convolution relationship can be expressed as a multiplication of Fourier coefficients of stress and strain-rate as

$$\tilde{\tau}(\boldsymbol{k}) = \tilde{\mu}(\boldsymbol{k})\tilde{\dot{\varepsilon}}(\boldsymbol{k}), \tag{6.5}$$

where the Fourier transform of stress is defined as

$$\tilde{\tau}(\boldsymbol{k}) = \int_{-\infty}^{+\infty} e^{i\boldsymbol{k}\cdot\boldsymbol{r}}\tau(\boldsymbol{r})\mathrm{d}\boldsymbol{r}, \tag{6.6}$$

and in similar manner for viscous kernel and strain rate. It should be noted that Fourier transform of the viscous kernel returns k-space viscosity, which is a measure of relaxation of different modes of momentum perturbations of the fluid. The viscosity of the fluid, therefore can be interpreted as the long wavelength limit of the k-space viscosity as $\mu_0 = \tilde{\mu}(k \to 0)$. If the information about the stress and strain-rate is known, the k-space viscosity can be easily computed from Eq. (6.5), and inverted back to real space to obtain the viscous kernel.

6.1.2 Parameterization of viscous kernel: STF Method

The STF method [57], is a robust approach to extract transport properties. In the present context, we discuss it to calculate wave-vector dependent viscosities. Here, a homogeneous fluid is subjected to a sinusoidal shear by the application of sinusoidal gravity that is modulated in the direction transverse to the flow direction as

$$g_x(z) = g_0 \sin(k_z z), \tag{6.7}$$

where x is the streamwise direction, and z is arbitrarily chosen as the transverse direction, k_z is the wave-vector in the z-direction, and can be represented as $k_z = 2n\pi/L_z$ for $n = 1, 2, 3\ldots$ representing the fundamental and higher order modes of gravity perturbation. For the remainder of the paper, we drop the subscript from k_z, noting the conclusions remain valid for isotropic fluid.

The steady state momentum conservation equation can be represented as

$$\frac{\mathrm{d}\tau(z)}{\mathrm{d}z} + m\rho_0 g(z) = 0, \tag{6.8}$$

where m is the mass, and ρ_0 is the bulk density of the fluid. In k-space, the momentum conservation equation can be recast as $\tilde{\tau}(k) = -im\rho_0\tilde{g}(k)/k$. Since the strain rate is the gradient of the velocity field ($\dot{\varepsilon}(z) = \mathrm{d}u(z)/\mathrm{d}z$), therefore $\tilde{\dot{\varepsilon}}(k) = -ik\tilde{u}(k)$. Further, using Eq. (6.5), one can write the expression for k-space viscosity as

$$\tilde{\mu}(k) = \frac{m\rho_0\tilde{g}(k)}{k^2\tilde{u}(k)}. \tag{6.9}$$

For the choice of the gravity field in Eq. (6.7), $\tilde{g}(k) = g_0$. When the shear rate is small, no additional harmonics are present in the velocity profile. The Fourier coefficient of the velocity field $\tilde{u}(k)$ can be computed using a NEMD simulation of the unconfined fluid with the sinusoidal gravity perturbation. It can be represented as

$$\tilde{u}(k) = \frac{2}{N}\sum_{i=0}^{N} \sin(kz_i)v_{x,i}, \tag{6.10}$$

where z_i is the position of the particle i, and $v_{x,i}$ is the streaming direction velocity. The summation runs over all particles N inside the box. Eq. (6.8) results in the efficient computation of the k-space viscosity, which can then be fitted into suitable analytic functional form and inverted to obtain real space viscous kernel. The question whether the k-space viscosity is analytic about $k = 0$ is an open problem. Mode-coupling theory of viscosity predicts that k-space viscosity is non-analytic about $k = 0$, and therefore the higher order Burnett coefficients do not exist. Non-analyticity of the k-space viscosity is also supported

by the computer simulations of soft spheres performed by Evans [46]. However, subsequent simulations of Travis et al. [165] have shown that the data can be fitted to both analytic and non-analytic forms. We choose a two Gaussian form, first proposed in Ref. [63] that is analytic. The attractive feature of using this functional form is that it avoids performing a numerical inverse Fourier transform of the k-space viscosity to compute the real space viscous kernel. The k-space viscosity functional form can be represented as

$$\tilde{\mu}(k) = \frac{\mu_0}{2}\left(\exp\left(\frac{-k^2}{2s_1^2}\right) + \exp\left(\frac{-k^2}{2s_2^2}\right)\right), \tag{6.11}$$

for which the real space kernel becomes

$$\mu(z) = \frac{\mu_0}{2\sqrt{2\pi}}\left(s_1 \exp\left(\frac{-z^2 s_1^2}{2}\right) + s_2 \exp\left(\frac{-z^2 s_2^2}{2}\right)\right). \tag{6.12}$$

Here, s_1 and s_2 are the parameters of the fit, and have the units of inverse length. The viscous kernel can also be rewritten as $\mu(z) = \mu_0 f(z)$, where the weight function $f(z)$ satisfies the normalization condition $\int_{-\infty}^{+\infty} f(z)\mathrm{d}z = 1$. The usefulness of separating the viscous kernel in this form would be leveraged in the non-local transport model for channel geometries, discussed in the next section.

6.2 Transport model

6.2.1 Non-local formulation in slit channel

In this section, we investigate the feasibility of utilizing the non-local constitutive relationship to solve for the velocity profiles. The system of interest is fluid confined between slit-shaped nanochannel, where the two walls are separated by the distance L in the z-direction. A constant gravity force g_x is applied in the streamwise (x) direction. The momentum conservation equation in the steady state can be written as

$$\frac{\mathrm{d}\tau(z)}{\mathrm{d}z} + mg_x\rho(z) = 0, \tag{6.13}$$

where the density is considered to be varying across the confinement due to the molecular nature of the fluid. The above equation can be readily integrated to obtain the stress profile

$$\tau(z) = -mg_x \int_0^z \rho(z')\mathrm{d}z'. \tag{6.14}$$

Here, we have assumed that shear stress at the center of the channel is zero due to the symmetry considerations. Once the shear stress is known, we can utilize its variation to solve for the velocity profiles by invoking the non-local constitutive relationship

$$\tau(z) = \int_{z-\Delta}^{z+\Delta} \mu(z, z'-z)\frac{\mathrm{d}u}{\mathrm{d}z'}\mathrm{d}z', \tag{6.15}$$

where Δ is the support of viscous kernel, and it depends upon the choice of the fluid and the thermodynamic state. It is typically of the order of two to three molecular diameters for simple fluids. The viscous kernel in the confinement, unlike bulk, is not isotropic. This is because the local density is variable in the channel, and as a result it locally alters the thermodynamic state of the fluid. Like bulk, we further separate the inhomogeneous viscous kernel as

$$\mu(z, z'-z) = \mu_0(z) f(z, z'-z), \tag{6.16}$$

where it is assumed the local viscosity varies across the confinement. This assumption is similar in spirit of the variable separable form proposed by Cadusch et al. [36] ($\mu(z, z'-z) = W(z)\mu(z'-z)$), with subtle differences. First, their choice of the function $W(z)$ as a top-hat function $\Pi(z)$ is motivated by finite size of the domain in the confined direction, and therefore it cannot be parameterized with a physical motivation. Second, we still retain the position dependence in weight function $f(z, z'-z)$. This is because the parameters of the functional form of homogeneous kernel in Eq. (6.12) have been shown to be density dependent in bulk systems [63].

It can be understood that the above equation can be recast into a higher order differential equation in streaming velocity by a suitable change of variable in the integral, and subsequently performing a Taylor series expansion of strain-rate. The coefficients of the higher order velocity gradient terms are moments of the viscous kernel. This approach, however, is not amenable to solve for the velocity profile as typically a Dirichlet or Robin type boundary condition is known. In what follows, we discuss a Jacobi like iterative scheme to solve for the velocity profile.

We first decompose the shear stress into local and non-local constituents as

$$\tau(z) = \tau_{\mathrm{L}}(z) + \tau_{\mathrm{NL}}(z), \tag{6.17}$$

where the local shear stress is represented by the typical point-wise stress strain-rate relationship

$$\tau_{\mathrm{L}}(z) = \mu_0(z)\frac{\mathrm{d}u}{\mathrm{d}z}, \tag{6.18}$$

and consequently, the non-local local contribution is represented by subtracting the local shear stress from the total shear stress

$$\tau_{\mathrm{NL}}(z) = \mu_0(z)\left[\int_{-\Delta}^{+\Delta} f(z,\theta)\frac{\mathrm{d}u}{\mathrm{d}\theta}\bigg|_{z+\theta}\mathrm{d}\theta - \frac{\mathrm{d}u}{\mathrm{d}z}\right], \tag{6.19}$$

where we have used $z' - z = \theta$ in Eq. (6.15). To start the iterative scheme, we neglect the non-local contribution and solve the Stokes equation with slip boundary condition to obtain the zeroth-iterate velocity profile ($u^{(0)}(z)$) using the slip boundary condition

$$u\left(\pm\frac{L}{2} \mp \delta\right) = u_{\mathrm{s}}, \tag{6.20}$$

where u_{s} is the slip velocity and can be related to the interfacial friction coefficient ζ_0 as

$$u_{\mathrm{s}} = \frac{Amg_x\rho_{\mathrm{avg}}}{2\zeta_0}. \tag{6.21}$$

The friction can be computed using the GLE formulation discussed previously. Once $u^{(0)}(z)$ is estimated, the non-local shear stress can be evaluated from Eq. (6.19) and the iterative scheme can be continued by solving

$$\mu_0(z)\frac{\mathrm{d}u^{(k+1)}}{\mathrm{d}z} = -mg_x\int_0^z \rho(z')\mathrm{d}z' - \tau_{\mathrm{NL}}^{(k)}(z), \tag{6.22a}$$

$$\tau_{\mathrm{NL}}^{(k)}(z) = \mu_0(z)\left[\int_{-\Delta}^{+\Delta} f(z,\theta)\frac{\mathrm{d}u^{(k)}}{\mathrm{d}\theta}\bigg|_{z+\theta}\mathrm{d}\theta - \frac{\mathrm{d}u^{(k)}}{\mathrm{d}z}\right], \tag{6.22b}$$

successively by using the slip velocity boundary condition (Eq. (6.20)).

6.2.2 Viscosity model

To model the variation of local viscosity $\mu_0(z)$, we adopt the local average density method (LADM) proposed by Bitsanis et al. [28]. In this approach, the density profile is first averaged with a weight function to obtain a local average density. This local average density, along with the operating temperature, identifies as an equivalent homogeneous bulk like system. The viscosity of this bulk system can be estimated using EMD simulations in conjunction with Green-Kubo relations. Alternatively, one can also use equation of state for viscosity where the literature is available. The local average density in this work is computed by utilizing

Tarazona weight functions as

$$\bar{\rho}(z) = \int \omega(z' - z, \bar{\rho}(z))\rho(z')\mathrm{d}z', \tag{6.23a}$$

$$\omega(z' - z, \bar{\rho}(z)) = \omega_0(z' - z) + \omega_1(z' - z)\bar{\rho}(z) + \omega_2(z' - z)\left[\bar{\rho}(z)\right]^2, \tag{6.23b}$$

where $\omega_{i=0,1,2}(z)$ are given in Ref. [167]. Once the homogeneous state of the fluid is characterized, we computed its viscosity following the correlations provided by Galliéro et al. [51], that have strong foundation by using the comprehensive dataset provided by Meier et al [104].

6.3 Simulation Details

Bulk MD simulations are performed in this work to compute the homogeneous viscous kernel. The fluid is modeled using purely repulsive Weeks-Chandler-Anderson (WCA) potential, which is expressed as

$$u_{\mathrm{WCA}}(r_{ij}) = \begin{cases} 4\epsilon_{\mathrm{ff}}\left(\frac{\sigma_{\mathrm{ff}}^{12}}{r_{ij}^{12}} - \frac{\sigma_{\mathrm{ff}}^{6}}{r_{ij}^{6}}\right) + \epsilon_{\mathrm{ff}}, & r_{ij} \leq 2^{1/6}\sigma_{\mathrm{ff}}, \\ 0, & r_{ij} > 2^{1/6}\sigma_{\mathrm{ff}}, \end{cases} \tag{6.24}$$

where ϵ_{ff} and σ_{ff} are the depth of the LJ potential well and the diameter of the fluid, respectively. They are chosen to be equal to $\epsilon_{\mathrm{ff}} = 148.1k_{\mathrm{B}}$, and $\sigma_{\mathrm{ff}} = 0.381$ nm to correspond to that of LJ Methane. The operating temperature is chosen to be 107.52 K, and density 12.62 atoms/nm^{-3}, which corresponds to a reduced temperature of 0.726 and reduced density of 0.698. The box length in z-direction L_z is chosen to be 6.7 nm, which corresponds to a minimum $k\sigma_{\mathrm{ff}} = 0.3567$ in the STF simulation.

In NEMD simulations, we consider WCA fluid confined between two silicon walls. Each wall is made up of four layers of silicon atoms arranged in the [111] direction, with lateral dimensions 4.655 nm $\times$ 4.224 nm. The interaction between the fluid atoms and the wall particles is modeled using 12–6 LJ potential, with $\epsilon_{\mathrm{wf}} = 1.7358$ kJ/mol and $\sigma_{\mathrm{wf}} = 0.3597$ nm. In NEMD simulations, the value of g_x is applied in the streaming direction.

6.4 Results

In this section, we examine the accuracy of the proposed non-local framework for bulk and confined fluids. We first compute the viscous kernel using the STF method. Different values of gravity magnitude g_0 is chosen for different modes to keep the k-space shear rate $\tilde{\dot{\varepsilon}}(k) = k\tilde{u}(k)$ to a maximum value of 0.15 ps^{-1}.

Since the k-space obtained from the STF simulation should be interpreted at the limit of zero shear rate, we first compute the zero shear rate limiting value of k-space viscosity by fitting the results to Quentrec local order theory as [136]

$$\tilde{\mu}(k,\dot{\varepsilon}) = \tilde{\mu}(k,\dot{\varepsilon}\to 0) + \frac{a\dot{\varepsilon}^2}{b+\dot{\varepsilon}^2}. \tag{6.25}$$

We plot the shear rate dependence of the k-space viscosity for first eight modes along with the fits described by Quentrec local order theory in Fig. 6.1. It can be inferred from the plot that the long wavelength modes (k near zero) have the highest viscosity, and the dependence of the shear rate is also more distinct in long wavelength modes. Higher order modes have successively lower zero shear rate k-space viscosity, and the shear rate dependence on the viscosity is weak.

Once the limiting value of k-space viscosity is computed, we plot the variation of the k-space viscosity with respect to the wavevector k alongside the Gaussian fit in Fig. 6.2. From the fit, we are able to obtain $s_1 = 5.4365$ nm^{-1}, and $s_2 = 11.6136$ nm^{-1}. Our values are very similar to the ones obtained in Ref. [63] for the same thermodynamic state of the fluid. We also plot corresponding real space viscous kernel Fig. 6.3 by using Eq. (6.12). From the plot, we are able to estimate the support of the viscous kernel to be $\Delta = 2\sigma_{\text{ff}}$. We have also verified that changing the support from $2\sigma_{\text{ff}}$ to $3\sigma_{\text{ff}}$ does not alter our subsequent results significantly.

6.4.1 Bulk fluid

For the bulk fluid, we first examine the accuracy of the local and non-local constitutive relationship by calculating the shear stress using the velocity profiles obtained from the STF-MD simulations and comparing them against the shear stress obtained by solving the conservation equation (Eq. (6.8)). We pick two distinct cases, with $k\sigma_{\text{ff}}$ equal to 0.3567 and 1.784, corresponding to the fundamental mode $n = 1$, and $n = 5$, respectively. In solving the conservation equation, we use $\tau(L_z/4) = 0$ as a boundary condition. The STF-MD velocity profiles are fitted to a functional form $u(z) = u_0 \sin(kz)$ for derivative evaluations. We compare the resultant shear stress profiles from the local and non-local constitutive relationship in Fig. 6.4. It can be seen from the plots that for the fundamental mode, both local and non-local formulation perform equally well (see Fig. 6.4(a)). This is because the strain-rate gradients in the fundamental mode do not vary appreciably over the width of the viscous kernel. As a result, the effect of the viscous kernel is akin to that of a delta function $\mu(z) = \mu_0\delta(z)$. Plugging this delta-function definition of viscous kernel reduces the non-local relation into a local one. However, when the strain-rate variations are of the order of the width of the kernel, and the non-local model is superior to the local model in predicting shear stress (see Fig. 6.4(b)). Thus, we can conclude that the non-local constitutive relation is a generic one, and only under

special circumstances becomes equivalent to the local relation.

Next, we examine the performance of the proposed iterative scheme to predict the velocity profiles of the STF simulation, provided the viscous kernel and the stress profile. As explained earlier, we begin the iterative scheme by solving the Stokes equation, which assumes a local relationship between the stress and strain-rate. Subsequent iterations are progressed by using equations similar to Eq. (6.22), with constant density $\rho(z) = \rho_0$ and viscosity $\mu(z) = \mu_0$, but variable gravity $g(z) = g_0 \sin(kz)$. We use $u(0) = u(L_z) = 0$, as a boundary condition while solving the Stokes equation. The convergence is evaluated by defining the normalized residual using the successive iterates of the velocity profile as

$$\text{Normalized residual} = \frac{\left\| u^{k+1}(z) - u^k(z) \right\|}{\| u^k(z) \|}, \tag{6.26}$$

where $\| \ldots \|$ denotes the 2-norm. The velocity profile is assumed to be converged when the normalized residual becomes smaller than 10^{-6}. We plot the residual versus number of iterations in Fig. 6.5, where it can be seen that the convergence of the iterative method is linear. We also plot the velocity profiles obtained using the non-local formulation in Fig. 6.6, where excellent agreement is observed between them and their STF-MD computed counterparts. As expected, the local model behaves accurately for $n = 1$, but deficient to predict the velocity profile $n = 5$.

6.4.2 Confined fluid

We now examine the performance of inhomogeneous viscous kernel in the confinement. As explained earlier, we hypothesize that the inhomogeneities in the viscous kernel enter in two ways. First, the local viscosity varies across the confinement. Additionally, the parameters s_1 and s_2 in the Gaussian fit show dependence on the thermodynamic state in bulk systems. Similar to the bulk case, we begin with checking the validity of local and non-local constitutive relationship in the confinement. For this exercise, we use the velocity profiles obtained from the NEMD simulation. We first smoothen the NEMD velocity profile using the quadratic-cosine functional form provided in Ref. [164], and evaluate the derivative using the fitted data. The inhomogeneous viscosity variation, modeled using LADM, is also provided as an input. We consider two channels of width $20\sigma_{\text{ff}}$ with $g_x = 5 \times 10^{-4}$ nm/ps^2 and $6\sigma_{\text{ff}}$ $g_x = 8 \times 10^{-3}$ nm/ps^2. The larger width of $20\sigma_{\text{ff}}$ channel provides a large bulk like region where local and non-local constitutive relations are expected to perform equally well. This is confirmed by plotting the shear stress in Fig. 6.7(a), although the local model changes sign within $1\sigma_{\text{ff}}$ distance away the interface, reflecting the change in the sign of strain rate due to local extremas in the velocity profile. These sign reversals of stress are absent in the non-local model

stress predictions, as the use of the kernel homogenizes the effective non-local strain-rate (bare strain rate convoluted with the function $f(z)$), compared to the bare strain rate. Nevertheless, the differences between the two definitions are minimal beyond $1\sigma_{\text{ff}}$, and they compare well with the NEMD data beyond $2\sigma_{\text{ff}}$. We interpret these deficiencies arising from the lack of information about the velocity profile in the region beyond the wall location, which results in a truncated calculation of the convoluted strain rate.

The smaller width of $6\sigma_{\text{ff}}$ channel, however, is able to highlight the differences between the two approaches. As expected, the predicted shear stress using the local model displays sign reversals consistent with the $20\sigma_{\text{ff}}$ case. Additionally, the local model is not able to capture the shear stress quantitatively except near the mid-point of the channel. The use of non-local model rectifies the sign-reversal, but still lacks the quantitative accuracy compared to the NEMD data in the region up to $1.5\sigma_{\text{ff}}$ away from the wall. We further refine our estimates in of shear stress in $1\sigma_{\text{ff}}$ region by considering a density dependence of parameter s_1, using the empirical correlations developed in Ref. [63] for bulk fluids. The variation can be represented as $s_1(\bar{\rho}) = (3.15/\sigma_{\text{ff}})(\bar{\rho}\sigma_{\text{ff}}^3)^{0.98}$, where we have used local average density as an input instead of the local density, consistent with the method of calculating viscosity profile. It should also be noted that the variation of s_2 does not change appreciably with density. However, both s_1 and s_2 are expected to change with respect to temperature, and therefore should be re-quantified for a different operating temperatures.

We now calculate and compare the velocity profiles obtained using the non-local framework (Eq. (6.22)) against NEMD simulations. For $20\sigma_{\text{ff}}$ channel width, we plot the velocity profiles in Fig. 6.8(a), where it can be seen that both non-local and local (Stokes) model perform equally well in predicting the velocity profiles, which is expected. On closer inspection, the non-local velocity profile shows oscillatory features near the interface (see inset), consistent with the NEMD velocity profile. Both models, however, are not able to capture the exact NEMD velocity profile near the interface. These deficiencies can be attributed to the theoretical model for calculating the viscosity profile. The choice of a variable kernel parameter $s_1(\bar{\rho})$ does not significantly alter the non-local velocity profile. For $6\sigma_{\text{ff}}$ channel width, however, the differences between the Stokes and non-local formulation are noteworthy (see Fig. 6.8(b)). The Stokes flow velocity profile, as expected, is unable to capture velocity gradients accurately both very close to the interface where the strain-rate changes sign, and around the center of the nanochannel. The non-local model (constant kernel) is able to capture the local extrema accurately but predicts negative velocity in the interfacial region. This behavior can be rectified by choosing a variable kernel (Fig. 6.8(c)). Similar to the $20\sigma_{\text{ff}}$ case, the mismatch of non-local model predicted velocity profiles against the NEMD ones in the interfacial region can be attributed to the viscosity model.

In this chapter, we have presented a multiscale, non-local transport model for nanochannel flow. The

non-local model postulates that the point-wise shear stress depends upon the strain-rate in its neighborhood. This dependence is characterized by a viscous kernel, which is isotropic in bulk but non-isotropic in confined systems. The non-isotropic viscous kernel can easily be parameterized by using the LADM to estimate the viscosity profile, and bulk STF simulations to characterize the shape of the weight function. We also discuss a Jacobi like iterative scheme to solve for the velocity profiles, which does not require additional boundary conditions other than the slip velocity in Dirichlet form. The presented model marks a significant improvement in capturing the short wavelength hydrodynamic effects and shows better agreement with the velocity profiles obtained from NEMD simulations, in comparison to the Stokes equation.

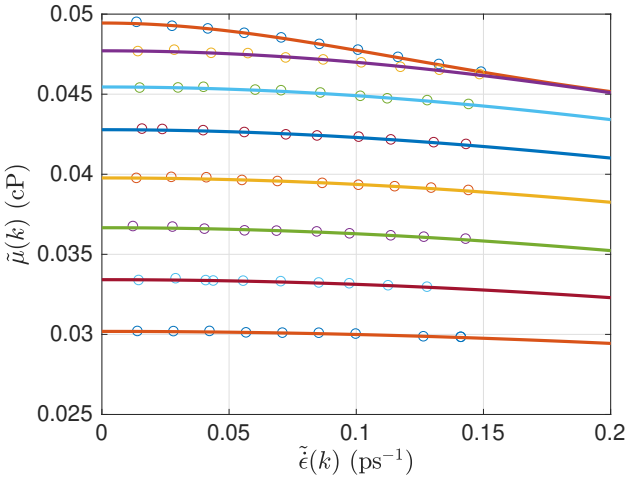

Figure 6.1: Shear rate dependence of k-space viscosity for first eight modes $n = 1$ to $n = 8$.

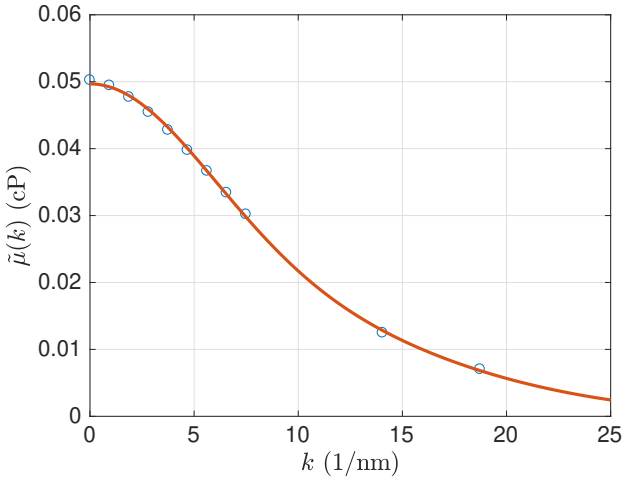

Figure 6.2: Variation of zero shear rate k-space viscosity. STF computed data is represented by blue circles, while the red line shows a Gaussian fit.

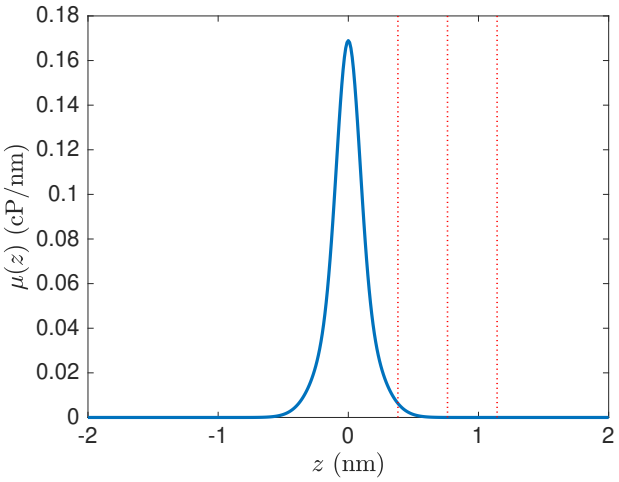

Figure 6.3: Real space viscous kernel plotted using a Gaussian function. The red vertical lines are spaced at one molecular diameter apart to interpret the support of the kernel.

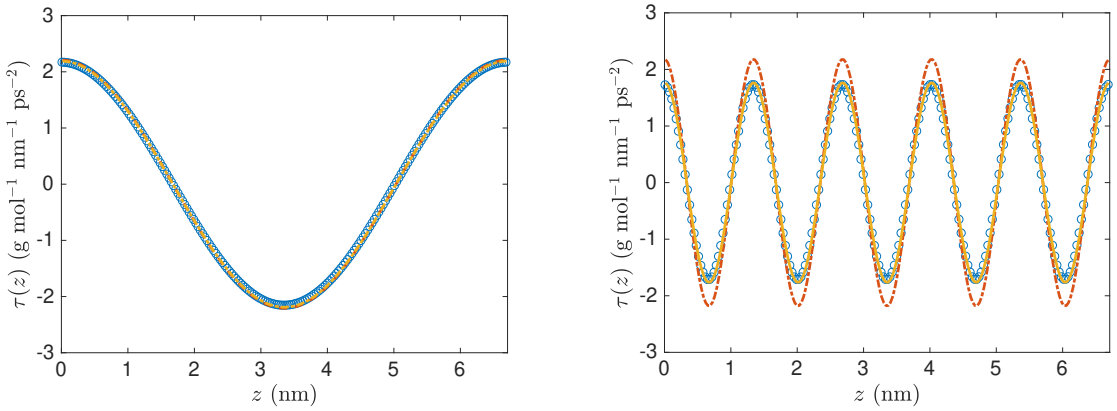

(a) $n = 1$ (b) $n = 5$

Figure 6.4: Comparison of shear stress in bulk using the local (red dashed line) and non-local (yellow solid line) model against STF-MD (blue circles) simulations for (a) fundamental mode ($n = 1$), and (b) $n = 5$.

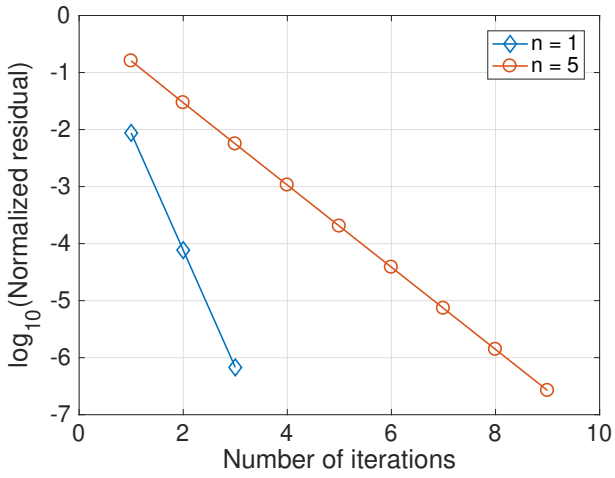

Figure 6.5: Normalized residual vs. number of iterations for the iterative method in bulk.

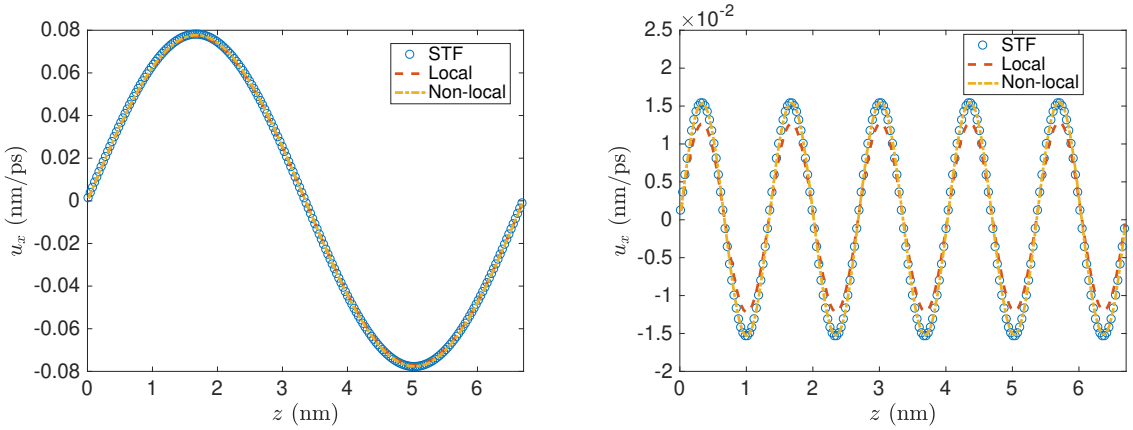

(a) $n = 1$ (b) $n = 5$

Figure 6.6: Comparison of STF velocity profile predictions in bulk WCA fluid using the local (red dashed line) and non-local (yellow solid line) model against STF-MD (blue circles) simulations for (a) fundamental mode ($n = 1$), and (b) $n = 5$.

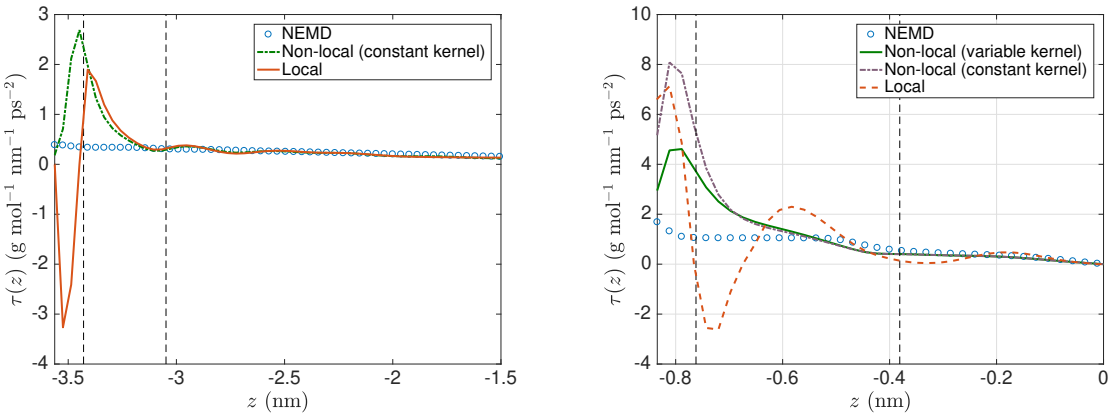

(a) $20\sigma_{\mathrm{ff}}$ (b) $20\sigma_{\mathrm{ff}}$

Figure 6.7: Comparison of confined shear stress for (a) $20\sigma_{\mathrm{ff}}$, and (b) $6\sigma_{\mathrm{ff}}$ wide slits.

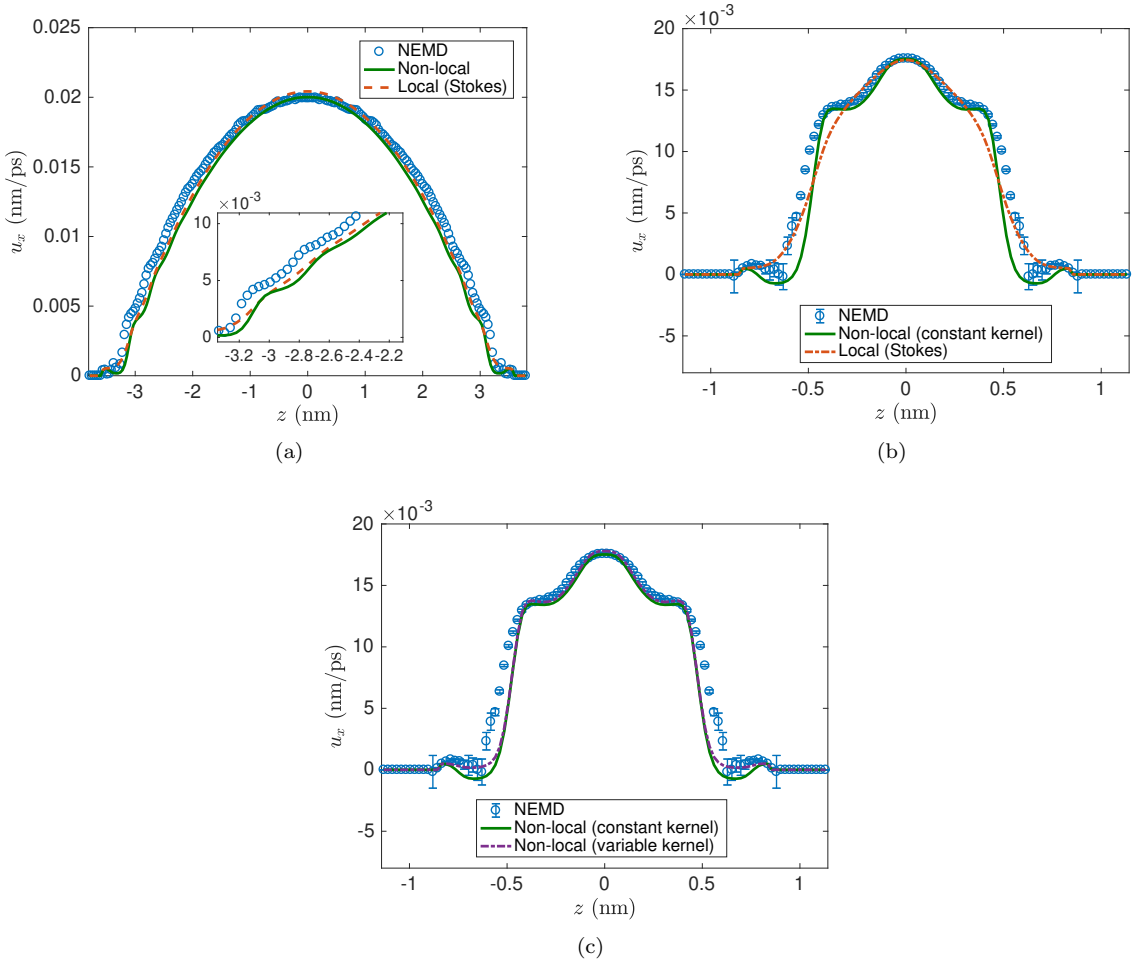

Figure 6.8: Comparison of local and non-local model predicted velocity profiles against NEMD velocity profiles for (a) $20\sigma_{\text{ff}}$, and (b) $6\sigma_{\text{ff}}$ wide slits. (c) compares the performance of constant vs. position dependent kernel for $6\sigma_{\text{ff}}$ wide slit.

Chapter 7

Conclusions

The primary conclusions of this research work are as follows

- In Chapter 2, we have developed a quasi-continuum hydrodynamic transport model for gravity driven flow in slit shaped nanopores. We have demonstrated the importance of both viscous and slip components in the velocity profile by considering three different types of systems which elucidate competition between the two phenomenon. Density profiles are used to calculate space dependent viscosity profile, using LADM method. This variation is necessary to capture the non-parabolic nature of velocity profiles as it would have been for constant density and viscosity case. A general boundary condition which takes into account the total wall-fluid interactions modeled into the static Langevin equation describing center of mass motion of fluid inside the slit is used. It is demonstrated that this boundary condition works for a spectrum of wall-fluid interaction type, and its parameters are constant for fluids confined in slit under same thermodynamic state. Furthermore, it is revealed from the velocity profiles that the slip contribution in mass flow rate increases in all cases when the confining length is decreased, which indicates that wall-fluid effects become more dominant compared to fluid-fluid effects for smaller slit sizes. Overall, the model results in good agreement with the velocity profiles obtained from NEMD simulations, and is valid for reasonable thermodynamic states that are studied in experiments for a variety of wall-surface interactions.

- In Chapter 3, we have developed a continuum based hydrodynamic transport model for gravity driven flow of water in slit shaped nanochannels. The boundary condition is formulated in the form of a slip velocity, which is dependent on the interfacial friction coefficient. The friction coefficient provides the atomistic to continuum bridge by incorporating the effect of the lattice structure and the nature of wall-fluid interactions. It is estimated using the wall-fluid force autocorrelation and force-velocity cross-correlation functions, which are computed using a GLE based dynamical framework. The correlations computed using the GLE model are in good agreement with those computed using EMD simulations of confined fluid. Furthermore, it is revealed from the velocity profiles that the slip length is invariant with

channel width under certain conditions, and therefore it can serve as the single transport parameter characterizing the surface-fluid interaction for a fixed thermodynamic state.

- In Chapter 4, we have developed a continuum based hydrodynamic transport model for isothermal, non reacting mixture transport in slit shaped nanochannels. We have focused on species transport equation instead of mixture motion as a whole. Viscous contributions are incorporated using partial viscosities, which are evaluated using vdW1 and LADM formulation. A Maxwell-Stefan type term is included to characterize the interspecies friction. The boundary conditions are provided in the form of a friction based condition that contains the species-specific interfacial friction coefficient. The friction coefficient is computed using a refined GLE based dynamical framework for mixtures. The species-specific memory function for the GLE is obtained implicitly by utilizing the corresponding MFE of the single particle VACF. The resulting correlations show good agreement with their EMD counterparts. Under application of gravity, the species velocity profiles are predicted that are in excellent agreement with NEMD velocities. The accuracy of the model remains unchanged in cases of species driven by different gravity fields. In the cases considered, the mixture was observed to behave as a pseudo fluid, that can be solved with preexisting one component transport models. Furthermore, it is also revealed from the calculations that the effective friction coefficient of the mixture varies linearly with molar composition at constant pressure and temperature, and therefore can be directly predicted from the pure component friction coefficients. The slip lengths of the species are observed to be different from each other.

- In Chapter 5, we have presented an interfacial friction based multiscale transport model for electroosmotic flow. Spatial inhomogeneity in the solvent viscosity is modeled with separate contributions due to the layering of solvent density and ion densities. Local viscosity variations include contributions from the solvent structure using LADM and ion concentration dependent excess contributions by the local application of Fuoss-Onsager theory, and Hubbard-Onsager electro-hydrodynamic equation based dielectric friction theory. Interfacial friction dependent slip velocity is used as the boundary condition. The friction parameter depends upon the time correlations, which are in turn computed using a refined GLE framework that uses the electrochemical wall-solvent force map as an input, and is observed to compare well with their EMD computed values. The segregation of flow profile into the slip and viscous contributions allows us to separately predict the phenomenon of interfacial thickening of the solvent and enhanced interfacial friction due to the coupling of LJ and electrostatic forces. It is inferred that the interfacial friction for a positively charged wall is higher as compared to the negatively charged wall of equal charge density magnitude. The proposed model shows good agreement of EOF velocity

profiles against NEMD computed ones for a variety of input parameters such as wall-type, surface charge densities and applied electric fields, including the cases of anomalous transport such as EOF reversal.

- In Chapter 6, we have presented a multiscale, non-local transport model for nanochannel flow. The non-local model postulates that the point-wise shear stress depends upon the strain-rate in its neighborhood. This dependence is characterized by a viscous kernel, which is isotropic in bulk but non-isotropic in confined systems. The non-isotropic viscous kernel can easily be parameterized by using the LADM to estimate the viscosity profile, and bulk STF simulations to characterize the shape of the weight function. We also discuss a Jacobi like iterative scheme to solve for the velocity profiles, which does not require additional boundary conditions other than the slip velocity in Dirichlet form. The presented model marks a significant improvement in capturing the short wavelength hydrodynamic effects and shows better agreement with the velocity profiles obtained from NEMD simulations, in comparison to the Stokes equation.

Appendix A: Multicomponent transport equations

Here we derive the vector form of Navier Stokes transport equations for multicomponent mixture. We would begin with control volume formulation of continuity and momentum equations and reduce them into PDE form. The interspecies friction term would account for the hydrodynamic drag experienced by a component from other species constituting the mixture.

Continuity

The control volume form of the continuity equation describing the conservation of density $m_\alpha \rho_\alpha$ for species α can be written as

$$\frac{\mathrm{d}}{\mathrm{d}t} \int\limits_{V_\alpha(t)} m_\alpha \rho_\alpha \mathrm{d}V = \int\limits_{V_\alpha(t)} m_\alpha (\Delta s_\alpha) \mathrm{d}V, \tag{1}$$

where $V_\alpha(t)$ is the control volume that is translating with the continuum velocity $\mathbf{u}_\alpha(\mathbf{r}, t)$. The right side of the above equation has m_α as the molar mass and s_α as the rate of generation (with units of $[\mathrm{L}^{-3}\mathrm{T}^{-1}]$). Since the choice of the control volume is arbitrary, the integrands must be equal. Dropping the volume integrals and expanding the total derivative into partial time and density flux, the equivalent local PDE form of the above equation is written as

$$\frac{\partial}{\partial t}(m_\alpha \rho_\alpha) + \nabla \cdot (m_\alpha \rho_\alpha \mathbf{u}_\alpha) = m_\alpha (\Delta s_\alpha). \tag{2}$$

Momentum

We apply a similar control volume based approach on momentum flux $m_\alpha \rho_\alpha \mathbf{u}_\alpha$ of species α as

$$\frac{\mathrm{d}}{\mathrm{d}t} \int\limits_{V_\alpha(t)} m_\alpha \rho_\alpha \mathbf{u}_\alpha \mathrm{d}V = \int\limits_{S_\alpha(t)} \mathbf{\Pi}_\alpha \cdot \mathbf{n} \mathrm{d}S + \int\limits_{V_\alpha(t)} m_\alpha \rho_\alpha \mathbf{f}_\alpha \mathrm{d}V + \int\limits_{V_\alpha(t)} m_\alpha (\Delta s_\alpha) \mathbf{u}_\alpha \mathrm{d}V + \int\limits_{V_\alpha(t)} \rho_\alpha \mathbf{F}_\alpha^* \mathrm{d}V, \tag{3}$$

where the stress tensor $\mathbf{\Pi}_\alpha$ contains both hydrostatic and deviatoric components, and its flux is considered moving across the surface $S_\alpha(t)$, which encloses the control volume $V_\alpha(t)$. The second term on the RHS represents the body force, while the third term is momentum change due to mass generation, which is assumed to be generated with the velocity $\mathbf{u}_\alpha$. The final term is included due to interspecies momentum transfer which is dependent on the species concentration, and the interspecies force $\mathbf{F}^*_\alpha$ consists of contributions from all of the other components and will be discussed later. Similar to the continuity equation, the present equation can be converted into the local PDE form as

$$\frac{\partial}{\partial t}(m_\alpha \rho_\alpha \mathbf{u}_\alpha) + \nabla \cdot (m_\alpha \rho_\alpha \mathbf{u}_\alpha \otimes \mathbf{u}_\alpha) = \nabla \cdot \mathbf{\Pi}_\alpha + m_\alpha \rho_\alpha \mathbf{f}_\alpha + m_\alpha (\Delta s_\alpha)\mathbf{u}_\alpha + \rho_\alpha \mathbf{F}^*_\alpha, \tag{4}$$

where we have also invoked the Gauss' divergence theorem. The symbol $\mathbf{u}_\alpha \otimes \mathbf{u}_\alpha$ denotes the outer product of velocity field and results in a tensor. Using the identity $\nabla \cdot (m_\alpha \rho_\alpha \mathbf{u}_\alpha \otimes \mathbf{u}_\alpha) = \mathbf{u}_\alpha (\nabla \cdot m_\alpha \rho_\alpha \mathbf{u}_\alpha) + m_\alpha \rho_\alpha (\mathbf{u}_\alpha \cdot \nabla \otimes \mathbf{u}_\alpha)$, and application of chain rule on the partial time derivative, we can rewrite LHS of Eq. (4) as

$$m_\alpha \rho_\alpha \frac{\partial \mathbf{u}_\alpha}{\partial t} + \underbrace{\mathbf{u}_\alpha \frac{\partial m_\alpha \rho_\alpha}{\partial t} + \mathbf{u}_\alpha (\nabla \cdot m_\alpha \rho_\alpha \mathbf{u}_\alpha)} + m_\alpha \rho_\alpha (\mathbf{u}_\alpha \cdot \nabla \mathbf{u}_\alpha), \tag{5}$$

where the term in the underbraces can be simplified to $m_\alpha (\Delta s_\alpha)\mathbf{u}_\alpha$ by using the continuity equation (Eq. (2)). Equating Eq. (5) and RHS terms from Eq. (4); and dropping the momentum term due to generation from both sides, we get

$$m_\alpha \rho_\alpha \left(\frac{\partial \mathbf{u}_\alpha}{\partial t} + \mathbf{u}_\alpha \cdot \nabla \otimes \mathbf{u}_\alpha \right) = \nabla \cdot \mathbf{\Pi}_\alpha + m_\alpha \rho_\alpha \mathbf{f}_\alpha + \rho_\alpha \mathbf{F}^*_\alpha. \tag{6}$$

This equation is the momentum equation for species α, and is very similar to the Cauchy momentum equation for pure component fluid, except for the introduction of interspecies friction force, which is absent in pure component equation. Next, we will discuss the constitutive relationship for stress and interspecies friction force.

Constitutive relationships

Stress tensor

The stress tensor for species α can be decomposed into hydrostatic partial pressure (P_α) and deviatoric ($\boldsymbol{\tau}_\alpha$) contributions

$$\mathbf{\Pi}_\alpha = -P_\alpha \mathbf{I} + \boldsymbol{\tau}_\alpha, \tag{7}$$

where $\mathbf{I}$ is the identity matrix. At this stage, we can ignore the compressibility (bulk viscosity) and invoke the stress-strain constitutive relationship

$$\boldsymbol{\tau}_\alpha = \frac{1}{2}\mu_\alpha^{\mathrm{P}}\left[\nabla \otimes \mathbf{u}_\alpha + (\nabla \otimes \mathbf{u}_\alpha)^{\mathrm{T}}\right], \tag{8}$$

where μ_α^{P} is the partial shear viscosity, and T denotes the transpose. Now the divergence term finally reduces to

$$\nabla \cdot \boldsymbol{\Pi}_\alpha = -\nabla P_\alpha + \mu_\alpha^{\mathrm{P}} \nabla^2 \mathbf{u}_\alpha, \tag{9}$$

Interspecies friction

The interspecies friction force $\mathbf{F}_\alpha^*$ consists of contributions from all other species β in the mixture, hence it can be expressed as

$$\mathbf{F}_\alpha^* = \sum_{\substack{\beta=1 \\ \beta\neq\alpha}}^{N} \rho_\beta F_{\alpha\beta}, \tag{10}$$

where the hydrodynamic drag component $F_{\alpha\beta}$ is assumed to be proportional to the relative velocity of the two species, and directed to oppose the motion of the species. Its phenomenological form can be expressed as

$$F_{\alpha\beta} = -\zeta_{\alpha\beta}(\mathbf{u}_\alpha - \mathbf{u}_\beta), \tag{11}$$

where $\zeta_{\alpha\beta}$ is the interspecies friction coefficient, and is related to the binary Maxwell-Stefan diffusivity as $\zeta_{\alpha\beta} = k_{\mathrm{B}}T/\rho_t D_{\alpha\beta}$. Here the mixture density $\rho_t = \sum_\alpha \rho_\alpha$, is the sum of all component densities. Now the total interspecies force can be written as

$$\rho_\alpha \mathbf{F}_\alpha^* = \sum_{\substack{\beta=1 \\ \beta\neq\alpha}}^{N} \frac{k_{\mathrm{B}}T\rho_\alpha\rho_\beta}{\rho_t D_{\alpha\beta}}(\mathbf{u}_\beta - \mathbf{u}_\alpha), \tag{12}$$

One-Dimensional simplification

Using results from Eq. (9) and Eq. (12) in Eq. (6), we can write the momentum equation as

$$m_\alpha\rho_\alpha\left(\frac{\partial \mathbf{u}_\alpha}{\partial t} + \mathbf{u}_\alpha \cdot \nabla \otimes \mathbf{u}_\alpha\right) = -\nabla P_\alpha + \mu_\alpha^{\mathrm{P}}\nabla^2\mathbf{u}_\alpha + m_\alpha\rho_\alpha\mathbf{f}_\alpha + \sum_{\substack{\beta=1 \\ \beta\neq\alpha}}^{N} \frac{k_{\mathrm{B}}T\rho_\alpha\rho_\beta}{\rho_t D_{\alpha\beta}}(\mathbf{u}_\beta - \mathbf{u}_\alpha). \tag{13}$$

These are N equations for velocity, and together with N continuity equations from Eq. (2), are able to fully describe the three dimensional velocity and density fields for isothermal, incompressible flow.

The following assumptions are made for 1D, gravity driven flow of a binary mixture $N = 2$,

1. No pressure gradient, $\nabla P_\alpha = 0$, and

2. No inertia term, LHS $= 0$,

Therefore the final equation can be written as

$$\frac{\mathrm{d}}{\mathrm{d}z}\left[\mu_\alpha^{\mathrm{P}}\frac{\mathrm{d}u_\alpha}{\mathrm{d}z}\right] + m_\alpha \rho_\alpha g_\alpha + \sum_{\substack{\beta=1 \\ \beta\neq\alpha}}^{2} \frac{k_{\mathrm{B}} T \rho_\alpha \rho_\beta}{\rho_t D_{\alpha\beta}} \left(u_\beta - u_\alpha\right) = 0, \tag{14}$$

References

[1] E. Akhmatskaya, B. D. Todd, P. J. Daivis, D. J. Evans, K. E. Gubbins, and L. A. Pozhar. A study of viscosity inhomogeneity in porous media. *J. Chem. Phys.*, 106(11):4684–4695, 1997.

[2] A. V. Anil Kumar and Suresh K. Bhatia. Mechanisms influencing levitation and the scaling laws in nanopores: oscillator model theory. *J. Phys. Chem. B*, 110(7):3109–3113, 2006. PMID: 16494316.

[3] C. A. J. Appelo. Specific conductance – how to calculate the specific conductance with PHREEQC. Technical report, 2010. Report.

[4] Gaurav Arya, Hsueh-Chia Chang, and Edward J. Maginn. Knudsen diffusivity of a hard sphere in a rough slit pore. *Phys. Rev. Lett.*, 91:026102, 2003.

[5] Gaurav Arya, Hsueh-Chia Chang, and Edward J. Maginn. Mol. simul.s of knudsen wall-slip: Effect of wall morphology. *Mol. Simul.*, 29(10-11):697–709, 2003.

[6] W. T. Ashurst and W. G. Hoover. Dense-fluid shear viscosity via nonequilibrium molecular dynamics. *Phys. Rev. A*, 11:658–678, 1975.

[7] S. Balasubramanian, Christopher J. Mundy, and Michael L. Klein. Shear viscosity of polar fluids: Molecular dynamics calculations of water. *The Journal of Chemical Physics*, 105(24):11190–11195, 1996.

[8] A. Barati Farimani, N. R. Aluru, and Emad Tajkhorshid. Thermodynamic insight into spontaneous hydration and rapid water permeation in aquaporins. *Applied Physics Letters*, 105(8):–, 2014.

[9] Jean-Louis Barrat and Lydéric Bocquet. Influence of wetting properties on hydrodynamic boundary conditions at a fluid/solid interface. *Farad. Discuss.*, 112:119–127, 1999.

[10] H. J. C. Berendsen, J. R. Grigera, and T. P. Straatsma. The missing term in effective pair potentials. *J. Phys. Chem.*, 91(24):6269–6271, 1987.

[11] B. J. Berne and G. D. Harp. *On the Calculation of Time Correlation Functions*, pages 63–227. John Wiley & Sons, Inc., 2007.

[12] B. J. Berne and G. D. Harp. *On the Calculation of Time Correlation Functions*, pages 102–106, 217–222. John Wiley & Sons, Inc., 2007.

[13] Ravi Bhadauria and N R Aluru. A quasi-continuum hydrodynamic model for slit shaped nanochannel flow. *The Journal of Chemical Physics*, 139(7):074109, 2013.

[14] Ravi Bhadauria and N. R. Aluru. A multiscale transport model for Lennard-Jones binary mixtures based on interfacial friction. *J. Chem. Phys.*, 145(7):074115, 2016.

[15] Ravi Bhadauria and N R Aluru. Multiscale modeling of electroosmotic flow: Effects of discrete ion, enhanced viscosity, and surface friction. *J. Chem. Phys.*, 146(18):184106, 2017.

[16] Ravi Bhadauria and N. R. Aluru. A multiscale transport model for non-classical nanochannel electroosmosis. *J. Chem. Phys.*, 147(21):214105, 2017.

[17] Ravi Bhadauria, Tarun Sanghi, and N. R. Aluru. Interfacial friction based quasi-continuum hydrodynamical model for nanofluidic transport of water. *The Journal of Chemical Physics*, 143(17):174702, 2015.

[18] S. K. Bhatia and D. Nicholson. Anomalous transport in molecularly confined spaces. *J. Chem. Phys.*, 127(12):124701, 2007.

[19] Suresh Bhatia and David Nicholson. Modeling Mixture Transport at the Nanoscale: Departure from Existing Paradigms. *Physical Review Letters*, 100(23):11–14, 2008.

[20] Suresh K. Bhatia, Mauricio Rincon Bonilla, and David Nicholson. Molecular transport in nanopores: a theoretical perspective. *Phys. Chem. Chem. Phys.*, 13:15350–15383, 2011.

[21] Suresh K. Bhatia, Haibin Chen, and David S. Sholl. Comparisons of diffusive and viscous contributions to transport coefficients of light gases in single-walled carbon nanotubes. *Mol. Simul.*, 31(9):643–649, 2005.

[22] Suresh K. Bhatia, Owen Jepps, and David Nicholson. Tractable molecular theory of transport of lennard-jones fluids in nanopores. *J. Chem. Phys.*, 120(9):4472–4485, 2004.

[23] Suresh K. Bhatia and David Nicholson. Transport of simple fluids in nanopores: Theory and simulation. *AIChE J.*, 52(1):29–38, 2006.

[24] Suresh K. Bhatia and David Nicholson. Friction based modeling of multicomponent transport at the nanoscale. *The Journal of Chemical Physics*, 129(16):164709, 2008.

[25] Suresh K. Bhatia and David Nicholson. Friction between solids and adsorbed fluids is spatially distributed at the nanoscale. *Langmuir*, 29(47):14519–14526, 2013.

[26] R. B. Bird, W. E. Stewart, and E. N. Lightfoot. *Transport Phenomena*, page 27. John Wiley & Sons, Inc., 2 edition, 2002.

[27] I. Bitsanis, J. J. Magda, M. Tirrell, and H. T. Davis. Molecular dynamics of flow in micropores. *The Journal of Chemical Physics*, 87(3):1733–1750, 1987.

[28] I. Bitsanis, T. K. Vanderlick, M. Tirrell, and H. T. Davis. A tractable molecular theory of flow in strongly inhomogeneous fluids. *The Journal of Chemical Physics*, 89(5):3152–3162, 1988.

[29] Felipe J. Blas and Ichiro Fujihara. Excess properties of Lennard-Jones binary mixtures from computer simulation and theory. *Molecular Physics*, 100(17):2823–2838, 2002.

[30] Lydéric Bocquet and Jean-Louis Barrat. Hydrodynamic boundary conditions, correlation functions, and kubo relations for confined fluids. *Phys. Rev. E*, 49:3079–3092, 1994.

[31] Lydéric Bocquet and Jean-Louis Barrat. Flow boundary conditions from nano- to micro-scales. *Soft Matter*, 3:685–693, 2007.

[32] Douwe Jan Bonthuis, Stephan Gekle, and Roland R. Netz. Dielectric profile of interfacial water and its effect on double-layer capacitance. *Phys. Rev. Lett.*, 107:166102, Oct 2011.

[33] Jean Pierre Boon and Sidney Yip. *Molecular hydrodynamics*. McGraw-Hill New York ; London, 1980.

[34] Barry R. Breslau and Irving Franklin Miller. On the viscosity of concentrated aqueous electrolyte solution. *The Journal of Physical Chemistry*, 74(5):1056–1061, 1970.

[35] Cullen R Buie, Jonathan D Posner, Tibor Fabian, Suk-Won Cha, Daejoong Kim, Fritz B Prinz, John K Eaton, and Juan G Santiago. Water management in proton exchange membrane fuel cells using integrated electroosmotic pumping. *J. Power Sources*, 161(1):191–202, 2006.

[36] Peter J Cadusch, B D Todd, Junfang Zhang, and Peter J Daivis. A non-local hydrodynamic model for the shear viscosity of confined fluids: analysis of a homogeneous kernel. *Journal of Physics A: Mathematical and Theoretical*, 41(3):035501, 2008.

[37] Bing-Yang Cao, Jun Sun, Min Chen, and Zeng-Yuan Guo. Molecular momentum transport at fluid-solid interfaces in mems/nems: A review. *International Journal of Molecular Sciences*, 10(11):4638–4706, 2009.

[38] Amalendu Chandra and Biman Bagchi. Ionic contribution to the viscosity of dilute electrolyte solutions: Towards a microscopic theory. *J. Chem. Phys.*, 113(8):3226–3232, 2000.

[39] Sydney Chapman and T. G. Cowling. *The mathematical theory of non-uniform gases; an account of the kinetic theory of viscosity, thermal conduction, and diffusion in gases*. Cambridge [Eng.] University Press, 1939.

[40] Marco Antonio Chávez-Rojo and Magdaleno Medina-Noyola. Self-consistent generalized Langevin equation for colloidal mixtures. *Phys. Rev. E*, 72:031107, 2005.

[41] Ting Horng Chung, Mohammad Ajlan, Lloyd L. Lee, and Kenneth E. Starling. Generalized multiparameter correlation for nonpolar and polar fluid transport properties. *Ind. Eng. Chem. Res.*, 27(4):671–679, 1988.

[42] Benjamin A. Dalton, Kirill S. Glavatskiy, Peter J. Daivis, and B. D. Todd. Nonlocal response functions for predicting shear flow of strongly inhomogeneous fluids. ii. sinusoidally driven shear and multisinusoidal inhomogeneity. *Phys. Rev. E*, 92:012108, Jul 2015.

[43] Sanjit K. Das, Mukul M. Sharma, and Robert S. Schechter. Solvation force in confined molecular fluids using molecular dynamics simulation. *J. Phys. Chem.*, 100(17):7122–7129, 1996.

[44] H. Ted Davis. *Statistical Mechanics of Phases, Interfaces and Thin Films*. Wiley, 1996.

[45] J. E. Desnoyers and G. Perron. The viscosity of aqueous solutions of alkali and tetraalkylammonium halides at 25 c. *Journal of Solution Chemistry*, 1(3):199–212, Sep 1972.

[46] Denis J. Evans. Computer simulation of burnett hydrodynamics. *Molecular Physics*, 47(5):1165–1170, 1982.

[47] Denis J. Evans and Gary Morriss. *Statistical Mechanics of Nonequilibrium Liquids*. Cambridge University Press, 2 edition, 2008.

[48] H. Falkenhagen. *Phys. Z.*, 32:745, 1931.

[49] George S. Fanourgakis, J. S. Medina, and R. Prosmiti. Determining the bulk viscosity of rigid water models. *The Journal of Physical Chemistry A*, 116(10):2564–2570, 2012.

[50] Daniel G. Friend and James C. Rainwater. Transport properties of a moderately dense gas. *Chem. Phys. Lett.*, 107(6):590 – 594, 1984.

[51] Guillaume Galliéro, Christian Boned, and Antoine Baylaucq. Molecular dynamics study of the Lennard-Jones fluid viscosity: Application to real fluids. *Industrial and Engineering Chemistry Research*, 44:6963–6972, 2005.

[52] Xuechao Gao, Joo C. Diniz da Costa, and Suresh K. Bhatia. Adsorption and transport of gases in a supported microporous silica membrane. *Journal of Membrane Science*, 460(0):46 – 61, 2014.

[53] Kirill S. Glavatskiy, Benjamin A. Dalton, Peter J. Daivis, and B. D. Todd. Nonlocal response functions for predicting shear flow of strongly inhomogeneous fluids. i. sinusoidally driven shear and sinusoidally driven inhomogeneity. *Phys. Rev. E*, 91:062132, Jun 2015.

[54] E. Gongadze, U. van Rienen, V. Kralj-Iglič, and A. Iglič. Spatial variation of permittivity of an electrolyte solution in contact with a charged metal surface: a mini review. *Comput Methods Biomech Biomed Engin*, 16(5):463–480, May 2013.

[55] Ekaterina Gongadze, Aljaž Velikonja, Šarka Perutkova, Peter Kramar, Alenka Maček-Lebar, Veronika Kralj-Iglič, and Aleš Iglič. Ions and water molecules in an electrolyte solution in contact with charged and dipolar surfaces. *Electrochimica Acta*, 126:42–60, 2014.

[56] M.C Gordillo and J Marti. Hydrogen bond structure of liquid water confined in nanotubes. *Chemical Physics Letters*, 329(5?6):341 – 345, 2000.

[57] Eveline M. Gosling, I.R. McDonald, and K. Singer. On the calculation by molecular dynamics of the shear viscosity of a simple fluid. *Molecular Physics*, 26(6):1475–1484, 1973.

[58] H. Grabert. *Projection Operator Techniques in Nonequilibrium Statistical Mechanics*. Springer, Berlin, 1982.

[59] Robert D. Groot and Patrick B. Warren. Dissipative particle dynamics: Bridging the gap between atomistic and mesoscopic simulation. *The Journal of Chemical Physics*, 107(11):4423–4435, 1997.

[60] Zhaoli Guo, T. S. Zhao, Chao Xu, and Young Shi. Simulation of fluid flows in the nanometer: kinetic approach and molecular dynamic simulation. *Int. J. Comput. Fluid D.*, 20(6):361–367, 2006.

[61] Nicolas G. Hadjiconstantinou and Anthony T. Patera. Heterogeneous atomistic-continuum representations for dense fluid systems. *International Journal of Modern Physics C*, 08(04):967–976, 1997.

[62] J. Hansen and I. R. McDonald. *Theory of Simple Liquids*. Elsevier, 2006.

[63] J. S. Hansen, Peter J. Daivis, Karl P. Travis, and B. D. Todd. Parameterization of the nonlocal viscosity kernel for an atomic fluid. *Phys. Rev. E*, 76:041121, Oct 2007.

[64] J. S. Hansen, B. D. Todd, and Peter J. Daivis. Prediction of fluid velocity slip at solid surfaces. *Phys. Rev. E*, 84:016313, 2011.

[65] Remco Hartkamp, Bertrand Siboulet, Jean-François Dufrêche, and Benoit Coasne. Ion-specific adsorption and electroosmosis in charged amorphous porous silica. *Physical Chemistry Chemical Physics*, 17(38):24683–24695, 2015.

[66] Eugene Helfand. Transport coefficients from dissipation in a canonical ensemble. *Phys. Rev.*, 119:1–9, Jul 1960.

[67] D. M. Heyes. Molecular dynamics simulations of liquid binary mixtures: Partial properties of mixing and transport coefficients. *The Journal of Chemical Physics*, 96(3):2217–2227, 1992.

[68] Hai Hoang and Guillaume Galliero. Shear viscosity of inhomogeneous fluids. *J. Chem. Phys.*, 136(12):124902, 2012.

[69] Jason K. Holt, Hyung Gyu Park, Yinmin Wang, Michael Stadermann, Alexander B. Artyukhin, Costas P. Grigoropoulos, Aleksandr Noy, and Olgica Bakajin. Fast mass transport through sub-2-nanometer carbon nanotubes. *Science*, 312(5776):1034–1037, 2006.

[70] P. J. Hoogerbrugge and J. M. V. A. Koelman. Simulating microscopic hydrodynamic phenomena with dissipative particle dynamics. *EPL (Europhysics Letters)*, 19(3):155, 1992.

[71] Kai Huang and Izabela Szlufarska. Green-kubo relation for friction at liquid-solid interfaces. *Phys. Rev. E*, 89:032119, 2014.

[72] G Hummer, JC Rasaiah, and JP Noworyta. Water conduction through the hydrophobic channel of a carbon nanotube. *Nature*, 414(6860):188–190, NOV 8 2001.

[73] K. Ibuki, T.-A. Hoshina, and M. Ueno. Reliability and Limitations of Dielectric Continuum Model for Ionic Mobility in Subcritical Liquid Methanol and Water. In J. Kawamura, S. Yoshikado, T. Sakuma, Y. Michihiro, M. Aniya, and Y. Ito, editors, *Superionic Conductor Physics*, pages 35–40, January 2007.

[74] K Ibuki and M Nakahara. Effect of dielectric friction on the viscosity b coefficient for electrolyte in methanol–water mixture. *J. Chem. Phys.*, 86(10):5734–5738, 1987.

[75] G. Ihm, Yuhua Song, and E. A. Mason. A new strong principle of corresponding states for nonpolar fluids. *J. Chem. Phys.*, 94(5):3839–3848, 1991.

[76] Owen G. Jepps, Suresh K. Bhatia, and Debra J. Searles. Wall mediated transport in confined spaces: Exact theory for low density. *Phys. Rev. Lett.*, 91:126102, 2003.

[77] Owen G. Jepps, Suresh K. Bhatia, and Debra J. Searles. Modeling molecular transport in slit pores. *J. Chem. Phys.*, 120(11):5396–5406, 2004.

[78] Laurent Joly, Christophe Ybert, Emmanuel Trizac, and Lydric Bocquet. Liquid friction on charged surfaces: From hydrodynamic slippage to electrokinetics. *J. Chem. Phys.*, 125(20):204716, 2006.

[79] Sony Joseph and N. R. Aluru. Pumping of confined water in carbon nanotubes by rotation-translation coupling. *Phys. Rev. Lett.*, 101:064502, Aug 2008.

[80] Sony Joseph and N. R. Aluru. Why are carbon nanotubes fast transporters of water? *Nano Letters*, 8(2):452–458, 2008.

[81] Amrit Kalra, Shekhar Garde, and Gerhard Hummer. Osmotic water transport through carbon nanotube membranes. *Proceedings of the National Academy of Sciences*, 100(18):10175–10180, 2003.

[82] Sridhar Kumar Kannam, B. D. Todd, J. S. Hansen, and Peter J. Daivis. How fast does water flow in carbon nanotubes? *The Journal of Chemical Physics*, 138(9):–, 2013.

[83] Rohit Karnik, Rong Fan, Min Yue, Deyu Li, Peidong Yang, and Arun Majumdar. Electrostatic control of ions and molecules in nanofluidic transistors. *Nano letters*, 5(5):943–948, 2005.

[84] P. J. A. M Kerkhof and M. A. M. Geboers. Analysis and extension of the theory of multicomponent fluid diffusion. *Chemical Engineering Science*, 60(12):3129–3167, 2005.

[85] P. J. A. M. Kerkhof, M. A. M. Geboers, and Krzysztof J. Ptasinski. On the isothermal binary mass transport in a single pore. *Chemical Engineering Journal*, 83:107–121, 2001.

[86] Piet J. A. M. Kerkhof and Marcel A. M. Geboers. Toward a unified theory of isotropic molecular transport phenomena. *AIChE Journal*, 51(1):79–121, 2005.

[87] S. Koneshan and Jayendran C. Rasaiah. Computer simulation studies of aqueous sodium chloride solutions at 298 k and 683 k. *J. Chem. Phys.*, 113(18), 2000.

[88] Evangelos M. Kotsalis. *Multiscale modeling and simulation of fullerenes in liquids*. PhD thesis, ETH Zürich, 2008.

[89] R. Kubo. The fluctuation-dissipation theorem. *Rep. Prog. Phys.*, 29(1):255–284, 1966.

[90] Sridhar Kumar Kannam, B. D. Todd, J. S. Hansen, and Peter J. Daivis. Slip length of water on graphene: Limitations of non-equilibrium molecular dynamics simulations. *The Journal of Chemical Physics*, 136(2):–, 2012.

[91] Song Hi Lee and Jayendran C. Rasaiah. Molecular dynamics simulation of ion mobility. 2. alkali metal and halide ions using the spc/e model for water at 25 c. *The Journal of Physical Chemistry*, 100(4):1420–1425, 1996.

[92] J Lyklema and J.Th.G Overbeek. On the interpretation of electrokinetic potentials. *Journal of Colloid Science*, 16(5):501 – 512, 1961.

[93] Abdelhamid Maali, Touria Cohen-Bouhacina, and Hamid Kellay. Measurement of the slip length of water flow on graphite surface. *Applied Physics Letters*, 92(5):–, 2008.

[94] M Majumder, N Chopra, R Andrews, and BJ Hinds. Nanoscale hydrodynamics: Enhanced flow in carbon nanotubes (vol 438, pg 44, 2005). *Nature*, 438(7070):930, DEC 15 2005.

[95] Gerald S Manning. The interaction between a charged wall and its counterions: A condensation theory. *J. Phys. Chem. B*, 114(16):5435–5440, 2010.

[96] G. A. Mansoori, N. F. Carnahan, K. E. Starling, and T. W. Leland. Equilibrium thermodynamic properties of the mixture of hard spheres. *The Journal of Chemical Physics*, 54(4):1523–1525, 1971.

[97] A. Martini, A. Roxin, R. Q. Snurr, Q. Wang, and S. Lichter. Molecular mechanisms of liquid slip. *J. Fluid Mech.*, 600:257–269, 2008.

[98] S. Y. Mashayak and N. R. Aluru. Coarse-grained potential model for structural prediction of confined water. *J. Chem. Theory Comput.*, 8(5):1828–1840, 2012.

[99] S. Y. Mashayak and N. R. Aluru. Coarse-grained potential model for structural prediction of confined water. *J. Chem. Theory Comput.*, 8(5):1828–1840, 2012.

[100] S. Y. Mashayak and N. R. Aluru. Thermodynamic state-dependent structure-based coarse-graining of confined water. *The Journal of Chemical Physics*, 137(21):214707, 2012.

[101] S Y Mashayak, M H Motevaselian, and N R Aluru. An EQT-cDFT approach to determine thermodynamic properties of confined fluids. *The Journal of Chemical Physics*, 142(24):244116, 2015.

[102] SY Mashayak and N. R. Aluru. Langevin-poisson-eqt: A dipolar solvent based quasi-continuum approach for electric double layers. *The Journal of Chemical Physics*, 146(4):044108, 2017.

[103] Nargess Mehdipour and Hossein Eslami. Calculation of transport properties of simple dense fluids. *Int. J. Therm. Sci.*, 41(10):949 – 954, 2002.

[104] Karsten Meier, Arno Laesecke, and Stephan Kabelac. Transport coefficients of the lennard-jones model fluid. i. viscosity. *The Journal of Chemical Physics.*, 121(8):3671–3687, 2004.

[105] Hazime Mori. Transport, collective motion, and brownian motion. *Prog. Theor. Phys.*, 33(3):423–455, 1965.

[106] M H Motevaselian, S Y Mashayak, and N R Aluru. An EQT-based cDFT approach for a confined Lennard-Jones fluid mixture. *The Journal of Chemical Physics*, 143(12):124106, 2015.

[107] CLMH Navier. Mémoire sur les lois du mouvement des fluides. *Mémoires de lAcadémie Royale des Sciences de lInstitut de France*, 6:389–440, 1823.

[108] Chiara Neto, Drew R Evans, Elmar Bonaccurso, Hans-Jrgen Butt, and Vincent S J Craig. Boundary slip in newtonian liquids: a review of experimental studies. *Reports on Progress in Physics*, 68(12):2859, 2005.

[109] Anoosheh Niavarani and Nikolai V. Priezjev. Modeling the combined effect of surface roughness and shear rate on slip flow of simple fluids. *Phys. Rev. E*, 81:011606, 2010.

[110] Shuichi Nosé. A unified formulation of the constant temperature molecular dynamics methods. *J. Chem. Phys.*, 81(1):511–519, 1984.

[111] Sergei Yu. Noskov, Wonpil Im, and Benot Roux. Ion permeation through the α-hemolysin channel: Theoretical studies based on brownian dynamics and poisson-nernst-plank electrodiffusion theory. *Biophysical Journal*, 87(4):2299 – 2309, 2004.

[112] Sean T. O'Connell and Peter A. Thompson. Molecular dynamics–continuum hybrid computations: A tool for studying complex fluid flows. *Phys. Rev. E*, 52:R5792–R5795, Dec 1995.

[113] Lars Onsager. Reciprocal relations in irreversible processes. i. *Phys. Rev.*, 37:405–426, Feb 1931.

[114] Lars Onsager. Reciprocal relations in irreversible processes. ii. *Phys. Rev.*, 38:2265–2279, Dec 1931.

[115] Lars Onsager and R. M. Fuoss. Irreversible processes in electrolytes. diffusion, conductance and viscous flow in arbitrary mixtures of strong electrolytes. *The Journal of Physical Chemistry*, 36(11):2689–2778, 1931.

[116] Gustavo A. Orozco, Othonas A. Moultos, Hao Jiang, Ioannis G. Economou, and Athanassios Z. Panagiotopoulos. Molecular simulation of thermodynamic and transport properties for the h2o+nacl system. *J. Chem. Phys.*, 141(23):234507, 2014.

[117] Mohammad Mehdi Papari. Transport properties of carbon dioxide from an isotropic and effective pair potential energy. *Chemical Physics*, 288(2–3):249 – 259, 2003.

[118] Hyung Gyu Park and Yousung Jung. Carbon nanofluidics of rapid water transport for energy applications. *Chem. Soc. Rev.*, 43:565–576, 2014.

[119] M. Parrinello and A. Rahman. Polymorphic transitions in single crystals: A new molecular dynamics method. *Journal of Applied Physics*, 52(12):7182, 1981.

[120] Rupali S. Patil, Vasim R. Shaikh, Pankaj D. Patil, Amulrao U. Borse, and Kesharsingh J. Patil. The viscosity b and d coefficient (jonesdole equation) studies in aqueous solutions of alkyltrimethylammonium bromides at 298.15k. *Journal of Molecular Liquids*, 200:416 – 424, 2014.

[121] Janka Petravic and Peter Harrowell. On the equilibrium calculation of the friction coefficient for liquid slip against a wall. *J. Chem. Phys.*, 127(17):174706, 2007.

[122] Eric R. Pinnick, Shyamsunder Erramilli, and Feng Wang. Computational investigation of lipid hydration water of l 1-palmitoyl-2-oleoyl-sn-glycero-3-phosphocholine at three hydration levels. *Molecular Physics*, 108(15):2027–2036, 2010.

[123] Steve Plimpton. Fast parallel algorithms for short-range molecular dynamics. *J. Comput. Phys.*, 117:1–19, 1995.

[124] JG Powles. Dielectric relaxation and the internal field. *The Journal of Chemical Physics*, 21(4):633–637, 1953.

[125] Liudmila A. Pozhar. Structure and dynamics of nanofluids: Theory and simulations to calculate viscosity. *Phys. Rev. E*, 61:1432–1446, Feb 2000.

[126] Liudmila A. Pozhar and Keith E. Gubbins. Dense inhomogeneous fluids: Functional perturbation theory, the generalized langevin equation, and kinetic theory. *J. Chem. Phys.*, 94(2):1367–1384, 1991.

[127] Liudmila A. Pozhar and Keith E. Gubbins. Transport theory of dense, strongly inhomogeneous fluids. *J. Chem. Phys.*, 99(11):8970–8996, 1993.

[128] M Předota, AV Bandura, PT Cummings, JD Kubicki, DJ Wesolowski, AA Chialvo, and ML Machesky. Electric double layer at the rutile (110) surface. 1. structure of surfaces and interfacial water from molecular dynamics by use of ab initio potentials. *J. Phys. Chem. B*, 108(32):12049–12060, 2004.

[129] M Předota, Peter T Cummings, and David J Wesolowski. Electric double layer at the rutile (110) surface. 3. inhomogeneous viscosity and diffusivity measurement by computer simulations. *J. Phys. Chem. C*, 111(7):3071–3079, 2007.

[130] Nikolai V. Priezjev. Rate-dependent slip boundary conditions for simple fluids. *Phys. Rev. E*, 75:051605, 2007.

[131] Nikolai V. Priezjev and Sandra M. Troian. Influence of periodic wall roughness on the slip behaviour at liquid/solid interfaces: molecular-scale simulations versus continuum predictions. *J. Fluid Mech.*, 554:25–46, 2006.

[132] R. Qiao and N. R. Aluru. Ion concentrations and velocity profiles in nanochannel electroosmotic flows. *J. Chem. Phys.*, 118(10):4692–4701, 2003.

[133] R. Qiao and N. R. Aluru. Charge inversion and flow reversal in a nanochannel electro-osmotic flow. *Phys. Rev. Lett.*, 92:198301, May 2004.

[134] R Qiao and N. R. Aluru. Atomistic simulation of kcl transport in charged silicon nanochannels: interfacial effects. *Colloids Surf., A*, 267(1):103–109, 2005.

[135] R Qiao and N. R. Aluru. Surface-charge-induced asymmetric electrokinetic transport in confined silicon nanochannels. *Appl. Phys. Lett.*, 86(14):143105, 2005.

[136] B. Quentrec. Dependance de la viscosit'e en fonction du taux de cisaillement dans un fluide de lennard-jones. *Molecular Physics*, 46(4):707–714, 1982.

[137] A. V. Raghunathan, J. H. Park, and N. R. Aluru. Interatomic potential-based semiclassical theory for lennard-jones fluids. *The Journal of Chemical Physics*, 127(17):174701, 2007.

[138] A. Rahman. Correlations in the motion of atoms in liquid argon. *Phys. Rev.*, 136:A405–A411, Oct 1964.

[139] Rodrigo A. Reis, Ronaldo Nobrega, José V. Oliveira, and Frederico W. Tavares. Self- and mutual diffusion coefficient equation for pure fluids, liquid mixtures and polymeric solutions. *Chemical Engineering Science*, 60(16):4581–4592, 2005.

[140] Eli Ruckenstein and Hongqin Liu. Self-diffusion in gases and liquids. *Industrial & engineering chemistry research*, 36(9):3927–3936, 1997.

[141] T. Sanghi and N. R. Aluru. A transferable coarse-grained potential to study the structure of confined, supercritical lennard-jones fluids. *The Journal of Chemical Physics*, 132(4):044703, 2010.

[142] T. Sanghi and N. R. Aluru. Coarse-grained potential models for structural prediction of carbon dioxide (co2]) in confined environments. *The Journal of Chemical Physics*, 136(2):024102, 2012.

[143] T. Sanghi and N. R. Aluru. A combined quasi-continuum/langevin equation approach to study the self-diffusion dynamics of confined fluids. *The Journal of Chemical Physics*, 138(12):–, 2013.

[144] T. Sanghi and N. R. Aluru. Thermal noise in confined fluids. *The Journal of Chemical Physics*, 141(17):174707, 2014.

[145] Tarun Sanghi, Ravi Bhadauria, and N. R. Aluru. Memory effects in nanoparticle dynamics and transport. *J. Chem. Phys.*, 145(13):134108, 2016.

[146] Mark S. P. Sansom and Philip C. Biggin. Biophysics: Water at the nanoscale. *Nature*, 414:156–159, 2001.

[147] Richard B. M. Schasfoort, Stefan Schlautmann, Jan Hendrikse, and Albert van den Berg. Field-effect flow control for microfabricated fluidic networks. *Science*, 286(5441):942–945, 1999.

[148] Mark A. Shannon, Paul W. Bohn, Menachem Elimelech, John G. Georgiadis, Benito J. Marinas, and Anne M. Mayes. Science and technology for water purification in the coming decades. *Nature*, 452(7185):301–310, 2008.

[149] David E. Smith and Liem X. Dang. Computer simulations of nacl association in polarizable water. *J. Chem. Phys.*, 100(5):3757, 1994.

[150] Ian K. Snook and William van Megen. Calculation of solvation forces between solid particles immersed in a simple liquid. *J. Chem. Soc., Farad. Trans. 2*, 77:181–190, 1981.

[151] V. P. Sokhan, D. Nicholson, and N. Quirke. Fluid flow in nanopores: An examination of hydrodynamic boundary conditions. *J. Chem. Phys.*, 115(8):3878–3887, 2001.

[152] V. P. Sokhan, D. Nicholson, and N. Quirke. Transport properties of nitrogen in single walled carbon nanotubes. *J. Chem. Phys.*, 120(8):3855–3863, 2004.

[153] V. P. Sokhan and N. Quirke. Interfacial friction and collective diffusion in nanopores. *Mol. Simul.*, 30(4):217–224, 2004.

[154] Vlad P. Sokhan and Nicholas Quirke. Slip coefficient in nanoscale pore flow. *Phys. Rev. E*, 78:015301, 2008.

[155] Vladimir P. Sokhan, David Nicholson, and Nicholas Quirke. Fluid flow in nanopores: Accurate boundary conditions for carbon nanotubes. *J. Chem. Phys.*, 117(18):8531–8539, 2002.

[156] William A. Steele. The physical interaction of gases with crystalline solids: Iġas-solid energies and properties of isolated adsorbed atoms. *Surface Science*, 36(1):317–352, 1973.

[157] M. E. Suk, A. V. Raghunathan, and N. R. Aluru. Fast reverse osmosis using boron nitride and carbon nanotubes. *Appl. Phys. Lett.*, 92(13):133120, 2008.

[158] Myung E. Suk and N. R. Aluru. Water transport through ultrathin graphene. *J. Phys. Chem. Lett.*, 1(10):1590–1594, 2010.

[159] Emad Tajkhorshid, Peter Nollert, Morten O. Jensen, Larry J. W. Miercke, Joseph O'Connell, Robert M. Stroud, and Klaus Schulten. Control of the selectivity of the aquaporin water channel family by global orientational tuning. *Science*, 296(5567):525–530, 2002.

[160] John A. Thomas and Alan J. H. McGaughey. Reassessing fast water transport through carbon nanotubes. *Nano Letters*, 8(9):2788–2793, 2008.

[161] Peter A. Thompson and Sandra M. Troian. A general boundary condition for liquid flow at solid surfaces. *Nature*, 389:360–362, 1997.

[162] B. D. Todd and J. S. Hansen. Nonlocal viscous transport and the effect on fluid stress. *Phys. Rev. E*, 78:051202, 2008.

[163] B. D. Todd, J. S. Hansen, and Peter J. Daivis. Nonlocal shear stress for homogeneous fluids. *Phys. Rev. Lett.*, 100:195901, May 2008.

[164] Karl P. Travis and Keith E. Gubbins. Poiseuille flow of lennard-jones fluids in narrow slit pores. *J. Chem. Phys.*, 112(4):1984–1994, 2000.

[165] Karl P. Travis, Debra J. Searles, and Denis J. Evans. On the wavevector dependent shear viscosity of a simple fluid. *Molecular Physics*, 97(3):415–422, 1999.

[166] Karl P. Travis, B. D. Todd, and Denis J. Evans. Departure from navier-stokes hydrodynamics in confined liquids. *Phys. Rev. E*, 55:4288–4295, Apr 1997.

[167] T. K. Vanderlick, L. E. Scriven, and H. T. Davis. Molecular theories of confined fluids. *The Journal of Chemical Physics*, 90(4):2422–2436, 1989.

[168] Feng-Chao Wang and Ya-Pu Zhao. Slip boundary conditions based on molecular kinetic theory: The critical shear stress and the energy dissipation at the liquid-solid interface. *Soft Matter*, 7:–, 2011.

[169] C. R. Wilke. A Viscosity Equation for Gas Mixtures. *The Journal of Chemical Physics*, 18(4):517, 1950.

[170] Leslie V. Woodcock. Equation of state for the viscosity of lennard-jones fluids. *AIChE J.*, 52(2):438–446, 2006.

[171] Margaret Robson Wright. *An Introduction to Aqueous Electrolyte Solutions*, pages 245, 380. John Wiley & Sons, Inc., 2007.

[172] Peng Wu and Rui Qiao. Physical origins of apparently enhanced viscosity of interfacial fluids in electrokinetic transport. *Phys. Fluids*, 23(7):072005, 2011.

[173] Yanbin Wu and N. R. Aluru. Graphitic carbon–water nonbonded interaction parameters. *The Journal of Physical Chemistry B*, 117(29):8802–8813, 2013.

[174] Xin Yong and Lucy Zhang. Slip in nanoscale shear flow: mechanisms of interfacial friction. *Microfluid. Nanofluid.*, 14(1-2):299–308, 2012.

[175] Hiroaki Yoshida, Hideyuki Mizuno, Tomoyuki Kinjo, Hitoshi Washizu, and Jean-Louis Barrat. Generic transport coefficients of a confined electrolyte solution. *Phys. Rev. E*, 90:052113, Nov 2014.

[176] Hiroaki Yoshida, Hideyuki Mizuno, Tomoyuki Kinjo, Hitoshi Washizu, and Jean-Louis Barrat. Molecular dynamics simulation of electrokinetic flow of an aqueous electrolyte solution in nanochannels. *J. Chem. Phys.*, 140(21):214701, 2014.

[177] Junfang Zhang, B. D. Todd, and Karl P. Travis. Viscosity of confined inhomogeneous nonequilibrium fluids. *The Journal of Chemical Physics*, 121(21):10778–10786, 2004.

[178] Yingxi Zhu and Steve Granick. Rate-dependent slip of newtonian liquid at smooth surfaces. *Phys. Rev. Lett.*, 87:096105, Aug 2001.

[179] Yingxi Zhu and Steve Granick. Limits of the hydrodynamic no-slip boundary condition. *Phys. Rev. Lett.*, 88:106102, 2002.

[180] R. Zwanzig. *Nonequilibrium Statistical Mechanics*. Oxford University Press, 2001.